KU LEUVEN

FACULTEIT WETENSCHAPPEN

Modeling and Simulation of Two-Step Resonance Ionization Processes using CW and Pulsed Lasers

Ruben DE GROOTE

Promotor: Prof. Dr. G. Neyens
KULeuven

Co-promotor: Dr. K.T. Flanagan
University of Manchester

Proefschrift ingediend tot het
behalen van de graad van
Master of Science in de Fysica

Academiejaar 2012-2013

ABSTRACT

This thesis derives and discusses equations that describe the evolution of atomic systems subjected to two monochromatic and coherent radiation fields and treats both continuous and temporally pulsed irradiation. This theoretical description is developed mainly to understand the influence of the photon field intensities on experimental ionization spectra. The primary application of this theoretical framework is on methods that rely on resonant laser excitation and non-resonant laser ionization to extract information on the hyperfine structure of atomic systems.

In particular, qualitative and quantitative discussions on the laser-related changes in hyperfine splitting extracted from ionization spectra are presented. Also, a method for increasing the resolution of resonance ionization techniques (potentially up until the natural linewidth of the electronic transitions) is discussed and theoretically justified. Both topics are illustrated with experimental data.

SAMENVATTING

Deze thesis bevat afleidingen voor vergelijkingen die de evolutie van atomaire systemen beschrijven onder invloed van twe coherente, monochromatische stralingsvelden. Deze velden kunnen zowel continu als gepulsd in de tijd zijn. De hoofdreden voor de ontwikkeling van dit theoretisch kader is om de invloed van de intensiteit van deze stralingsvelden op experimentele ionizatiespectra na te gaan. Het toepassingsgebied van dit werk situeert zich dan ook binnen methodes die gebruik maken van resonante laser-excitatie en niet-resonante laserionizatie om de hyperfijnstructuur van atomaire systemen te karakterizeren.

Een eerste luik van de thesis presenteert zowel kwantitatief als kwalitatief onderzoek rond laser-gerelateerde veranderingen in experimenteel geëxtraheerde hyperfijn parameters. Verder wordt ook een methode besproken die de resolutie van resonantie laser ionizatietechnieken zou kunnen verbeteren (potentieel tot en met de natuurlijke lijnbreedte van de electronische transities). Beide onderwerpen worden geïllustreerd met experimentele data.

VULGARISERENDE SAMENVATTING

Een belangrijke observatie in de kernfysica is dat er kernen zijn met een bepaalde configuratie van protonen en neutronen die ervoor zorgen dat ze opmerkelijke eigenschappen hebben. Deze kernen worden met de naam ‘magische kernen’ aangeduid en vormen de hoeksteen van ons theoretisch begrip van de kernfysica. Een belangrijke open vraag binnen het hedendaagse onderzoek is in hoeverre onze kennis over de gemakkelijk bestudeerbare magische kernen mag veralgemeend worden naar meer exotische kernen. Dergelijke exotische kernen zijn vaak heel kortlevend en moeilijk te produceren, wat het onderzoek natuurlijk moeilijker maakt.

Recent werd er in CERN een nieuw experiment ontwikkeld om eigenschappen van die exotische kernen te bestuderen. Dit experiment berust op het gebruik van lasers om de fijnere details van de kernstructuur te ontrafelen. Om dat op een nauwkeurige en precieze manier te doen moet natuurlijk volledig in kaart gebracht worden hoe die lasers precies inwerken op de atomen. Het is op dit moment dat deze thesis op de voorgrond komt. Vertrekkende van de basiswetten van de kwantummechanica gaat deze thesis dieper in op de laser-atoom interacties met als duidelijk doel de toepassing in de nucleaire spectroscopie.

Essentieel bevat deze thesis twee resultaten. Een eerste is dat de interacties van de lasers en atomen ervoor kunnen zorgen dat de parameters die uit een experiment worden gedestilleerd kunnen afwijken van hun eigenlijke, echte waarde. Enige voorzichtigheid is dus geboden bij het kiezen van de experimentele condities. Een tweede resultaat bestaat uit een beschrijving en een theoretische onderbouwing van een nieuwe methode waarmee zowel de precisie als de nauwkeurigheid van de experimentele techniek in principe significant verbeterd zou kunnen worden. Beide resultaten werden experimenteel gestaafd.

"To achieve great things, two things are needed: a plan and not quite enough time." — Leonard Bernstein

ACKNOWLEDGMENTS

Er zijn waarschijnlijk veel thesisschrijvende studenten die de uitspraak op de vorige bladzijde al zelf ondervonden hebben. Het ontbreekt vaak niet aan plannen of ambities; zo goed als altijd aan tijd om die te verwezenlijken. Een van de laatste stappen in een goed stappenplan is, zo wil de traditie, het schrijven van een dankwoord.

Geheel volgens de traditie begint zo'n dankwoord met het vermelden van de begeleiders en de promotoren die bovengenaamde wilde plannen in goede banen leiden (al dan niet door ze ietwat minder wild te maken). Professor Gerda Neyens is dan ook de eerste naam die ik hier wil vermelden. Bedankt om me de vrijheid te geven zelf mijn weg uit te stippelen en zelf richting te geven aan een open onderzoeksopdracht. Of die vrijheid en de daarbijhorende chronische tijdsnood daadwerkelijk tot *great things* heeft geleid laat ik aan de lezer over. . .

If anyone is ever in need of some ambitious ideas, they should go to Kieran. Thank you for pointing out the interesting questions, for the patience required to listen to my incoherent answers (no pun intended) and for investing so much time in the experiments presented in this thesis. I should of course also thank Ronald and Mark for freeing up their busy schedules; it would've proven difficult to do resonance ionization spectroscopy without the expertise to take care of the 'resonance' part.

Stijn en Ivan, bedankt om het betere deel van een zomer in CERN aangenamer te maken en natuurlijk ook voor de prima sfeer in ons kantoor. Hanne en Marieke, sta me toe me te excuseren voor de ongetwijfeld behoorlijk verminderde concentratie en jullie te bedanken voor de fijne samenwerking doorheen het voorbije jaar.

Aan iedereen van tweede master fysica: bedankt voor de voorbije vijf jaar; voor de vele leerrijke gesprekken en vooral voor de uiterst aangename 'extracurriculaire activiteiten'.

Mama, papa, zonder jullie was ik natuurlijk al helemaal niet aan het begin van deze thesis geraakt. Bedankt. Zoals jullie ook wel weten omvatten bovengenoemde extracurriculaire activiteiten enkel scrabbleavonden met een fruitsapje naar keuze. Echt.

Ruben

CONTENTS

LIST OF FIGURES

LIST OF TABLES

FOREWORD

This thesis grew out of a need to understand the finer details of resonance ionization spectroscopy (RIS). This technique has already been used in various nuclear physics applications [1], and a new Collinear Resonance Ionization Spectroscopy (CRIS) beam line has recently been constructed at ISOLDE, CERN, to apply it to nuclear physics cases. CRIS uses a collinear geometry: the laser beams and the atomic or ionic beam travel along the same straight line. Schematically, a first laser beam is tuned so that the energy of one photon matches the energy difference between two electronic states in the atom of interest. This first laser step is followed by a second one, with photons of sufficient energy to non-resonantly ionize only the electrons that were excited by the first laser. Then, the atomic beam is separated from its ionized component, and these ions are detected.

This approach has two distinct advantages over fluorescence detection methods: ions can be detected much more efficiently than photons and they can be separated from the non-ionized background, leading to background-free detection. There are downsides however. For example, there is an issue related to the phenomenon of power broadening (a notion that will be developed more rigorously later in this thesis): the higher the laser power density, the broader the line shapes will be. This is undesirable since it means that the energy resolution of the experiment goes down as it tries to be more efficient. Additionally CRIS uses more than one laser step with a non-resonant ionization step that requires a high-power laser. A crucial question is therefore what minimal resolution could be attained using CRIS. The answer on this question then determines the physics cases within reach of the technique.

Note that the previous paragraph made two statements but did not provide an explanation as to why they are true:

1. The more powerful the laser, the broader the line shape.
2. The second laser step further broadens the line shape.

Both of these statements have to be made more precise and quantified. Doing this will require a more sophisticated language: a mathematical model that describes resonant laser ionization physics. The next chapters are devoted to the development of such a model. This model not only describes power broadening of line shapes, it also predicts some systematic effects that have to be understood to perform high-resolution CRIS experiments.

Since this thesis is mainly theoretical in nature, such a high-resolution CRIS experiment will be abstracted. An atom, nucleus and electrons, is represented by a collection of atomic quantum states. The two lasers are described by electromagnetic fields (be it in quantized form or just as classical fields). A CRIS experiment is then simulated by applying two electromagnetic fields to these discrete states and by then solving the equations of motion. The first laser field is responsible for the energy-sensitivity of CRIS; it scans the energies of the electronic state. The second laser provides a probe of the first laser and the impact it has on the system.

Having two photon fields that can interact with the discrete states and the continuum can bring unexpected physics to light; resonance positions can change and the resonance shapes can be asymmetrized. These effects, while always interesting from a theoretical point of view, could be a hindrance for an experimentalist. The aim of this thesis is therefore to investigate these effects, and to determine whether or not they are detrimental to the extraction of nuclear observables. If they are, the next question is then if they can be avoided or, if this is not the case, understood well enough to allow for accurate corrections during data analysis. This is a research topic that has already attracted some interest in the Leuven nuclear moments group[2].

If pulsed lasers are used, using a probe field also brings along an additional degree of freedom: it allows the experimentalist to choose when to probe, in contrast with fluorescence detection which is spontaneous decay process. This thesis will also attempt to study this degree of freedom.

It is worthwhile to briefly go over the structure of this document. First, a model for resonant ionization physics will be developed. Before discussing any of the applications, the link between the physics of the electronic states and the nucleus will be explained (summarizing the theory of hyperfine interactions). This chapter will allow the formulation of some well-defined test cases that will be studied to better understand two distinct topics: power broadening and systematic energy shifts due to coherent effects. Since the CRIS experiment uses pulsed lasers, the comments made in the previous paragraph will play a decisive role here.

Part I

THEORETICAL FOUNDATIONS

1

HYPERFINE INTERACTIONS

The study of exotic nuclei (nuclei with a proton-to neutron ratio that is significantly different from the ratio in stable isotopes) has proven to be an ideal testing ground for nuclear structure theory, and continuously provides input for new theoretical models [3]. Understanding the exact nature of the proton-neutron interaction relies crucially on the measurement of nuclear moments, mainly the magnetic dipole moment and the electric quadrupole moment. The magnetic dipole moment is sensitive to the single particle orbit occupied by the unpaired nucleon in odd-odd or odd-even nuclei, while the electrical quadrupole moment provides key information on collective effects and deformation of nuclei. One of the ways these moments can be experimentally measured is by studying the hyperfine interaction between the nucleus and the electrons that orbit it. The Collinear Resonance Ionization Spectroscopy (CRIS) technique probes these hyperfine energy levels. The goal of CRIS is to enable the study of exotic nuclei in cases where the production is too low for other methods [4, 5]. This chapter will briefly revise the basics of hyperfine interaction and its application for nuclear structure research.

1.1 THE HYPERFINE INTERACTION

The hyperfine interaction is a result of the interaction of the nuclear multipole moments with the charge and current distributions of the electrons that orbit the nucleus [6]. This interaction modifies the Hamiltonian of the nucleus-electron system and therefore leads to a small shift in the energies and lifting of the degeneracies of the electronic states. The size and sign of this shift depends not only on these multipole moments but also on the total angular momentum of the states, which causes them to lift the degeneracy of the energy levels in a 'Coloumb atom'. The magnitude of the shift is also determined by the size of the multipole moments of the nucleus. This means that information on the nuclear properties can be extracted from the energy splitting of the hyperfine-split states.

The total angular momentum of a state in the nucleus-electron system is determined by the total electronic spin $\hat{J}$ and the total nuclear spin $\hat{I}$. In free atoms, these two spins couple together and result in a total angular momentum $\hat{F}$. Each relative orientation of the angular momenta $\hat{J}$ and $\hat{I}$ results in a different value of the norm F of $\hat{F}$; its value is therefore restricted to $F \in \{|I-J|, |I-J+1|, \dots, I+J-1, I+J\}$. In absence of interactions other than the simple Coulomb interaction, all of these F-states are degenerate, but the addition of the hyperfine interaction can completely lift this degeneracy.

The higher the order of the multipole moment, the smaller the effect of the interaction on the energy levels will be. The dominant contribution to the total hyperfine splitting is therefore due to the interaction of the electrons with the magnetic dipole and the electric quadrupole moment of the nucleus. The nuclear magnetic moment $\hat{\mu}$ can be related to its spin through a dimensionless g-factor and and the nuclear magneton $\mu_N = \frac{e}{2m_p}$:

$$\hat{\mu} = g\mu_N \hat{I}. \tag{1}$$

The quadrupole moment $\hat{Q}$ for a system of charges q_i (e.g. protons) can be defined as

$$\hat{Q} = \sqrt{\frac{16\pi}{5}} \sum_i q_i \hat{r}_i^2 Y_2^0(\theta_i, \phi_i), \tag{2}$$

where Y_2 is the spherical harmonic function of order two. The hyperfine Hamiltonian of the system due to the nuclear magnetic dipole and electric quadrupole moment interacting with the magnetic field and electric field gradient induced by the electron cloud is given by

$$\hat{H}_{dip} + \hat{H}_{quad} = -\hat{\mu} \cdot \hat{B} - \frac{1}{6}\hat{Q} \cdot \nabla E. \tag{3}$$

The corresponding energy shift can be expressed as function of the angular momenta in the system, the experimental nuclear moments, μ and Q_s, and the hyperfine parameters A (related to the dipole interaction) and B (linked to the quadrupole interaction). These A and B parameters are defined as follows:

$$A = \frac{\mu B(0)}{IJ} \qquad B = eQ_s \frac{\partial^2 V}{\partial z^2}. \tag{4}$$

$B(0)$ is the magnetic field in the center of the nucleus induced by the electrons and V is the electric potential at the center of the nucleus created by the electrons. Note how these quantities contain both nuclear information and electronic information.

The shifts in energy due to Hamiltonian (3) is then given by

$$E_{dip}(F) + E_{quad}(F) = -\frac{A}{2}C + B\frac{3C(C+1) - 4I(I+1)J(J+1)}{8I(2I-1)J(2J-1)}, \tag{5}$$

where $C = [F(F+1) - I(I+1) - J(J+1)]$. Interesting for nuclear physics is the fact that the size of the splittings governed by (5) gives information on nuclear properties that are very relevant for studying nuclear structure. How these energy splittings can be experimentally determined will be illustrated by explaining the idea behind the CRIS technique.

1.2 COLLINEAR RESONANCE IONIZATION SPECTROSCOPY

If the energy of laser photons exactly matches the energy separation of electronic states, the laser photons can excite electrons to a higher atomic state. Of course, angular momentum selection rules also need to be satisfied. For example, consider the level scheme shown in figure 1. There are three possible transitions here, and if the wavelength of the photons is tuned correctly, these photons will induce excitations and de-excitations among the relevant atomic states. One way of probing whether or not the laser is indeed tuned to resonance is by measuring the fluorescence photons. This is the cornerstone of collinear (fluorescence) laser spectroscopy. The technique takes advantage of the reduction in the longitudinal velocity spread of an accelerated ion beam [7]. The laser beam is overlapped with the atomic or ionic beam. A typical spectrum is shown in figure 1 along with the corresponding level scheme.

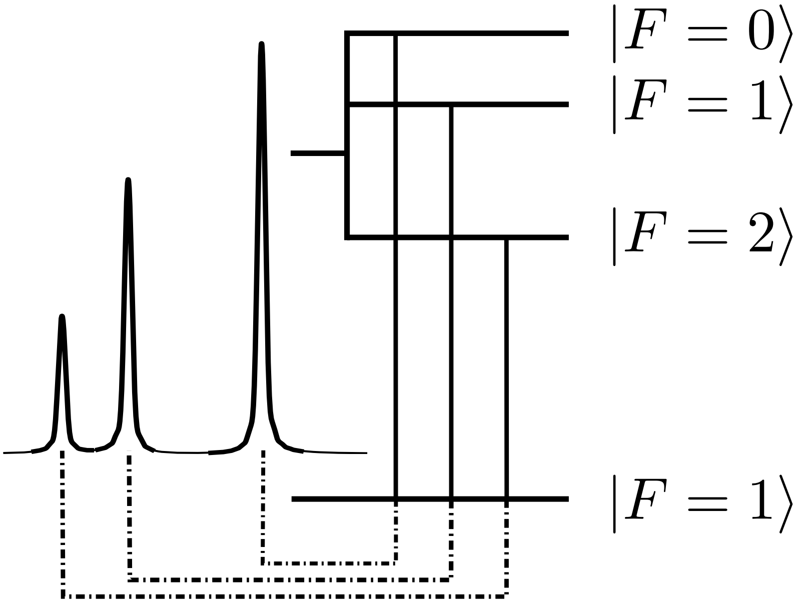

Figure 1: An example of an electronic level scheme. The states are labelled by their total angular momentum F. On the left is a typical spectrum taken by a collinear laser spectroscopy experiment.

Another way of probing the population of the excited state is to avoid letting the electron decay back to the ground state. Instead the atom is stripped of this excited electron, for example by interactions with a second laser that take the electron's energy above the ionization potential, a process which can be resonant or non-resonant. Ionization spectroscopy experiments then use some form of ion detection to determine the hyperfine structure, by recording the number of ions as function of the wavelength of the first resonant laser step. Ion detection has three advantages over photon detection:

1. Ion detectors typically have a 100% quantum efficiency, as opposed to up to 20% for photon detectors.
2. Ion detection can be performed with a 100% solid angle coverage; ions can be guided towards the detector with electromagnetic fields. Solid angles for photon detection are typically only of the order of 10% or less.
3. There is no background (e.h related to scattered light scattering of the laser beam itself). IF the resonant excitation process happens in an ultra-high vacuum environment, only resonantly excited ions are produced which can be deflected from any non-ionized background beam.

CRIS uses a second laser step to ionize excited atoms. The additional laser step can lead to higher-order couplings that can distort the experimental resonance shapes. Additionaly, the lineshapes can be broadened or shifted. The first effect results in reduced resolution and the second effect leads to a shift of the probed hyperfine levels, leading to an incorrect determination of the hyperfine parameters A and B if the lines are fitted with simple Voigt profiles. Therefore a systematic error associated with the extracted nuclear observables can occur. Understanding these effects is therefore crucial for the high-resolution operation of CRIS. This thesis aims to begin this investigation by developing a theoretical model that can take the higher order correlations into account.

2

ATOM-PHOTON INTERACTIONS: THE TWO-LEVEL ATOM

This chapter is devoted to understanding how electronic states interact with monochromatic coherent light sources, with in particular lasers in mind. The coherence properties of such sources imply that rate equations that are typically used for interactions of bound states with incoherent photons do not fully consider the physics problem. Adding coherence to the equations of motion requires using the time-dependent Schrödinger equation. This chapter will discuss solutions of this time-dependent Schrödinger equation. Rather than treating atoms and photons independently, an approach based on dressed states [8] will be used. The concept of dressed states will be introduced in this chapter.

Electrons populating excited states can decay back to a lower-lying state. This spontaneous decay mechanism will not be taken into account in this thesis. This automatically means that there is a class of effects that the model will not be able to predict which could nevertheless be of significance. Adding spontaneous decay to the model could be done in future work.

Once the interactions of bound states and laser photons are understood, the interactions that couple a bound state to a continuum will be characterized. The coupling of a bound states to the infinitely large collection of continuum states will be reduced to an effective interaction of the discrete states [11].

This thesis restricts itself to the simple scenario of two-step ionization: first a resonant excitation step, followed by a non-resonant ionization step induced by a second laser. The initial focus will be on the workhorse of atomic physics: the two-level atom. In chapter 3, the theory developed in this chapter will be expanded to larger systems.

Ideal conditions will be assumed initially. For example, the emitted wavelength spectrum of the first excitation laser is assumed to be a delta-distribution, there are no fluctuations in laser power, etc. In chapter 4, these unrealistic assumptions will be relaxed, which will result in a more realistic description of a CRIS experiment allowing for quantitative simulations and examples.

2.1 RESONANT EXCITATION: THE JAYNES-CUMMINGS MODEL

The model for resonant ionization developed in this section is called the Jaynes-Cummings model [12, 13]. Note that from now on, natural units ($\hbar = c = 1$) are used.

Consider a quantized atom consisting of two levels, labeled $|0\rangle$ and $|1\rangle$, and a photon field given by

$$\hat{\mathbf{E}} = \mathbf{e} \left(\frac{\omega_a}{\varepsilon_0 V} \right)^{\frac{1}{2}} \left(\hat{a} + \hat{a}^\dagger \right) \sin\left(kz\right), \tag{6}$$

where ω_a is the energy of the photons, ε_0 is the vacuum permittivity and V is the quantization volume. The operators $\hat{a}$ and $\hat{a}^\dagger$ are the photon annihilation and creation operators and k is the photon wave number. Throughout this derivation, boldface is used for vectors and hats for operators.

The evolution of the photons and electrons can be described by solving Schrödingers equation for a suitable Hamiltonian. The Hamiltonian describing a free atom immersed in a laser field can be expressed in terms of the fermionic and photonic creation and annihilation operators. Atomic systems where the electrons can occupy states $|0\rangle$ or $|1\rangle$ are of particular interest, requiring a pair of creation and annihiliation operators $\hat{c}_i^\dagger$ and $\hat{c}_i$ for both states. The photons should be described by coherent states with a Poissonian population distribution around the mean number of photons n. Since n is typically very large for lasers, these coherent photon states can be approximated by a number state $|n\rangle$, with corresponding annihilation (creation) operator $\hat{a}^{(\dagger)}$. If the energy of the two states are denoted with ω_i and the energy of a laser photon with ω_a, the free atom and laser Hamiltonians are then given by:

$$\hat{H}_{\text{atom}} = \omega_0 \hat{c}_0^\dagger \hat{c}_0 + \omega_1 \hat{c}_1^\dagger \hat{c}_1 \tag{7}$$

$$\hat{H}_{\text{photon}} = n\omega_a \hat{a}^\dagger \hat{a}. \tag{8}$$

The interaction Hamiltonian is given by the product of field (6) and the dipole moment of the atomic electron ($\mathbf{d} = -e\mathbf{r}$):

$$\begin{aligned} \hat{H}_{\text{int}} &= -\hat{\mathbf{d}} \cdot \hat{\mathbf{E}} \\ &= -\left(\hat{\mathbf{d}} \cdot \mathbf{e}\right) \left(\frac{\omega_a}{\varepsilon_0 V} \right)^{\frac{1}{2}} \left(\hat{a} + \hat{a}^\dagger \right) \sin\left(kz\right), \\ &= -\hat{d} \left(\frac{\omega_a}{\varepsilon_0 V} \right)^{\frac{1}{2}} \left(\hat{a} + \hat{a}^\dagger \right) \sin\left(kz\right), \end{aligned} \tag{9}$$

where the definiation $\hat{d} = \hat{\mathbf{d}} \cdot \mathbf{e}$ was made. Define also

$$\hat{g} = \hat{d} \left(\frac{\omega_a}{\varepsilon_0 V} \right)^{\frac{1}{2}} \sin\left(kz\right). \tag{10}$$

The interaction Hamiltonian can then be written as

$$\hat{H}_{\mathrm{int}} = -\,\hat{g}\left(\hat{a} + \hat{a}^{\dagger}\right) \tag{11}$$

It will prove convenient to express the total Hamiltonian $\hat{H}_{\mathrm{atom}} + \hat{H}_{\mathrm{photon}} + \hat{H}_{\mathrm{int}}$ in matrix form with respect to the two-state basis $\{|0,n\rangle, |1,n-1\rangle\}$. These two bare states are respectively the combination of the electronic ground state with n laser photons and the excited state with $n-1$ laser photons and their energy is quasi-degenerate when $\omega_a = \omega_1 - \omega_0$. The choice of these two states are the most pertinent for expressing excitations from $|0\rangle$ to $|1\rangle$ or de-excitations from $|1\rangle$ to $|0\rangle$ accompanied by absorption or emission of one of the photons. Note that, because of parity conservation,

$$\langle 0|\,\hat{d}\,|0\rangle = 0 = \langle 1|\,\hat{d}\,|1\rangle\,. \tag{12}$$

Hence, the photon field only couples one state with the other one, but not with itself. By definition of the operators $\hat{a}$ and $\hat{a}^{\dagger}$ it follows that

$$\begin{aligned}
&\langle 0,n|\,\hat{H}_{\mathrm{int}}\,|1,n-1\rangle \\
&= \langle 0|\,\hat{g}\,|1\rangle\,\langle n|\left(\hat{a} + \hat{a}^{\dagger}\right)|n-1\rangle \\
&= \sqrt{n}\,\langle 0|\,\hat{g}\,|1\rangle\,, \\
&:= g
\end{aligned} \tag{13}$$

where g is the strength of the laser-induced interactions. For a system with nuclear spin I and electronic spins J_0 and J_1, g^2 is given by [2]

$$\begin{aligned}
g^2 = &\frac{\pi e^2}{m\varepsilon_0}\frac{\mathcal{P}_1}{\omega_1 - \omega_0} f(J_0, J_1)(2J_0+1)(2F_0+1)(2F_1+1) \\
&\times \begin{pmatrix} F_1 & 1 & F_0 \\ -m_{F_1} & 0 & m_{F_0} \end{pmatrix}^2 \begin{Bmatrix} J_1 & F_1 & I \\ F_0 & J_0 & 1 \end{Bmatrix}^2,
\end{aligned} \tag{14}$$

where the $\sqrt{n}$ has been absorbed into the power density of the laser $\mathcal{P}_1$ since this is the experimentally accessible quantity. The objects on the second line of (14) are Wigner 3J and 6J symbols [14]. In equation (14) f is the oscillator strength, which is a dimensionless cross section that expresses the strength of the transition. It can be related to the Einstein coefficients and the absorption cross section [15]. The value of f depends on the transition and the atom. Values of f are tabulated, see e.g. [16] for the alkali atoms. The Hamiltonian $\hat{H}_{\mathrm{int}}$ can now be written in the basis $\{|0,n\rangle, |1,n-1\rangle\}$ as

$$H^{I} = \begin{pmatrix} 0 & g \\ g^{*} & 0 \end{pmatrix}. \tag{15}$$

By virtue of (15), the diagonal elements of the total Hamiltonian $\hat{H} = \hat{H}_{\text{atom}} + \hat{H}_{\text{photon}} + \hat{H}_{\text{int}}$ are just the matrix elements of $\hat{H}_{\text{atom}} + \hat{H}_{\text{photon}}$. For example,

$$\begin{aligned} &\langle 0, n| \hat{H}_{\text{atom}} + \hat{H}_{\text{photon}} |0, n\rangle \\ &= \langle 0| \hat{H}_{\text{atom}} |0\rangle + \langle n| \hat{H}_{\text{photon}} |n\rangle \\ &= \omega_0 + n\omega_a \end{aligned}$$

The total Hamiltonian $\hat{H}$ can then be written in the following matrix form:

$$\begin{aligned} H =& H_{\text{atom}} + H_{\text{photon}} + H^I \\ =& \begin{pmatrix} \omega_0 + n\omega_a & g \\ g^* & \omega_1 + (n-1)\omega_a \end{pmatrix}. \end{aligned} \tag{16}$$

Since the terms $n\omega_a$ only add a phase term, they can be removed without changing the dynamics. This results in the following Hamiltonian:

$$H = \begin{pmatrix} \omega_0 & g \\ g^* & \omega_1 - \omega_a \end{pmatrix}. \tag{17}$$

The coupling g can in principle depend on time, for example when the lasers are pulsed instead of continuous wave (cw). Note that $g(t)$ contains two essential bits of information:

1. The value of $g(t)$ depends on the laser power.
2. The value of $g(t)$ reflects the angular momentum selection rules. If they are not met, $g(t)$ will be zero. These selection rules are present in expression (14) through the Wigner symbols.

2.1.1 *Analytical Solution for the Two-Level Atom*

It is convenient to introduce the atom-laser detuning Δ_{01}:

$$\Delta_{01} = \omega_1 - \omega_0 - \omega_a. \tag{18}$$

This quantity expresses how much the laser frequency ω_a is detuned from the frequency difference $\omega_1 - \omega_0$ of the atomic transition. The resonance condition is therefore $\Delta_{01} = 0$. When the laser field is very weak ($g \approx 0$) the two states $\{|0, n\rangle, |1, n-1\rangle\}$ are approximately the eigenstates of the Hamiltonian. These states are called the bare states. When the laser is tuned to the resonance frequency, i.e. $\Delta_{01} = 0$, the two bare states are degenerate since the energy of the photon compensates the electronic energy difference. Due to the presence of the non-diagonal terms in (17), the laser atom interaction, these two bare states are no longer good eigenstates of the Hamiltonian and their degeneracy will be lifted. The true eigenstates of the system are called the dressed states. Finding these dressed states is most conveniently done by introducing a mixing angle θ:

$$\theta(t) = \frac{1}{2}\arctan\frac{2g(t)}{\Delta_{01}}. \tag{19}$$

The two eigenstates of (17) can then be defined as rotations of the bare states

$$|-,n\rangle = \cos\theta(t)\,|0,n\rangle - \sin\theta(t)\,|1,n-1\rangle\,, \tag{20}$$

$$|+,n\rangle = \sin\theta(t)\,|0,n\rangle + \cos\theta(t)\,|1,n-1\rangle\,, \tag{21}$$

which can be written as

$$\begin{pmatrix} |-,n\rangle \\ |+,n\rangle \end{pmatrix} = R(\theta)\begin{pmatrix} |0,n\rangle \\ |1,n-1\rangle \end{pmatrix} \tag{22}$$

with R defined as

$$R(\theta) = \begin{pmatrix} \cos\theta & -\sin\theta \\ \sin\theta & \cos\theta \end{pmatrix}. \tag{23}$$

The states (20) and (21) are the dressed states. They are sometimes also referred to as the **adiabatic states**, an name that will be explained in chapter 6. The associated eigenvalues for a detuning Δ_{01} are

$$\begin{aligned} \lambda_{\pm} &= \frac{1}{2}\left(\Delta_{01} \pm \sqrt{4g^2(t) + \Delta_{01}^2}\right) \\ &= \frac{1}{2}\Delta_{01} \pm \frac{1}{2}\Omega, \end{aligned} \tag{24}$$

where Ω is the Rabi flopping frequency:

$$\Omega = \lambda_{-} - \lambda_{+} = \sqrt{4g^2(t) + \Delta_{01}^2}. \tag{25}$$

On resonance, $\lambda_{\pm} = \pm\frac{1}{2}\sqrt{4g^2(t)} = \pm g(t)$: the two states $|-,n\rangle$ and $|+,n\rangle$ are separated by an energy $2g(t)$.

Figure 2 shows an energy diagram of a few bare (left) and dressed states (right). There are infinitely many steps to this energy ladder, since there is a doublet of dressed states for each value of n. The energy difference between the two adiabatic basis states also depends on the laser frequency. This is shown graphically in figure 3, which depicts the eigenvalues of one of the pairs in figure 2 as function of the detuning. The repelling of the energies is a sign that the two states are now coupled (mixed). It is precisely this mixing that is responsible for population transfer from the ground state to the excited state. If two eigenvalue curves cross rather than repelling, i.e. if the degeneracy of the

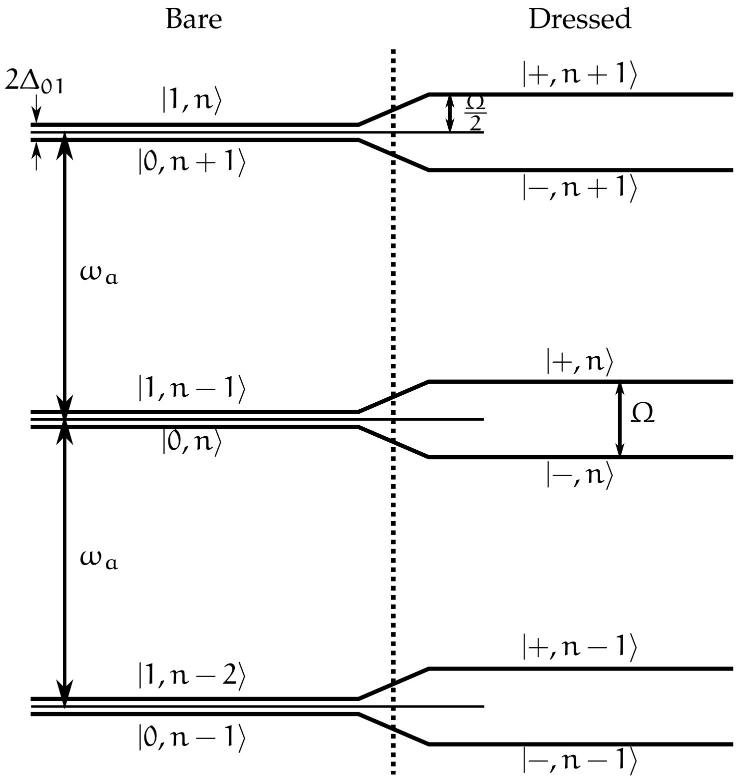

Figure 2: On the left: three pairs of bare states, each pair with one photon more than the previous. The lasers are tuned to a detuning Δ_{01}. On the right, the interaction is switched on. The approximate degeneracy is lifted by an energy splitting Ω. In principle, the energy ladder extends infinitely far up, and down until the states dressed with zero photons are reached.

dressed states is not lifted by the laser field, they do not exchange population; no electrons get excited from the electronic ground state to the electronic excited state.

The populations of an initially undressed atom (so: an atom that has not yet seen any radiation fields) when it enters a radiation field can now be calculated. The initial state of the system is $|0,n\rangle$. The effects on the population dynamics will clearly depend on the oscillation frequency of this field (i.e. ω_a). It is useful to define the probability amplitudes of the adiabatic and bare states, $A(t)$ and $B(t)$ respectively [17];

$$A(t) = \begin{pmatrix} a_-(t) \\ a_+(t) \end{pmatrix} \qquad B(t) = \begin{pmatrix} b_1(t) \\ b_2(t) \end{pmatrix}, \tag{26}$$

so that $a_-^2 + a_+^2 = 1 = b_1^2 + b_2^2$. Schrödingers equation can then be written down in the basis of bare states:

$$i\dot{B}(t) = H \cdot B, \tag{27}$$

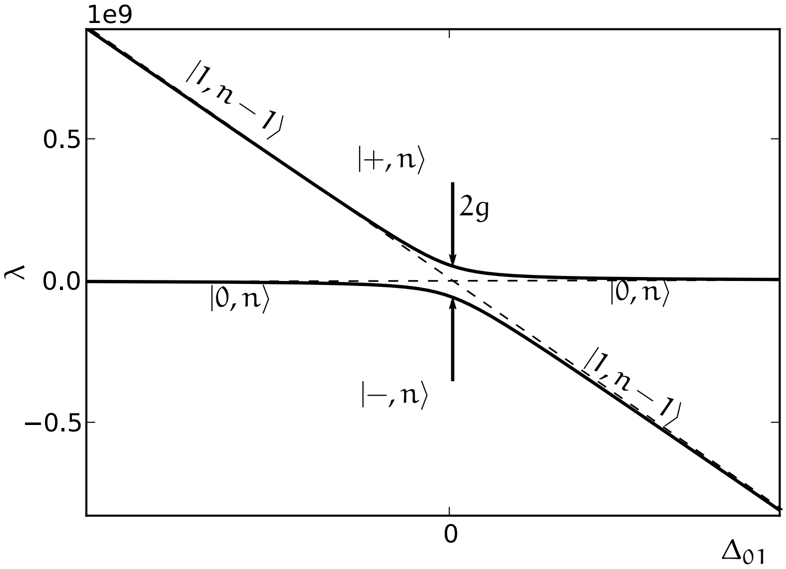

Figure 3: Eigenvalues of the Hamiltonian (17) as function of detuning of the excitation laser. On resonance, the energy curves repel each other, signifying full mixing of the two states. In other words, the two states are coupled.

where H is the Hamiltonian defined earlier in (17). Since the adiabatic states are just rotations of the bare states, their populations are also related by this rotation:

$$B(t) = R[\theta(t)]A(t). \tag{28}$$

So, the statement that the system initially is in $|0,n\rangle$ gets translated as follows:

$$B(0) = \begin{pmatrix} 1 \\ 0 \end{pmatrix} \implies A(0) = \begin{pmatrix} \cos(\theta) \\ \sin(\theta) \end{pmatrix}. \tag{29}$$

With this initial condition, the adiabatic probability amplitudes of the system at a time t (in the presence of a constant laser field) are given by

$$A(t) = \begin{pmatrix} \cos(\theta) \exp(-i\lambda_- t) \\ \sin(\theta) \exp(-i\lambda_+ t) \end{pmatrix}. \tag{30}$$

This results from the time-dependent Schrödinger equation in the adiabatic basis which can be found by starting from the Schrödinger equation for $B(t)$ and using relation (28):

$$i\dot{A}(t) = \left[R(-\theta)H_I R(\theta) - iR(-\theta)\dot{R}(t)\right] A(t) \tag{31}$$

$$= \begin{pmatrix} \lambda_- & -i\dot{\theta} \\ i\dot{\theta} & \lambda_+ \end{pmatrix} A(t) \tag{32}$$

The appearance of the time derivative $\dot{\theta}$ of the mixing angle is worth noting. The time dependence of θ is inherited from the time dependence of g, and indicates that populations could behave differently when subjected to pulsed electromagnetic waves ($\dot{g} \neq 0$) instead of cw irradiation ($\dot{g} = 0$). At this stage, however, set $\dot{g} = 0$ and thus $\dot{\theta} = 0$; only cw lasers are considered.

Combining (30) and utilizing trigonometry then gives for cw laser irradiation [18]

$$\begin{aligned} P_+ &= |\langle 0, n|\Psi(t)\rangle|^2 = |A(0)^\dagger \cdot A(t)|^2 \\ &= 1 - \frac{1}{2}\sin^2(2\theta)\,[1 - \cos(\Omega t)] \\ P_- &= 1 - P_+ \\ &= \frac{1}{2}\sin^2(2\theta)\,[1 - \cos(\Omega t)] \end{aligned} \tag{33}$$

Interestingly, the population oscillates between the two adiabatic states, a phenomenon referred to as *Rabi Oscillations* [19]. The oscillation frequency is determined by both the laser power (through the form of g) and the detuning of the laser Δ_{01}. This dependency of the oscillation frequency on both Δ_{01} and g will have important implications for the numerical simulations performed in later chapters. Note that if the laser field is on resonance and present for half of the oscillation period, the population is completely inverted from the ground state to the excited state.

On the right in figure 4 the population of the excited state $|1\rangle$ as function of detuning Δ_{01} is shown. This evolution as function of time is also shown for two values of Δ_{01} on the left.

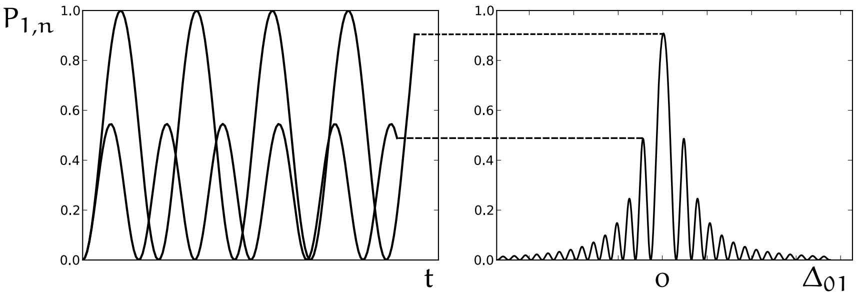

Figure 4: Left: Evolution of the population of the excited state as function of time for two detunings. Right: the population as function of frequency. Note that the time oscillation period is different for different detunings, as well as the maximal population.

2.2 HAMILTONIAN DESCRIPTION OF THE IONIZATION PROCESS

The continuum is a continuous set of infinitely many states. Taking all of these states into account in the same way as the bound states is impossible and instead a method to decrease the population of the atomic system within a Schrödinger equation formalism is required. One solution is to add a non-hermitian term to the Hamiltonian (readers interested in a framework useful for dealing with non-hermitian Hamiltonians might find [20] to be a good starting point). This means that the eigenvalues of the Hamiltonian will no longer be real. The imaginary component of the eigenvalues will cause an exponential damping of the populations.

Since the applied ionizing laser field only provides enough energy to promote electrons in the excited state to the continuum, the following Hamiltonian can be added:

$$H_{\text{add}} = \begin{pmatrix} 0 & 0 \\ 0 & -i\frac{\Gamma}{2} \end{pmatrix}, \tag{34}$$

where Γ determines the ionization strength. This form clearly indicates that ionization directly from the ground state is impossible. $\Gamma = \sigma \cdot P_2$, where σ is the photo-ionization cross section and P_2 is the power density of the ionizing laser. This intuitive approach is simplistic, and is insufficient for the more general multi-level case. A more rigorous treatment is called for.

The effect of an ionizing laser on discrete states will be derived from first principles following an approach based on [11] and expanding on earlier research for nuclear laser spectroscopy [2] which was based on a different approach outlined in [21] and [22]. It will be shown that the approach used in this thesis will result in effects not included in the earlier work.

Consider a single bound state $|1\rangle$ and a continuum of states $|\varepsilon, \omega_\varepsilon\rangle$, labeled by some continuous parameter ε. The laser field that couples this discrete state to the set of continuum states will be assumed to result in a coherent coupling given by $V = V(t)\cos(\omega_b t + \Phi(t))$, where ω_b is the frequency of the laser field.

The wave function of the atomic system consisting of a state $|1\rangle$ and the continuum at a certain time t can be written in the bare states basis as

$$|\Psi, t\rangle = b_1(t) + \int d\varepsilon\ b_\varepsilon\, |\varepsilon, \omega_\varepsilon\rangle\,. \tag{35}$$

Applying Schrödinger's equation reveals how the coefficients a evolve under influence of the laser field $V(t)$:

$$i\dot{b}_1 = \omega_1 b_1 - \int d\varepsilon\, \langle 1\, |V(t)|\, \varepsilon, \omega_\varepsilon\rangle \cos(\omega_b t + \Phi) b_\varepsilon, \tag{36}$$

$$i\dot{b}_\varepsilon = \omega_\varepsilon b_\varepsilon - \langle \varepsilon, \omega_\varepsilon\, |V(t)|\, 1\rangle \cos(\omega_b t + \Phi) b_\varepsilon. \tag{37}$$

Start by making the transformation

$$c_j = b_j \exp(i\omega_j t) \tag{38}$$

and introduce the detuning $\Delta_{\varepsilon 1} = \omega_\varepsilon - \omega_1 - \omega_b$. This change of variables makes the transformation to co-rotating coordinates and is particularly well suited for further calculations. Making the Rotating Wave approximation, equations (36) and (37) become

$$i\dot{c}_1 = -\frac{1}{2}\int d\varepsilon \, \langle 1\,|V(t)|\,\varepsilon\rangle \exp\left(i\Phi - i\Delta_{\varepsilon 1}\right) c_\varepsilon, \tag{39}$$

$$i\dot{c}_\varepsilon = -\frac{1}{2}\,\langle \varepsilon\,|V(t)|\,1\rangle \exp\left(i\Phi - i\Delta_{\varepsilon 1}\right) c_1. \tag{40}$$

By formally integrating equation (40) and plugging it into equation (39), an integrodifferential equation for $c_1(t)$ can be found:

$$\dot{c}_1(t) = -\frac{1}{4}\int d\varepsilon \int_0^t dt' \, \langle 1\,|V(t)|\,\varepsilon, \omega_\varepsilon\rangle \langle \varepsilon, \omega_\varepsilon\,\left|V(t')\right|\,1\rangle \\ \times \exp\left(-i\Delta_\varepsilon(t-t') + i(\Phi(t) - \Phi(t'))\right) c_1(t'). \tag{41}$$

The switch to integrating over the energy of the continuum states instead of the label ε is now made. Introducing the density of states $\rho(\omega_\varepsilon)$, the previous equation becomes

$$\dot{c}_1(t) = -\frac{1}{4}\int_0^\infty d\omega_\varepsilon \int_0^t dt' \, \rho(E)\,|\langle 1\,|V(t)|\,\varepsilon, \omega_\varepsilon\rangle|^2 \\ \times \exp\left(-i\Delta_\varepsilon(t-t') + i(\Phi(t) - \Phi(t'))\right) c_1(t'). \tag{42}$$

To proceed analytically, an approximation has to be made, which assumes that the matrix elements $\langle 1\,|V(t)|\,\varepsilon\rangle$ only slowly depend on ε, and that they have a large width χ. Note that the oscillatory term $\exp\left(-i\Delta_\varepsilon(t-t')\right)$ in the integral has a period proportional to $1/(t-t')$. The only non-zero contributions to the total integral will therefore be the contributions of the t' for which $|t-t'| \lesssim 1/\chi$. Taking $\chi \to \infty$ then yields the Markov approximation [11]: $\dot{c}_1(t)$ is only influenced by $c_1(t'=t)$. So,

$$\dot{c}_1(t) = -\frac{c_1}{4}\int_0^\infty d\omega_\varepsilon \rho(\omega_\varepsilon)\,|\langle 1\,|V(t)|\,\varepsilon, \omega_\varepsilon\rangle|^2 \int_0^t dt' \\ \times \exp\left(-i\Delta_{\varepsilon 1}(t-t')\right) \tag{43}$$

This approach is valid for structureless continua. Note that the phases have disappeared. The time integral can be approximated by integrating from $-\infty$ to t instead of from 0 to t. This approximation is justified because of the argument given in favor of the Markov approximation: the integral is zero anyway for $|t-t'| \gtrsim 1/\chi$. Notice now that the time integral is the Fourier transform of the Heaviside function. Integral (43) becomes [23]

$$\dot{c}_1(t) = -\frac{c_1(t)}{4}\int_0^\infty d\omega_\varepsilon \,|\langle 1\,|V(t)|\,\varepsilon, \omega_\varepsilon\rangle|^2 \rho(\omega_\varepsilon) \\ \times \left[i\mathcal{P}(1/\Delta_{\varepsilon 1}) + \pi\delta(\Delta_{\varepsilon 1})\right] \tag{44}$$

where $\mathcal{P}$ is the principal part and δ is the delta function. Now define

$$\Gamma(\omega_\varepsilon, t) = \frac{\pi}{2} \left|\langle 1 \left|V(t)\right| \varepsilon, \omega_\varepsilon\rangle\right|^2 \rho(\omega_\varepsilon), \tag{45}$$

$$\begin{aligned} \delta\omega(t) &= \frac{1}{4}\mathcal{P}\int_0^\infty d\omega_\varepsilon\ \rho(\omega_\varepsilon)\frac{\left|\langle 1 \left|V(t)\right| \varepsilon, \omega_\varepsilon\rangle\right|^2}{\Delta_{\varepsilon 1}} \\ &= \frac{1}{2\pi}\mathcal{P}\int_0^\infty d\omega_\varepsilon \frac{\Gamma(\omega_\varepsilon)}{\Delta_{\varepsilon 1}}, \end{aligned} \tag{46}$$

$\Gamma(\omega_\varepsilon, t)$ is the strength of the coupling of the discrete state to the states in the continuum in the shell of energy ω_ε. The delta function in equation (44) motivates the definition $\Gamma(t) = \Gamma(\omega_\varepsilon = \omega_1 + \omega_b, t)$. This is the coupling of the discrete state to the state at which the laser plus bound state is tuned. In practical applications, however, the laser has a certain linewidth and it then makes more sense to define $\Gamma(t)$ as the integral of $\Gamma(\omega_\varepsilon, t)$ over all the ε the laser can reach.

The interpretation of the two quantities $\delta\omega$ and Γ can be illustrated by considering constant laser powers. Then

$$\dot{c}_1(t) = -\left(i\delta\omega + \frac{\Gamma}{2}\right) c_1(t), \tag{47}$$

and therefore

$$c_1(t) = e^{-\Gamma t} e^{-i\delta\omega t} c_1(0). \tag{48}$$

Going back to the original expansion coefficients b, the evolution of the probability amplitude of the bare states can be found:

$$b_1(t) = e^{-\Gamma t} e^{-i(\omega_1 + \delta\omega)t} b_1(0) \tag{49}$$

The term $\delta\omega$ is an energy shift of the bound state due to the coupling with the continuum, and could be called a dynamical bound-continuum Stark shift [24]. An example of a Stark shift was already encountered earlier in the form of the energy splitting (25) due to the resonant laser step [25], this time due to the bound-bound interactions. For an example of both theoretical and experimental values of the Stark shift, see e.g. [26].

The size of shift (46) could in principle be computed by calculating the matrix elements of the transition to the continuum states. This is usually done by atomic mean-field calculations. The evolution of the population of the system is not influenced by this shift, so they will usually just be absorbed in the definitions of the energy of the states. Typically, the shifts are small unless the power density becomes really high [27]. Moreover, since the energy difference of the excited states is the main parameter of interest, the only important quantity is the relative shift of these states. Since the states in the excited hyperfine multiplet all have similar electronic wave functions, this relative shift should be small.

Finally, note that the factor Γ is the same as the one defined in equation (34) (per definition of the ionization cross section) and that definition given in (45) links it to first principles. In practice, the relation $\Gamma = \sigma P_2$ is more useful and is adopted for the simulations in this work.

2.3 COMBINING RESONANT EXCITATION AND NON-RESONANT IONIZATION

The results of the previous two sections can now be used to construct one Hamiltonian describing both processes:

$$H_{\text{tot}} = \begin{pmatrix} \omega_0 & g(t) \\ g^*(t) & \omega_1 - \omega_a - i\frac{\Gamma(t)}{2} + \delta\omega_1(t) \end{pmatrix} \tag{50}$$

For notational convenience, the unknown Stark shift $\delta\omega_1(t)$ is absorbed into the energy ω_1. By utilizing the frequency detuning $\Delta_{01} = \omega_1 - \omega_0 - \omega_a$, this can be rewritten relative to ω_0 as

$$H_{\text{tot}} = \begin{pmatrix} 0 & g(t) \\ g^*(t) & \Delta_{01} - i\frac{\Gamma(t)}{2} \end{pmatrix} \tag{51}$$

without changing any of the dynamics. This Hamiltonian, here expressed in the bare state basis, can be rewritten in the basis of the adiabatic states introduced in equations (20) and (21). The definition of the mixing angle θ is kept and the adiabatic states are now the instantaneous eigenstates of the real part of Hamiltonian (51). Equation (32) becomes [17]:

$$i\dot{A}(t) = \begin{pmatrix} \lambda_- - \frac{1}{2}\Gamma\sin^2\theta & -i\dot{\theta} - \frac{i}{4}\Gamma\sin 2\theta \\ i\dot{\theta} - \frac{i}{4}\Gamma\sin 2\theta & \lambda_+ - \frac{1}{2}\Gamma\cos^2\theta \end{pmatrix} A(t) \tag{52}$$

2.3.1 *Solution for a Two-Level Atom*

Schrödingers equation with Hamiltonian (51) can be solved in the case of constant laser powers. The eigenvalues of H_{tot} are

$$\begin{aligned} \lambda_\pm^{\text{tot}} &= \frac{1}{2}\left(\Delta_{01} - \frac{i\Gamma}{2} \pm \sqrt{4g^2 + \left(\Delta_{01} - i\frac{\Gamma}{2}\right)^2}\right) \\ &= \frac{1}{2}\left(\Delta_{01} - \frac{i\Gamma}{2} \pm \sqrt{4g^2 + \Delta_{01}^2 - \frac{\Gamma^2}{4} - i\Delta_{01}\Gamma}\right) \end{aligned} \tag{53}$$

Note that the real part of the eigenvalues contains a contribution of the diagonal term $i\Gamma$. **This means that the energy splitting**

of the states will be different in the presence of the second laser; this can be considered another example of a Stark shift. The imaginary part will cause an exponential damping of the population in both of the eigenstates of the Hamiltonian. The real and imaginary parts of eigenvalues (53) are shown in figure 5. The curve of the real parts of the eigenvalues of course still repel, while the imaginary parts of the eigenvalues switch places near the resonance. Calculating the evolution of the populations

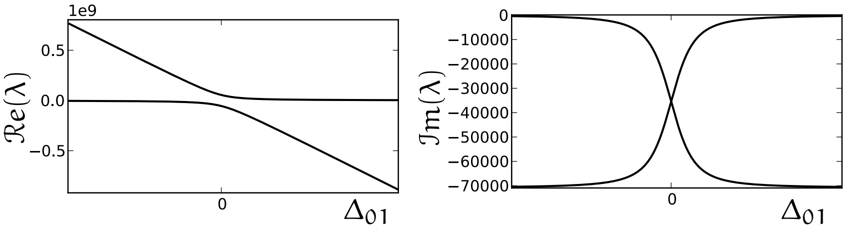

Figure 5: Real (left) and Imaginary (right) parts of the eigenvalues of Hamiltonian (51) as function of the detuning of the first laser. Note once again the repelling of the real part of the eigenvalues, and the reversal of the imaginary parts of the eigenvalues.

is still possible analytically [2]:

$$P_{0n} = \left| \frac{\Delta_{01} + i\Gamma \sin \Omega t + i\Omega \cos \Omega t}{\Omega} \right|^2 e^{-\Gamma t}$$
$$P_{1n} = \left| \frac{g}{\Omega} \sin \Omega t \right|^2 e^{-\Gamma t}, \tag{54}$$

where $\Omega = \lambda_-^{\text{tot}} - \lambda_+^{\text{tot}}$. The exponential damping is clearly expressed by the factor $e^{-\Gamma t}$, but it should be kept in mind that Ω is complex so that the goniometric functions of Ω also behave like exponential terms. In figure 6 the population of the excited state is shown (on resonance, so $\Delta_{10} = 0$), as well as the population that has escaped the system from $t = 0$ until a certain time t', as function of the laser-atom detuning. This graph was made by solving Schrödingers equation numerically. The Rabi ocillations are clearly damped, and a smooth resonance in the ionization rate I can be observed. I is defined as

$$I = 1 - P_{1,n} - P_{0,n}. \tag{55}$$

The ionization curve is quite smooth, since the simulation spans a few Rabi cycles and the rate is averaged over these cycles. There is still a slight oscillation superimposed on the Lorentzian shape, but it is very small. Chapter 4 will show that the inclusion of the pulse shape of the laser removes even these small oscillations.

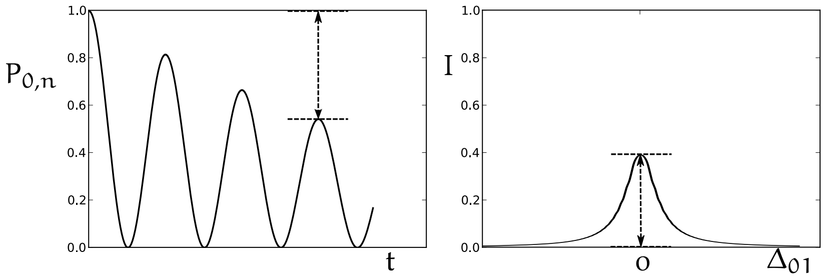

Figure 6: Left: Evolution of the population of the ground state as function of time with $\Delta_{10} = 0$. When this curve is maximal, all of the population is in the ground state. The population deficit has been ionized. Right: the ionization rate as function of frequency. This curve is smooth, but some small oscillations can be seen. The dotted lines are there to visually support the idea that population missing from the atomic system has been ionized.

2.4 POWER BROADENING FOR SIMULTANEOUS EXCITATION AND IONIZATION

Power broadening refers to the increase of the width of a resonance with increasing laser powers [28]. Power broadening is therefore usually not desirable, since it reduces the experimental resolution: two close-lying resonances could be hidden underneath one wide signal. On the other hand, increasing the laser powers also results in an increased total experimental efficiency, which is of course desirable. Therefore a balance must be found between resolution and efficiency.

Since the CRIS experiment uses at least two lasers, there are two possible sources of power broadening. This section studies the influence of both lasers on the width of the resonance. First, the resonant excitation step is treated.

2.4.1 *Power Broadening in the Jaynes-Cummings Model*

The analytical solution for the populations of a two-level atom subjected to a single resonant laser field was given in (33):

$$P_{1,n} = \frac{1}{2}\sin^2(2\theta)\left[1 - \cos(\Omega t)\right] \tag{56}$$

The laser power enters this expression through the coupling g, which is related to both θ and Ω:

$$\theta(t) = \frac{1}{2}\arctan\frac{2g(t)}{\Delta_{01}} \tag{57}$$

$$\Omega = \lambda_+ - \lambda_- = \sqrt{4g^2(t) + \Delta_{01}^2}. \tag{58}$$

In laser spectroscopic experiments like CRIS, the oscillations in time in equation (56) are not observed. This can be attributed to the fact that experimental conditions never allow coherence to be perfectly maintained, e.g. due to fluctuations in for example the laser power or in the phases of the electronic wavefunctions of the atomic ensemble. In other words, $1 - \cos(\Omega t) \approx 1$. The maximal experimental excited population $P_{1n}^{\exp}$ is then solely determined by $1/2 \sin^2(2\theta)$:

$$P_{1n}^{\exp} = \frac{1}{2}\sin^2(2\theta) \tag{59}$$

Looking at equation (57), two cases should be distinguished:

1. $|\Delta_{01}| \ll g$. On resonance, the denominator dominates the argument of (57) so that $\theta \approx \frac{\pi}{4}$, regardless of laser power.

2. $|\Delta_{01}| \gtrsim g$. Off resonance, the denominator does not dominate the argument of (57): as g increases, θ only slowly evolves towards $\frac{\pi}{4}$. The larger the detuning, the longer it takes for the excitation probability to saturate. The behaviour of $P_{1,n}^{\exp}$ for three fixed detunings is shown in figure 7.

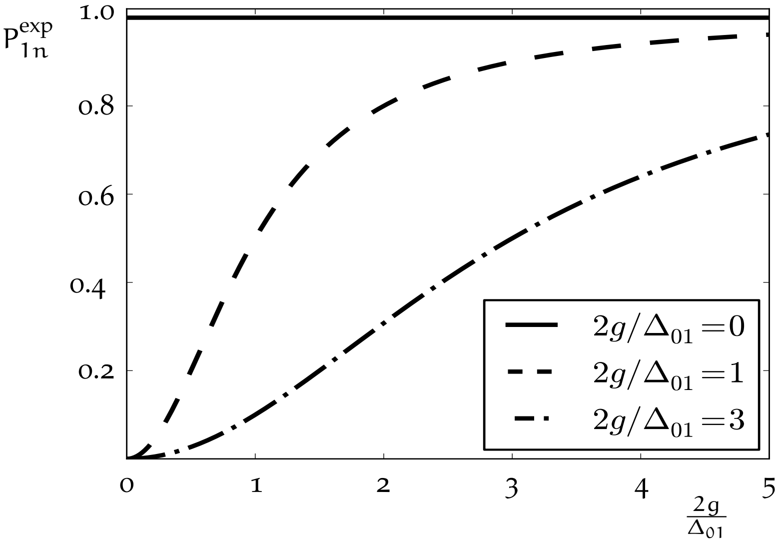

Figure 7: Plot of the function $P_{1n}^{\exp} = \frac{1}{2}\sin^2(2\theta)$ as a function of $\frac{2g(t)}{\Delta_{01}}$ for a few fixed detunings .

The population saturates at a lower laser power on resonance than in the tails of the peak. At a certain point, increasing the power of the laser will only make the tails of the resonance go up, while the efficiency on resonance remains the same (since it is already close to optimal). The observed resonance will therefore get wider with increasing laser power.

Another way of looking at this is that as the power is increased, the probability of stimulated emission increases. This implies that the lifetime of the excited state decreases, which in turn implies that the absolute uncertainty on the lifetime decreases. By virtue of the time-energy uncertainty relation

$$\Delta E \Delta \tau \geqslant \frac{1}{2}, \tag{60}$$

the uncertainty on the energy increases; the resonance becomes broader. Figure 8 shows the broadening of the population profiles of the excited state for four different laser powers, each one ten times larger than the previous one. The oscillations are not averaged out in these simulations, but the increasing width of the envelopes can clearly be seen.

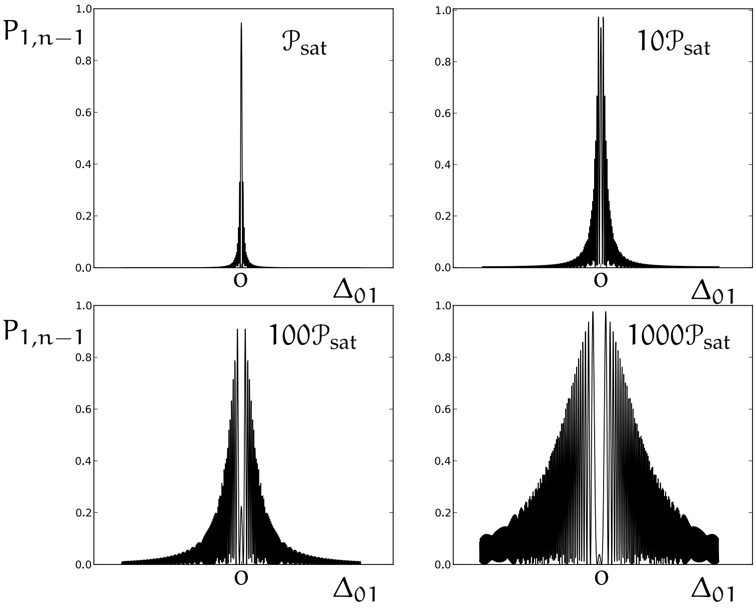

Figure 8: Population of the excited state for four excitation laser powers, each one ten times larger than the previous.

2.4.2 *Power Broadening due to Ionization*

An ionization step introduces an additional decay channel for the electrons in the excited state. Not only can the electrons be stimulated back to the ground state, they can now also 'decay' into one of the continuum states. So, the half life of the excited state is reduced and the the excited state therefore gets broadened. Since the energy probing done by the first laser is sensitive to this energy width if both lasers fire simultaneously, the measured resonance will broaden. Based on this argument, the resonances will not broaden if the ionization step takes place after the excitation pulse has stopped. This will be discussed further in chapter 6.

Figure 9 plots the linewidth of the ionization signal as a function of the laser power of the second laser expressed relative to the saturation power (see figure 10 for a saturation curve). These widths were obtained by fitting the simulated data with a Lorentzian, which resulted in an essentially perfect fit. Figure 10 shows the ionization rate for the same laser powers. Comparing these two figures reveals that power broadening occurs even when the ionization process is not yet saturated.

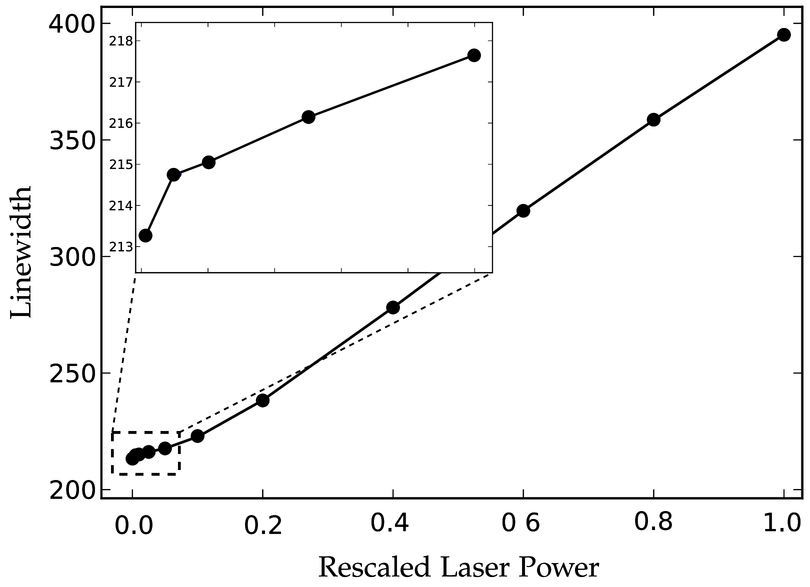

Figure 9: Linewidth in MHz as function of rescaled ionization laser power, with constant power in the first step. The fitting errors are smaller than the dots.

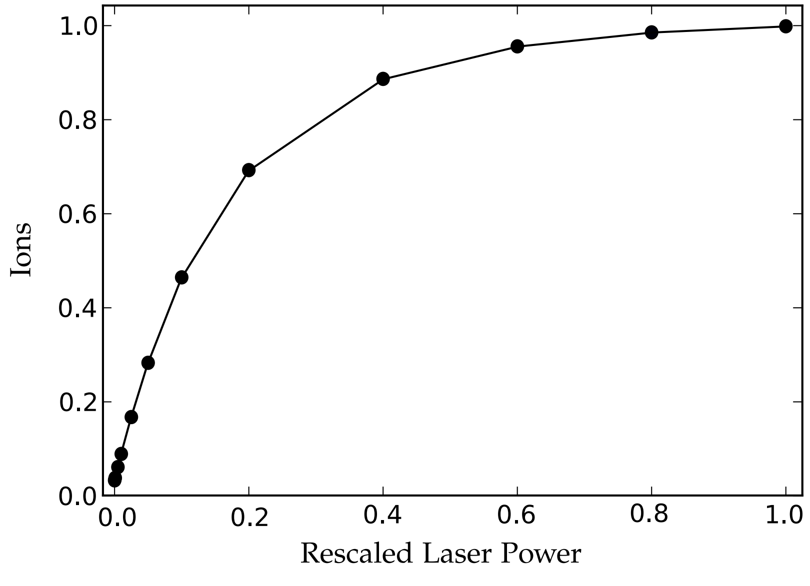

Figure 10: Ionization rate as function of rescaled ionization laser power. The fitting errors are smaller than the dots (and since these are simulations there are no other errors).

3

RESONANT LASER IONIZATION: MULTI-LEVEL ATOMS

The goal of this chapter is to generalize the results of chapter 2 to more than two levels. Consider a system made up of two groups of states, one of which will be called the ground state multiplet, containing k states, and the other the *excited state multiplet*, containing l states.

3.1 RESONANT EXCITATION IN A MULTI-LEVEL ATOM

The Hamiltonian governing resonant excitations is a straightforward generalization of the two-level Hamiltonian (see equation (61)). Note that this is a block matrix with four blocks: there's a diagonal block that contains the electronic energies of the ground state multiplet and a block with the electronic energies of the excited state multiplet minus the energy of a laser photon. The two other blocks contain the couplings g and are each others hermitian conjugate (in this case just the transpose, since the couplings are real).

$$\left(\begin{array}{cccc||cccc}
\omega_{i_1} & 0 & \dots & 0 & g_{i_1,f_1} & g_{i_1,f_2} & \dots & g_{i_1,f_l} \\
0 & \omega_{i_2} & \dots & 0 & g_{i_2,f_1} & g_{i_2,f_2} & \dots & g_{i_2,f_l} \\
\vdots & \vdots & \ddots & \vdots & \vdots & \vdots & \ddots & \vdots \\
0 & 0 & \dots & \omega_{i_k} & g_{i_k,f_1} & g_{i_k,f_2} & \dots & g_{i_k,f_l} \\
\hline\hline
g_{i_1,f_1} & g_{i_2,f_1} & \dots & g_{i_k,f_1} & \omega_{f_1}-\omega_a & 0 & \dots & 0 \\
g_{i_1,f_2} & g_{i_2,f_2} & \dots & g_{i_k,f_2} & 0 & \omega_{f_2}-\omega_a \dots & 0 & \\
\vdots & \vdots & \ddots & \vdots & \vdots & \vdots & \ddots & \vdots \\
g_{i_1,f_l} & g_{i_2,f_l} & \dots & g_{i_k,f_l} & 0 & 0 & \dots & \omega_{f_l}-\omega_a
\end{array}\right). \tag{61}$$

This is the description of resonant excitation for larger systems: a straightforward generalization of the two-level case. In figure 11 the eigenvalues of Hamiltonian (61) are shown as function of the detuning for the specific case of a spin 1 nucleus and a ground-state electron spin $\frac{1}{2}$ and excited-state electron spin $\frac{3}{2}$, with a A_{lower} = 4GHz and A_{upper}= 300 MHz. This system has a ground state doublet and a triplet of excited states, so $k = 2$ and $l = 3$. Note how the mixing of the states causes repelling of the eigenvalue curves. Angular momentum conservation forbids the transition from a state with total angular momentum $\frac{1}{2}$ to a state with total angular momentum $\frac{5}{2}$, so at the energy of this transition the purple and cyan eigenvalue curves intersect instead of repelling. The frequencies at which the mixings occur are exactly the frequencies at which peaks will be observed in the hyperfine scans.

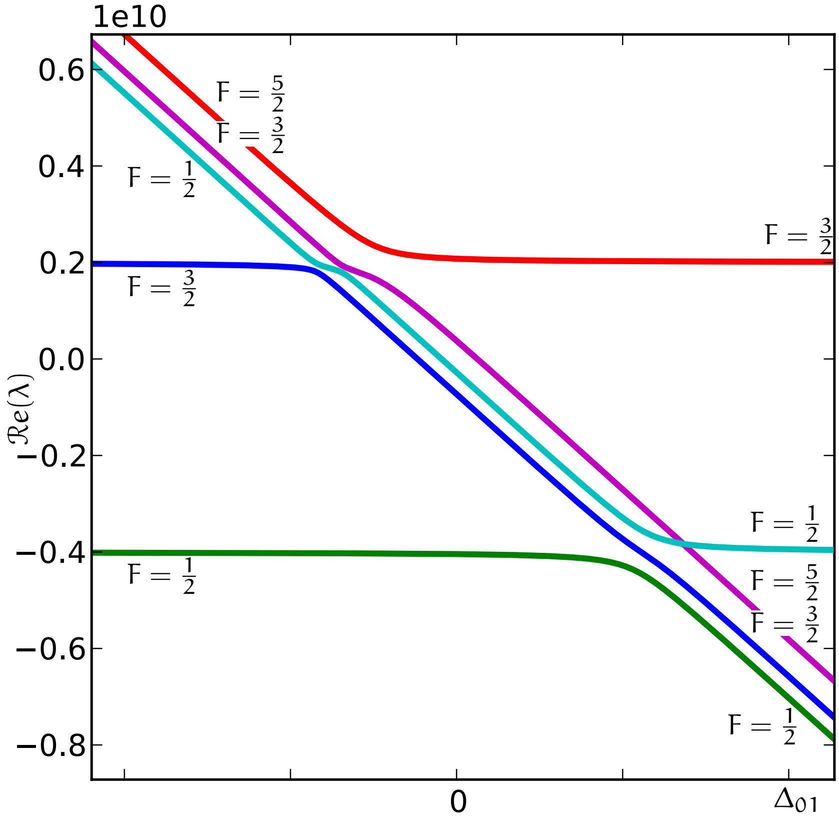

Figure 11: (Colour) Eigenvalues of Hamiltonian (61) as function of the detuning of the first laser, for the specific case of a spin 1 nucleus and spin $\frac{1}{2}$ and spin $\frac{3}{2}$ ground and excited electronic states. Note how the purple and cyan curve intersect.

3.2 IONIZATION FOR MULTI-LEVEL ATOMS

The naive approach to adding an ionization mechanism to the description made so far adds factors $-i\Gamma$ and Stark Shifts to the diagonal of the bottom right block of (61). These shifts could be different for each of the excited states. This approximation represents a starting point rather than the whole story, however. A more rigorous derivation is presented next.

3.2.1 *A Doublet of States coupled to one Continuum*

Consider a system with two states with energy ω_1 and ω_2 that are both coupled to the continuum by the same laser field with frequency ω_b Understanding the interaction terms requires repeating the derivations carried out in section 2.2, with some additional considerations. Applying Schrödingers equation to the state vector of the system

$$|\Psi, t\rangle = a_1(t) + a_2(t) + \int d\varepsilon a_\varepsilon \, |\varepsilon, \omega_\varepsilon\rangle \tag{62}$$

yields the time evolution of the coefficients a:

$$i\dot{a}_1 = \omega_1 a_1 - \int d\varepsilon \, \langle 1 \, |V(t)| \, \varepsilon, \omega_\varepsilon\rangle \cos(\omega_b t + \Phi) a_\varepsilon, \tag{63}$$

$$i\dot{a}_2 = \omega_2 a_2 - \int d\varepsilon \, \langle 2 \, |V(t)| \, \varepsilon, \omega_\varepsilon\rangle \cos(\omega_b t + \Phi) a_\varepsilon, \tag{64}$$

$$\begin{aligned} i\dot{a}_\varepsilon = \omega_\varepsilon a_\varepsilon &- \langle \varepsilon, \omega_\varepsilon \, |V(t)| \, 1\rangle \cos(\omega_b t + \Phi) a_1 \\ &- \langle \varepsilon, \omega_\varepsilon \, |V(t)| \, 2\rangle \cos(\omega_b t + \Phi) a_2. \end{aligned} \tag{65}$$

Once again, the transformation (38) is used and $\Delta_{\varepsilon 1} = \omega_\varepsilon - \omega_1 - \omega_b$ and $\Delta_{\varepsilon 2} = \omega_\varepsilon - \omega_2 - \omega_b$ are introduced. The Rotating Wave Approximation is then made. Following the methods applied in section 2.2 then yield

$$\begin{aligned} \dot{c}_1(t) = &-\frac{1}{4}\int d\varepsilon \int_0^t dt' \, |\langle 1 \, |V(t)| \, \varepsilon, \omega_\varepsilon\rangle|^2 \\ &\qquad \times \exp\left(-i\Delta_{\varepsilon 1}(t - t') + i(\Phi(t) - \Phi(t'))\right) c_1(t') \\ &-\frac{1}{4}\int d\varepsilon \int_0^t dt' \, \langle 1 \, |V(t)| \, \varepsilon, \omega_\varepsilon\rangle \langle \varepsilon, \omega_\varepsilon \, \left|V(t')\right| \, 2\rangle \\ &\qquad \times \exp\left(-i\Delta_{\varepsilon 1} t + i\Delta_{\varepsilon 2} t' + i(\Phi(t) - \Phi(t'))\right) c_2(t') \end{aligned} \tag{66}$$

$$\begin{aligned} \dot{c}_2(t) = &-\frac{1}{4}\int d\varepsilon \int_0^t dt' \, |\langle 2 \, |V(t)| \, \varepsilon, \omega_\varepsilon\rangle|^2 \\ &\qquad \times \exp\left(-i\Delta_{\varepsilon 2}(t - t') + i(\Phi(t) - \Phi(t'))\right) c_2(t') \\ &-\frac{1}{4}\int d\varepsilon \int_0^t dt' \, \langle 2 \, |V(t)| \, \varepsilon, \omega_\varepsilon\rangle \langle \varepsilon, \omega_\varepsilon \, \left|V(t')\right| \, 1\rangle \\ &\qquad \times \exp\left(i\Delta_{\varepsilon 1} t' - i\Delta_{\varepsilon 2} t + i(\Phi(t) - \Phi(t'))\right) c_1(t') \end{aligned} \tag{67}$$

These equations allow the identification of interactions not included in the intuitive model at the beginning of this section. The evolution of the two states is coupled, which is made apparent by the third line of equations (66) and (67). The evolution of the amplitude of one state is also determined by the matrix elements and amplitudes related to the other state. Using the

Markov Approximation to simplify equations (66) and (67) results in

$$\begin{aligned}\dot{c}_1 =& -\frac{c_1}{4}\int_0^\infty d\omega_\varepsilon\, \left|\langle 1\,|V(t)|\,\varepsilon,\omega_\varepsilon\rangle\right|^2 \rho(\omega_\varepsilon)\,[i\mathcal{P}(1/\Delta_{\varepsilon 1}) + \pi\delta(\Delta_{\varepsilon 1})]\\ & -\frac{c_2}{4}\int_0^\infty d\omega_\varepsilon\, \langle 1\,|V(t)|\,\varepsilon,\omega_\varepsilon\rangle\,\langle \varepsilon,\omega_\varepsilon\,|V(t)|\,2\rangle\,\rho(\omega_\varepsilon)\\ & \times \exp\left[i(\Delta_{\varepsilon 1} - \Delta_{\varepsilon 2})t\right]\cdot[i\mathcal{P}(2/(\Delta_{\varepsilon 1} + \Delta_{\varepsilon 2})) + \pi\delta(\Delta_{\varepsilon 1} + \Delta_{\varepsilon 2})]\end{aligned} \tag{68}$$

$$\begin{aligned}\dot{c}_2 =& -\frac{c_2}{4}\int_0^\infty d\omega_\varepsilon\, \left|\langle 2\,|V(t)|\,\varepsilon,\omega_\varepsilon\rangle\right|^2 \rho(\omega_\varepsilon)\,[i\mathcal{P}(1/\Delta_{\varepsilon 2}) + \pi\delta(\Delta_{\varepsilon 2})]\\ & -\frac{c_1}{4}\int_0^\infty d\omega_\varepsilon\, \langle 2\,|V(t)|\,\varepsilon,\omega_\varepsilon\rangle\,\langle \varepsilon,\omega_\varepsilon\,|V(t)|\,1\rangle\,\rho(\omega_\varepsilon)\\ & \times \exp\left[-i(\Delta_{\varepsilon 1} - \Delta_{\varepsilon 2})t\right]\cdot[i\mathcal{P}(2/(\Delta_{\varepsilon 1} + \Delta_{\varepsilon 2})) + \pi\delta(\Delta_{\varepsilon 1} + \Delta_{\varepsilon 2})]\end{aligned} \tag{69}$$

Define similarly to equations (45) and (46),

$$\Gamma_{ij}(\omega_\varepsilon) = \frac{\pi}{2}\langle i\,|V(t)|\,\varepsilon,\omega_\varepsilon\rangle\,\langle \varepsilon,\omega_\varepsilon\,|V(t)|\,j\rangle\,\rho(\omega_\varepsilon) \tag{70}$$

$$\delta\omega_{ij} = \frac{1}{2\pi}\mathcal{P}\int_0^\infty d\omega_\varepsilon\,\frac{2\Gamma_{ij}(\omega_\varepsilon)}{\Delta_{\varepsilon i} + \Delta_{\varepsilon j}} \tag{71}$$

$$q_{ij} = \frac{\delta\omega_{ij}(t)}{\Gamma_{ij}(t)}. \tag{72}$$

Γ_{ij} contains a product of matrix elements of the coupling of state $|i\rangle$ and $|j\rangle$ to the continuum. This enables the interpretation that the off-diagonal Γ_{ij} couplings are there because the bound states are coupled to one and the same continuum, and are hence coupled to one another. $\delta\omega_{ij}$ is then an energy shift due to these couplings. In the off-diagonal couplings a parameter q appears. The notation q is chosen for historical reasons. This parameter is called the *Fano* q *parameter* [29]. This parameter signifies that the ionization step also embeds the discrete state in the continuum; there are now states in the continuum that can be distinguished from the others. Ionization from a bound state to a continuum that is structured by the embedding of another bound state results in enhanced or suppressed ionization rates due to interference effects of the ionization channels of these newly embedded dressed states (see e.g. [30] for a theoretical discussion of this phenomenon). **This can happen in the case of CRIS for sufficiently large ionizing laser powers**; the dressed states consisting of laser photons of the second laser and the states of the excited multiplet give a certain structure to the continuum. q can be related to the ratio of the decay rates to the original structureless continuum and the now structured continuum. Typical experimental values range from 0 to 10 (see [31, 32, 33, 34, 35, 36] for published values in several different elements).

With these definitions the equations further simplify and the time evolution of the amplitudes c_1 and c_2 can be expressed as follows:

$$\begin{pmatrix} \dot{c}_1 \\ \dot{c}_2 \end{pmatrix} = \begin{pmatrix} \delta\omega_{11} - \frac{i}{2}\Gamma_{11} & -\frac{1}{2}\Gamma_{12}(q_{12}+i)\exp\left[i(\Delta_{\varepsilon 1}-\Delta_{\varepsilon 2})t\right] \\ -\frac{1}{2}\Gamma_{21}(q_{12}+i)\exp\left[-i(\Delta_{\varepsilon 1}-\Delta_{\varepsilon 2})t\right] & \delta\omega_{22} - \frac{i}{2}\Gamma_{22} \end{pmatrix} \begin{pmatrix} c_1 \\ c_2 \end{pmatrix}. \tag{73}$$

Note that $\Delta_{\varepsilon 1} - \Delta_{\varepsilon 2} = \omega_2 - \omega_1$. So, reversing the transformation (38) will remove the exponentials in the off-diagonal and restore the energy terms to the diagonal:

$$\begin{pmatrix} \dot{a}_1 \\ \dot{a}_2 \end{pmatrix} = H_{\text{ion}} \begin{pmatrix} a_1 \\ a_2 \end{pmatrix} = \begin{pmatrix} \omega_1 + \delta\omega_{11} - \frac{i}{2}\Gamma_{11} & -\frac{1}{2}\Gamma_{12}(q_{12}+i) \\ -\frac{1}{2}\Gamma_{21}(q_{12}+i) & \omega_2 + \delta\omega_{22} - \frac{i}{2}\Gamma_{22} \end{pmatrix} \begin{pmatrix} a_1 \\ a_2 \end{pmatrix}. \tag{74}$$

The Hamiltonian (74) differs from the intuitive version in the beginning of this section. The diagonal terms are as expected, but the off-diagonal terms indicate a coupling of the two states. Note that this coupling is not a direct coupling of the two states as is the case for resonant excitations, but an indirect coupling induced by the interaction of the discrete states with the common continuum. There is population transfer among bound states via the continuum (see figure 12 for a pictorial illustration). The influence on the ionization spectra is illustrated in figure 13 for the particular case of a singlet ground state and a doublet of excited states. This figure shows the difference between a spectrum obtained with and without the ionization-induced couplings. The dashed lines indicate the position of the maxima of the ionization curves. A clear repelling and asymmetrization of the peaks can be observed. The implications on the hyperfine parameters that are extracted form such ionization spectra will be discussed in chapter 5. Considerable effort has been devoted to understanding how this mechanism can be utilized to get efficient transfer among bound states, both from the theoretical viewpoint [31] and the experimental side [37]. Recently, some attention has also been given to the opposite goal, namely that of avoiding these transfers and optimizing the ionization efficiency [38]. It is interesting to note that in all of this research the dynamic Stark shifts and Fano q parameters play a very important role. The firing time of the pulsed lasers is also an important parameter, as is perhaps best illustrated in [38]. This degree of freedom will be further explored in chapter 5.

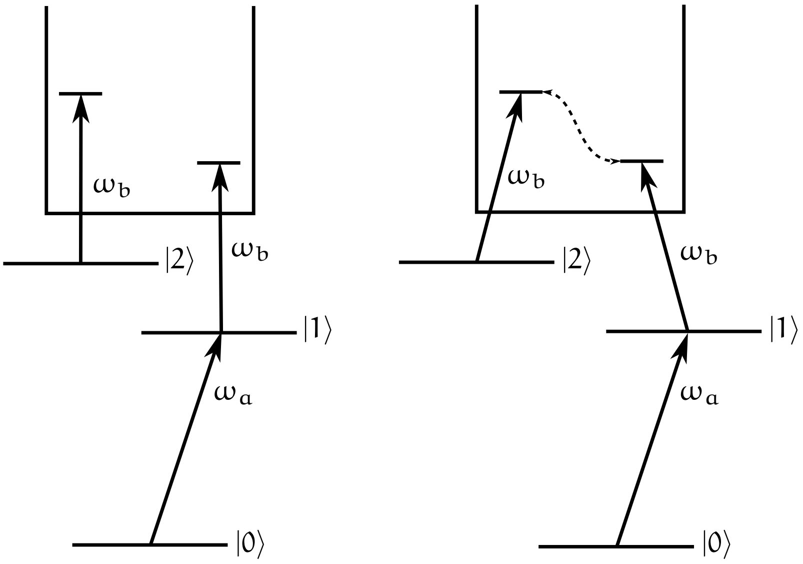

Figure 12: A single ground state resonantly coupled to one of the states in an excited doublet by laser a. This doublet is then coupled to the continuum by a second laser b. Left: Pictogram of direct ionization events from the discrete states. Right: Couplings of the dressed states in the continuum. These couplings lead to interference effects which can alter the ionization cross section, as is illustrated in figure 13.

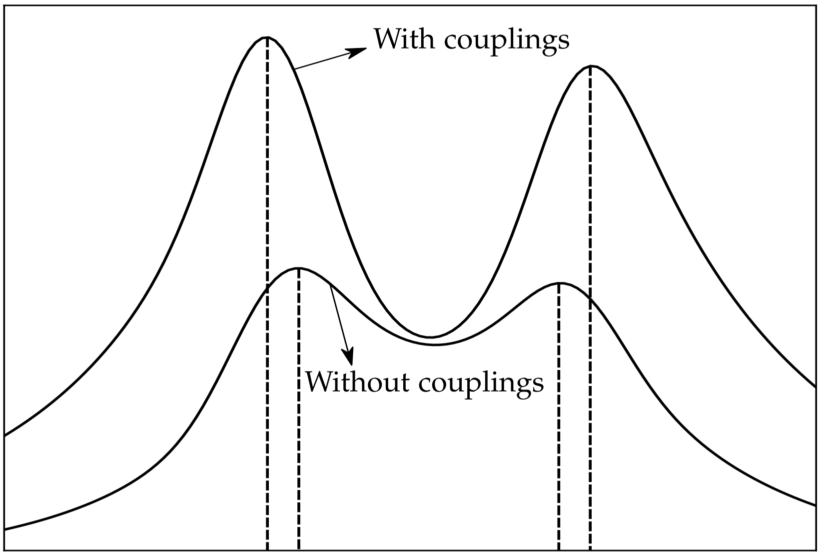

Figure 13: Two ionization spectra scanned around the doubled levels in the intermediate state. One obtained by neglecting the ionization-induced excited state couplings, the other with these couplings if effect. All the simulations parameter were the same. In this particular case, the ionization-induced couplings result in the peaks repelling each other. This is illustrated by the dashed lines drawn at the frequencies that result in maximal ionization. Note also the the change in lineshape due to the interferences in the overlap region.

3.2.2 *An* l*-fold Multiplet Coupled to one Continuum*

Going to l excited states modifies the set of equations (63) - (65) by adding equations similar to (63) and (64) for each of the excited states and by expanding equation (65) by adding extra terms:

$$i\dot{a}_1 = \omega_1 a_1 - \int d\varepsilon \, \langle 1 \,|V(t)|\, \varepsilon, \omega_\varepsilon \rangle \cos(\omega_a t + \Phi) a_\varepsilon, \tag{75}$$

$$\vdots \tag{76}$$

$$i\dot{a}_l = \omega_2 a_2 - \int d\varepsilon \, \langle 2 \,|V(t)|\, \varepsilon, \omega_\varepsilon \rangle \cos(\omega_a t + \Phi) a_\varepsilon, \tag{77}$$

$$i\dot{a}_\varepsilon = \omega_\varepsilon a_\varepsilon - \sum_{\alpha=1}^{l} \langle \varepsilon, \omega_\varepsilon \,|V(t)|\, \alpha \rangle \cos(\omega_a t + \Phi) a_\alpha \tag{78}$$

By making a change of variables and using the Markov approximation:

$$\begin{aligned} \dot{c}_1 = &- \frac{c_1}{4} \int_0^\infty d\omega_\varepsilon \, |\langle 1 \,|V(t)|\, \varepsilon, \omega_\varepsilon \rangle|^2 \, \rho(\omega_\varepsilon) \, [i\mathcal{P}(1/\Delta_{\varepsilon 1}) + \pi\delta(\Delta_{\varepsilon 1})] \\ &- \sum_{\alpha=2}^{l} \left\{ \frac{c_\alpha}{4} \int_0^\infty d\omega_\varepsilon \, \langle 1 \,|V(t)|\, \varepsilon, \omega_\varepsilon \rangle \langle \varepsilon, \omega_\varepsilon \,|V(t)|\, \alpha \rangle \, \rho(\omega_\varepsilon) \right. \\ &\left. \times \exp\left[i(\Delta_{\varepsilon 1} - \Delta_{\varepsilon\alpha})t\right] \cdot [i\mathcal{P}(2/(\Delta_{\varepsilon 1} + \Delta_{\varepsilon\alpha})) + \pi\delta(\Delta_{\varepsilon 1} + \Delta_{\varepsilon\alpha})] \right\} \end{aligned} \tag{79}$$

$$\vdots$$

$$\begin{aligned} \dot{c}_l = &- \frac{c_1}{4} \int_0^\infty d\omega_\varepsilon \, |\langle l \,|V(t)|\, \varepsilon, \omega_\varepsilon \rangle|^2 \, \rho(\omega_\varepsilon) \, [i\mathcal{P}(1/\Delta_{\varepsilon l}) + \pi\delta(\Delta_{\varepsilon 1})] \\ &- \sum_{\alpha=1}^{l-1} \left\{ \frac{c_\alpha}{4} \int_0^\infty d\omega_\varepsilon \, \langle l \,|V(t)|\, \varepsilon, \omega_\varepsilon \rangle \langle \varepsilon, \omega_\varepsilon \,|V(t)|\, \alpha \rangle \, \rho(\omega_\varepsilon) \right. \\ &\left. \times \exp\left[i(\Delta_{\varepsilon l} - \Delta_{\varepsilon\alpha})t\right] \cdot [i\mathcal{P}(2/(\Delta_{\varepsilon l} + \Delta_{\varepsilon\alpha})) + \pi\delta(\Delta_{\varepsilon l} + \Delta_{\varepsilon\alpha})] \right\} \end{aligned} \tag{80}$$

In these equations, the diagonal contribution is taken out of the summation so that the summation in the expression for $\dot{c}_i$ excludes $\alpha = i$. This makes the diagonal and off-diagonal terms clearer. Make the following definitions (analogous to (70), (71), (72)):

$$\Gamma_j(\omega_\varepsilon) = \frac{\pi}{2} |\langle j \,|V(t)|\, \varepsilon, \omega_\varepsilon \rangle|^2 \, \rho(\omega_\varepsilon) \tag{81}$$

$$\delta\omega_j = \frac{1}{2\pi} \mathcal{P} \int_0^\infty d\omega_\varepsilon \frac{\Gamma_j(\omega_\varepsilon)}{\Delta_{\varepsilon j}} \tag{82}$$

and

$$\Gamma_{ij}(\omega_\varepsilon) = \frac{\pi}{2}\left\langle i\left|V(t)\right|\varepsilon,\omega_\varepsilon\right\rangle\left\langle\varepsilon,\omega_\varepsilon\left|V(t)\right|j\right\rangle\rho(\omega_\varepsilon) \tag{83}$$

$$\delta\omega_{ij} = \frac{1}{2\pi}\mathcal{P}\int_0^\infty d\omega_\varepsilon\,\frac{2\Gamma_{ij}(\omega_\varepsilon)}{\Delta_{\varepsilon 1}+\Delta_{ij}} \tag{84}$$

$$q_{ij} = \frac{\delta\omega_{ij}(t)}{\Gamma_{ij}(t)}. \tag{85}$$

For a system of l states coupled to the continuum, the Hamiltonian H_{ion} in the basis of bare states is given by:

$$\begin{pmatrix}
\omega_1+\delta\omega_{11}-\frac{i}{2}\Gamma_{11} & -\frac{1}{2}\Gamma_{12}(q_{12}+i) & -\frac{1}{2}\Gamma_{13}(q_{13}+i) & \cdots & -\frac{1}{2}\Gamma_{1l}(q_{1l}+i)\\
-\frac{1}{2}\Gamma_{21}(q_{21}+i) & \omega_2+\delta\omega_{22}-\frac{i}{2}\Gamma_{22} & -\frac{1}{2}\Gamma_{22}(q_{22}+i) & \cdots & -\frac{1}{2}\Gamma_{2l}(q_{2l}+i)\\
-\frac{1}{2}\Gamma_{31}(q_{31}+i) & -\frac{1}{2}\Gamma_{32}(q_{32}+i) & \omega_3+\delta\omega_{33}-\frac{i}{2}\Gamma_{33} & \cdots & -\frac{1}{2}\Gamma_{3l}(q_{3l}+i)\\
\vdots & \vdots & \vdots & \ddots & \vdots\\
-\frac{1}{2}\Gamma_{l1}(q_{l1}+i) & -\frac{1}{2}\Gamma_{l2}(q_{l2}+i) & -\frac{1}{2}\Gamma_{l3}(q_{l3}+i) & \cdots & \omega_l+\delta\omega_{ll}-\frac{i}{2}\Gamma_{ll}
\end{pmatrix} \tag{86}$$

3.3 COMBINING RESONANT EXCITATION AND NON-RESONANT IONIZATION FOR MULTI-LEVEL ATOMS

The total Hamiltonian that describes both resonant excitations and non-resonant ionizations is found by combining the results of sections 3.1 and 3.2 (the Stark shifts are absorbed into the definitions ω_{f_i} because of space constraints):

$$\left(\begin{array}{ccc||cccc}
\omega_{i_1} & \cdots & 0 & g_{i_1,f_1} & g_{i_1,f_2} & \cdots & g_{i_1,f_l}\\
\vdots & \ddots & \vdots & \vdots & \vdots & \ddots & \vdots\\
0 & \cdots & \omega_{i_k} & g_{i_k,f_1} & g_{i_k,f_2} & \cdots & g_{i_k,f_l}\\
\hline\hline
g_{i_1,f_1} & \cdots & g_{i_k,f_1} & \omega_{f_1}-\omega_a-\frac{i}{2}\Gamma_{f1} & -\frac{1}{2}\Gamma_{f_1f_2}(q_{f_1f_2}+i) & \cdots & -\frac{1}{2}\Gamma_{f_1f_l}(q_{f_1f_l}+i)\\
g_{i_1,f_2} & \cdots & g_{i_k,f_2} & -\frac{1}{2}\Gamma_{f_2f_1}(q_{f_2f_1}+i) & \omega_{f_2}-\omega_a-\frac{i}{2}\Gamma_{f_2} & \cdots & -\frac{1}{2}\Gamma_{f_2f_l}(q_{f_2f_l}+i)\\
\vdots & \ddots & \vdots & \vdots & \vdots & \ddots & \vdots\\
g_{i_1,f_l} & \cdots & g_{i_k,f_l} & -\frac{1}{2}\Gamma_{f_lf_1}(q_{f_lf_1}+i) & -\frac{1}{2}\Gamma_{f_lf_2}(q_{f_lf_2}+i) & \cdots & \omega_{f_l}-\omega_a-\frac{i}{2}\Gamma_{f_l}
\end{array}\right). \tag{87}$$

Part II

APPLICATION TO EXPERIMENT

4

EXPERIMENTAL CONSIDERATIONS

The theory of hyperfine interactions discussed in chapter 1 determines the system the nuclear spectroscopist tries to probe. A nucleus with spin I and electronic spins J_1 and J_2 has a total of $\min\{2I+1, 2J_1+1\}$ states in the ground state multiplet and $\min\{2I+1, 2J_2+1\}$ in the excited state multiplet. The theory introduced in chapters 2 and 3 leads to a system of coupled differential equations, one for each of the hyperfine states, that can only be solved with numerical methods for all but the simpletst two-level case. The theory developed in chapters 2 and 3 does not take into account the full experimental conditions, however. This section explains how the simulations will bridge the gap between the exact theory and the experimental circumstances.

4.1 INPUT PARAMETERS

The implementation of the simulation procedure was written in Python v2.6. This package relies on fast numerical algortihms implemented by the NumPy and SciPy packages [39]. A Graphical User Interface (GUI) was also written using the Tkinter library. This GUI allows full control over all of the physical parameters, starting from input .txt files like those shown in appendix B. It allows the user to easily compare the populations of the hyperfine states or the ionization spectrum for different parameters.

The units are always mentioned in the parameter description. Whenever two numbers appear below a single name, those two quantities are stored as lists. For instance, the A parameters are stored as $[A_{\text{lower}}, A_{\text{upper}}]$.

The photo-ionisation cross section is used to calculate the ionization parameters Γ_i, since it is the product of this cross section with the laser power of the second laser. An approximation that is always made is to assign the same ionization rate Γ to all states belonging to the same hyperfine multiplet. This also means that the off-diagonal Γ_{ij} are equal to the same Γ. So, even though it is in principle possible to calculate all of the Γ's from first principles using (81) and (83), the experimentally tabulated cross sections will be used.

The laser intensity is entered into the code in the dimensions of energy per pulse, and is divided by the area of the laser beam to provide the intensity per unit area. This quantity is then used throughout the calculations. The duration of the laser pulses also plays an important role, since they determine the laser power densities $\mathcal{P}_i$ of both lasers. The pulses are assumed to be Gaussian-shaped in time, but this can be changed. The temporal separation of the two lasers can also be changed. The oscllator strength is used in the calculation of the resonant interaction parameters g, as explained by equation (14).

It is also possible to simulate the effects of cw-excitations by entering the total energy the atoms or ions are subjected to when travelling through the laser beam and by choosing a flat pulse shape (for example, if the atoms travel through the beam in $3\mu s$, multiply the power of the laser by $3\mu s$ and put that number in the .txt file).

With this, all of the parameters appearing in the Hamiltonian of the system (87) have been linked to the input parameters, except for the Fano parameters q and the Stark shifts $\delta\omega_i$. The effect of the Stark shifts $\delta\omega_i$ is understood easily as a shift of the energy levels. The influence of the Fano q parameter is less clear and will be investigated later. The algorithm that will be used from now on will be further developed to better reflect the actual experimental conditions. Two experimental effects will be included:

1. **Spatial laser profile.** The laser intensity is usually not constant throughout the cross section of the laser beam. The ensemble of atoms is not subjected to just one laser power $\mathcal{P}_1$, but rather a distribution centered around this value at any instantaneous moment in time t. Also, the laser field fluctuates shot-by-shot. Therefore not every atom experiences the same electrical laser field. The total ionization signal will therefore be a sum of Rabi oscillated signals with many different periods, since it is a result of many atom-laser interactions. These laser fluctuations are all taken into account by averaging the simulated spectra over a range of powers.

2. **Temporal laser pulse shape.** CRIS uses pulsed lasers, and therefore the power output of the laser depends on time. Typically, the laser pulse shape is roughly Gaussian with a full width half maximum of the order of 10 nanoseconds. The pulse shape can have important consequences on the response of the system (see chapter 6). The Hamiltonian will be time-dependent, which will impact the simulation procedure as is outlined below (section 4.2).

These two effects will completely remove the Rabi Oscillations from the simulated state populations and ionization spectra, facilitating analysis and interpretation of more complicated multi-level simulations. This will not remove the coherent effects but will rather average the coherent effects over a certain range.

A remark on the laser linewidth should be made at this point. Lasers emit a spectrum of wavelengths, not just a single one. So far, the response of an atomic system subjected to a single cavity mode has been treated. Going towards realistic lasers with a non-delta function linewidth would in principle mean that for every detuning, the response of the system to the whole emission spectrum of the laser would have to be calculated. This is of course very resource intensive, so a faster option is to just calculate the response to a single laser wavelength and to then take a convolution of the ionization spectra and population profiles. If the laser linewidth is broader than the resonances, they will of course be broadened.

This approach is only approximately valid. Consider for example the case of a fully saturated transition and a laser linewidth twice as large as the natural linewidht. Convoluting the simulated spectra with this broader lineshape will result in a reduction of the ionization efficiency by a factor of two, since the lineshape becomes broader while keeping its integral constant. Experimentally, however, the ionization efficiency will not be reduced very much, since the transition is heavily saturated. Even though only about half of the power in the laser beam is actually used to excite electrons, this reduced power is still sufficient to saturate. In other words: convoluting spectra results in lineshapes with the correct width, but the total ionization efficiencies or saturation curves are unreliable.

For the reasons mentioned in the above two paragraphs, the effect of the laser linewidth is not taken into account for the simulations in this work; all excitations are assumed to be narrowband.

4.2 ALGORITHM

The algorithm can be broken down into three separate blocks.

1. The **input and initialization** phase. In this step, the parameters are read in from either an input file or from the GUI. With these parameters, Python objects are made for the hyperfine states and the Hamiltonian. Each hyperfine state has a certain total angular momentum F, so there are $2F+1$ possible F projections to take into account. The linear polarization of the laser light imposes a selection rule $\Delta m = 0$ which implies that small Hamiltonians can be constructed for each possible angular momentum projection. The total Hamiltonian H is then constructed as a concatenation of these smaller matrices.

2. The **calculation** phase. The central piece of code is solving the Von Neumann equation for non-Hermitian Hamiltoni-

ans, which is the density matrix version of Schrödingers equation:

$$i\frac{d\rho}{dt} = H\rho - \rho H^{\dagger} \tag{88}$$

The reason for using a density matrix is that it makes it easier to add effects like spontaneous decay later on, since spontaneous decay is typically formalized using density matrices. The solutions can be found by matrix exponentiating (for time-independent Hamiltonians);

$$\rho(t) = \exp(-iHt)\rho(0)\exp(-iH^{\dagger}t). \tag{89}$$

The Hamiltonian can be time-dependent if the lasers are pulsed. The approach is then to discretize this smooth excitation pulse into a step-like function and to solve

$$\begin{aligned} \rho(t) &= \exp\left(-i\int_{t_0}^{t_1} H dt'\right)\rho(0)\exp\left(-i\int_{t_0}^{t_1} H^{\dagger} dt'\right) \\ &\approx \exp\left(-i\sum_k H_k \Delta t\right)\rho(0)\exp\left(-i\sum_k H_k^{\dagger}\Delta t\right) \\ &= \prod_k\left[\exp\left(-iH_k\Delta t\right)\right]\rho(0)\prod_k\left[\exp\left(-iH_k^{\dagger}\Delta t\right)\right]. \end{aligned} \tag{90}$$

The matrix exponentiations are done numerically by using a Numpy algorithm based on Pade approximants. This approach is very stable [40]. All results presented so far were obtained by calculating the density matrix at time t for laser frequencies in a user-defined range using relation (89) or (90).

Taking into account the two effects described above (the temporal laser pulse shape and the spatial laser profile) requires looping over the calculations twice; one for each effect. The user can define how many iterations are needed in each of these loops.

3. The **Wrapping-up phase**. The state objects are assigned their populations for each frequency and time. The total ionization rate is calculated. If needed, the laser linewidth is taken into account by a convolution of the spectra. If asked, the results are stored in .txt files and figures are saved. The population of all of the state objects can be plotted and manipulated using standard python plotting tools, or by using the GUI plotting tool.

Expressed in pseudo-code, the algorithm is as follows:

Listing 1: Pseudo-code algoritm followed by the simulation code.

```
#--------------------------#
# Input and initialization #
#--------------------------#
Read Parameters

Make Objects
#--------------------------#
#  Calculation             #
#--------------------------#
for position in space:
{
        for time in timerange:
        {
                for frequency in scanning range:
                {
                        Use laser power(position, time)
                        Solve using Von Neumann
                }
        }
}
Average over space
#--------------------------#
# Wrapping up              #
#--------------------------#
Calculate populations and ionization rate (time, space)
Concolute if required
Save files, make figures, plotting,...
```

This is the algorithm that will be used for all of the simulations in the next chapters. First, the effect the two outer loops in Algorithm 1 have on the simulated lineshapes and their time dependence will be investigated.

4.2.1 *Influence of the Spatial Laser Profile*

As outlined earlier in this chapter laser power fluctuations and the spatial non-uniformity of the laser power require averaging the simulations over several different laser powers. The assumption is that the power can be up to 50 percent lower near the edge of the atom beam than near the center. The period of a Rabi Oscillation for a two level atom was presented in equation (33):

$$P_{0,n} = \sin^2(2\theta)\,[1-\cos(\Omega t)]\,, \qquad (33)$$

$$\text{where } \Omega = \lambda_+ - \lambda_- = \sqrt{4g^2(t)+\Delta_{01}^2}.$$

The factor $1-\cos(\Omega t)$ is averaged to one in experiments due to coherence losses. These coherence losses are simulated in algorithm 1 by applying a laser power distribution rather than a single laser power. This will dampen the oscillations in time, as can be verified by looking at the population of the excited state when the system is subjected to a cw laser beam with a certain laser power distribution (without the second laser present).

Analytical calculations can be made to predict the evolution of the ensemble under these circumstances. On resonance $\Delta_{01} = 0$, equation (33) simplifies to

$$P_{0,n}(g,t) = \frac{1}{2}\left[1 - \cos(gt)\right]. \tag{91}$$

Suppose this population has to be averaged over laser fluctuations uniformly distributed in $\left[\frac{1}{2}\mathcal{P}_{\text{av}}, \frac{3}{2}\mathcal{P}_{\text{av}}\right]$ so that g is uniformly distributed in $\left[\sqrt{\frac{1}{2}}g_{\text{av}}, \sqrt{\frac{3}{2}}g_{\text{av}}\right]$. The average population is then given by

$$\begin{aligned} P^{\text{av}}_{0,n}(t) &= \frac{1}{2\left(\sqrt{3/2}-\sqrt{1/2}\right)g_{\text{av}}}\int_{\sqrt{1/2}g_{\text{av}}}^{\sqrt{3/2}g_{\text{av}}} dg\left[1-\cos(gt)\right] \\ &= \frac{1}{2}\left[-\frac{\sin\left(\sqrt{3/2}g_{\text{av}}t\right)-\sin\left(\sqrt{1/2}g_{\text{av}}t\right)}{2\left(\sqrt{3/2}-\sqrt{1/2}\right)g_{\text{av}}t}\right]. \end{aligned} \tag{92}$$

This result illustrates that the oscillations are damped with time as $\frac{1}{g_{\text{av}}t}$. Numerical simulations are plotted in figure 14 for $g_{\text{av}} = 1$ (dashed line) and $g_{\text{av}} = 20$ (full line). The averaging procedure will be more effective for high powers than for low powers.

This dampening in time will be important in chapter 6 (though not strictly necessary), where the effect of separating the excitation pulse from the ionization pulse is investigated. The results of the simulations would depend very strongly on when the excitation pulse ends if the Rabi oscillations are not removed from the simulations. This does not make the analysis impossible, but it does make interpretation more involved.

The smoothening of the Rabi oscillations in time is also reflected in the frequency spectrum of the populations: the oscillations visible in figure 4 are dampened slightly (see figure 15). Implementing a smooth pulse shape will actually remove these frequency oscillations completely, which will be shown in section 4.2.2.

4.2.2 *Influence of the Temporal Laser Pulse Shape*

Switching from cw lasers to pulsed lasers requires a time dependent Hamiltonian. Both lasers can be pulsed, and the delay between the pulses can be changed. It is assumed that the laser pulses have a Guassian shape, but different pulse shapes are

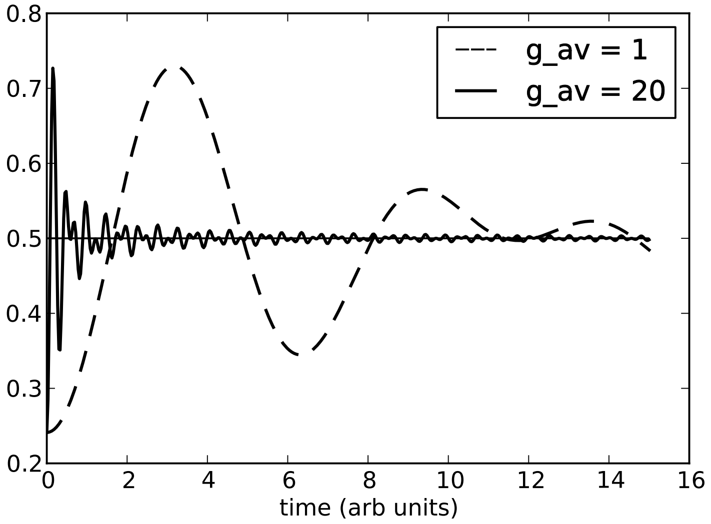

Figure 14: Expression ([92]) illustrated for $g_{av} = 1$ (dashed line) and $g_{av} = 20$ (full line). Note the $\frac{1}{g_{av} t}$ dampening; the population evolves to 50 percent in all cases.

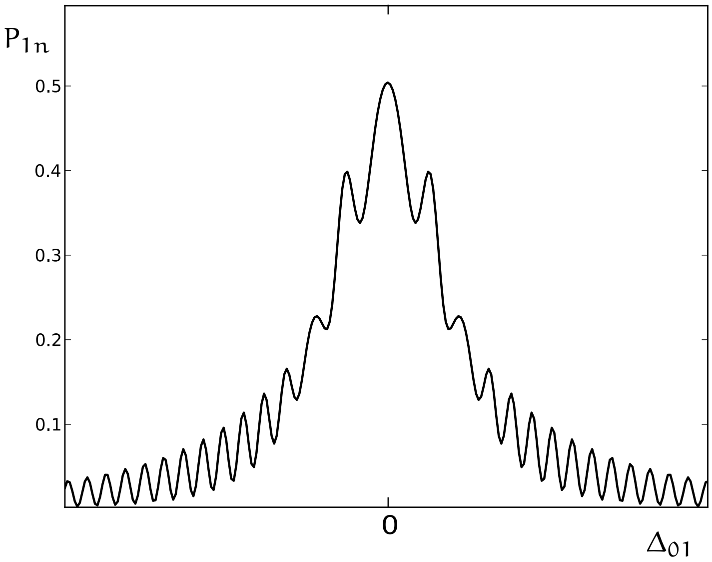

Figure 15: Population of the excited state as function of detuning, with averaging over the spatial laser profile taken into account.

also possible. When the spatial and temporal pulse shape are taken into account (so algorithm 1 is completely followed), results like figure 16 are obtained. This figure shows the population of the excited state as a function of detuning half-way through the excitation pulse, in absence of ionization. The oscillations have been removed (compare to figure 4 or 15). For completeness, a plot of the population on resonance as function of time is shown on the right, with an arrow that indicates the time at which the spectrum on the left is produced. Note the similarities

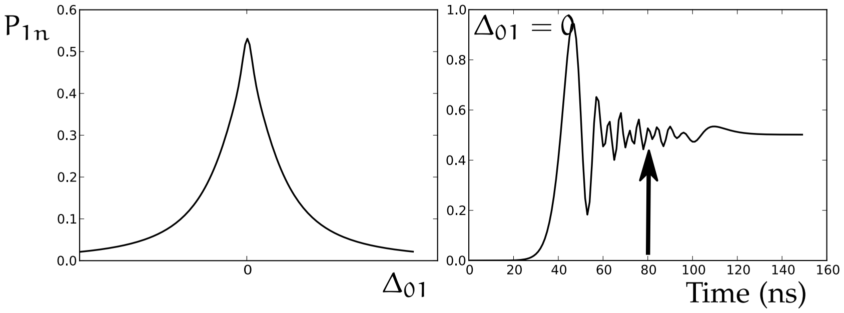

Figure 16: The excited state population on resonance as function of time (right) and the population of the excited state as function of detuning (left). The time indicated with the large arrow on the right plot is the time at which the left plot is made.

with figure 14.

The implementation of the temporal pulse shape and the addition of a spatial averaging mechanism allows for a realistic simulation of experimental ionization spectra. The next chapters will explore the possibilities provided by the procedure outlined in this chapter.

5

SYSTEMATIC EFFECTS ON LINESHAPES FOR SIMULTANEOUS EXCITATION AND IONIZATION

This chapter will investigate the systematic effects predicted by the theory developed in chapters 2 and 3 and the algorithm for the simulations presented in chapter 4. It has been highlighted that the couplings of the discrete electronic states can lead to systematic deviations in peak-to peak distances of ionization spectra. The additional couplings induced by the ionizing laser can also adjust lineshapes. This chapter sets out to study these effects in some detail, both qualitatively and quantitatively. The latter will be done by simulating ionization spectra and then fitting them using the standard fitting lineshapes used in hyperfine laser spectroscopy.

This standard fitting procedure consists of summing several pseudo-Voigt profiles at positions calculated with equation 5 and by performing a least-squares optimization, with free parameters A, B and the intensities of the peaks. The pseudo-Voigt profile f_{pV}

$$f_{pV}(x) = (1-\eta) f_{\mathrm{Gauss}}(x, \gamma_G) + \eta f_{\mathrm{Lorentz}}(x, \gamma_L), \tag{93}$$

is an approximation to a Voigt profile, which in turn is the convolution of a Lorentzian of width γ_L and a Gaussian profile of width γ_G. Note that η, γ_G, γ_L are also free parameters. The parameter η expresses how strong the Lorentzian component is relative to the Gaussian component. The reason why pseudo-Voigt profiles are used rather than Voigt profiles is that they require significantly less computing time and yet are sufficiently precise [41]. The use of both Lorentzian and Gaussian components reflects two different mechanisms that lead to broadening of resonance profiles; these are homogeneous broadening and inhomogeneous broadening.

If the cause of the broadening is the same for every atom, it is homogeneous, and the resulting profile will be Lorentzian. Examples are power broadening or collisional (pressure) broadening: all atoms experience the same laser powers or pressure. If on the other hand the broadening is the result of a process that varies in size from atom to atom, the profile will be Gaussian. The most common example here is Doppler broadening; every atom has a slightly different velocity. The effect of multiple broadening mechanisms can be taken into account by convoluting their respective profiles. Since the convolution of two Gaussians is once again Gaussian and the convolution of two Lorentzians is once again Lorentzian, all broadening mechanisms can be described by a Voigt profile.

The goal of this chapter consists of two intertwined sub goals:

1. What is the influence of the coherent (homogeneous) laser couplings on the lineshape? In other words, to what extent does the lineshape deviate from a pseudo-voigt?
2. How is the position of the resonances influenced by the coherent interactions? Is there a noticeable effect on the fitted hyperfine parameters?

This chapter will generate ionization spectra using the model introduced in previous chapters. These ionization spectra will then be fitted using the fitting model described above. The simulation strategy will focus on two cases, illustrated schematically in figure 17. Typical simulations values are shown in file B.2.

The two cases under investigation are a ground state doublet with one excited state and an excited doublet with only one ground state. Both laser powers will be varied to gauge their impact.

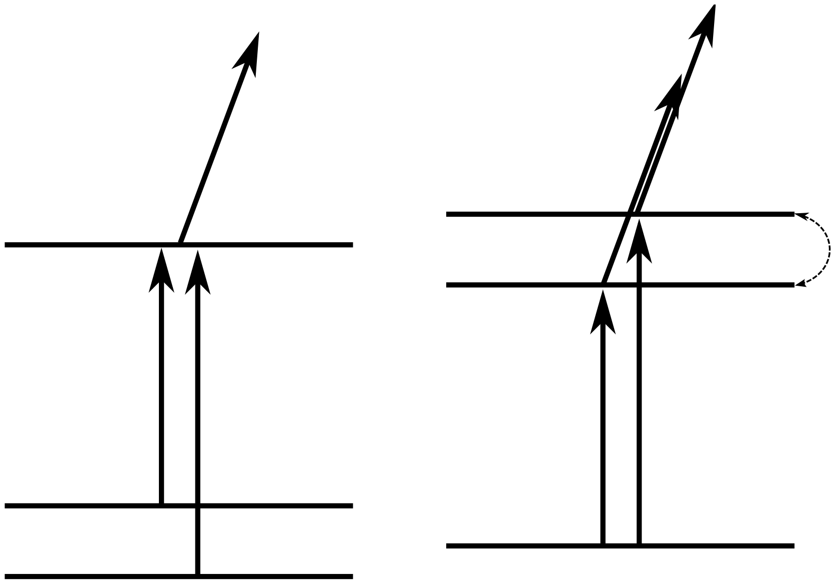

Figure 17: The two physics cases under investigation: a ground state doublet with an excited singlet and a singlet with an excited doublet that is coupled through the continuum.

After this, the influence of the fano q-terms is investigated by looking at a simple system consisting of one ground state and an excited doublet for several values of q.

Once these simple cases are understood, an example will be presented to make things more quantitative and concrete; section 5.2 will investigate the hyperfine structure of ^{57,59,63,65}Cu in some more detail. These isotopes are of particular interest because a recent in-gas cell laser ionization experiment [42, 43] obtained hyperfine A parameters that were slightly different from a high-resolution fluorescence laser spectroscopy experiment [44]. This mismatch could be due to the laser-induced couplings which are present in the laser ionization experiment. The hyperfine structure of the transition that was used consists of a ground state doublet and an excited state doublet. This makes it a generalization of the cases studied in the earlier parts of the chapter.

5.1 SIMULATION RESULTS

The results of the simulations for the two cases are shown in figure 18. This figure shows the relative deviation of the fitted hyperfine parameters with respect to the assumed value in the simulations. This is done for several different laser power combinations and input A parameters. The laser powers are never taken higher than saturation values, since this would generally also not be done in experiments. The inset shows a pictorial representation of the atomic system. The scale on the x axis is the fitted hyperfine splitting divided by the fitted FWHM, a measure for the resolution of the experiment. Note how the fit overestimates the upper splitting but underestimates the lower splittings. Note also the scale on the y axis; deviations of several tenths of percent are possible for very poorly resolved structures. A correlation between the relative deviation and the power in the excitation step appears to exist for the extracted values of A_{low}. However, the power of the ionization step still has a small influence. Similarly, the extracted A_{up} appears quite strongly correlated with the ionizing laser power but is also not completely independent of the power in the first laser step.

The results in this section provide clear examples that care is needed when interpreting RIS spectra. If the peaks of the spectrum start overlapping ($A_{\mathrm{fit}} < 3$ FWHM), the extracted hyperfine splittings can significantly shift from the true, bare-atom values. The laser power in both steps plays an important role. This makes correcting experimental spectra nontrivial. Section 6.1.3 will present a way of reducing the complexity of the problem by removing all effects due to the ionizing laser by adjusting the delay between the two laser pulses.

If both the ground state and the excited state are split into two or more states, the interpretation of the ionization spectra is further complicated, especially if the ratio of the hyperfine splittings is fixed in the fitting procedure (to a ratio determined by the study of stable atomic beams). The increase in the fitted excited multiplet splitting and the decrease in the fitted ground

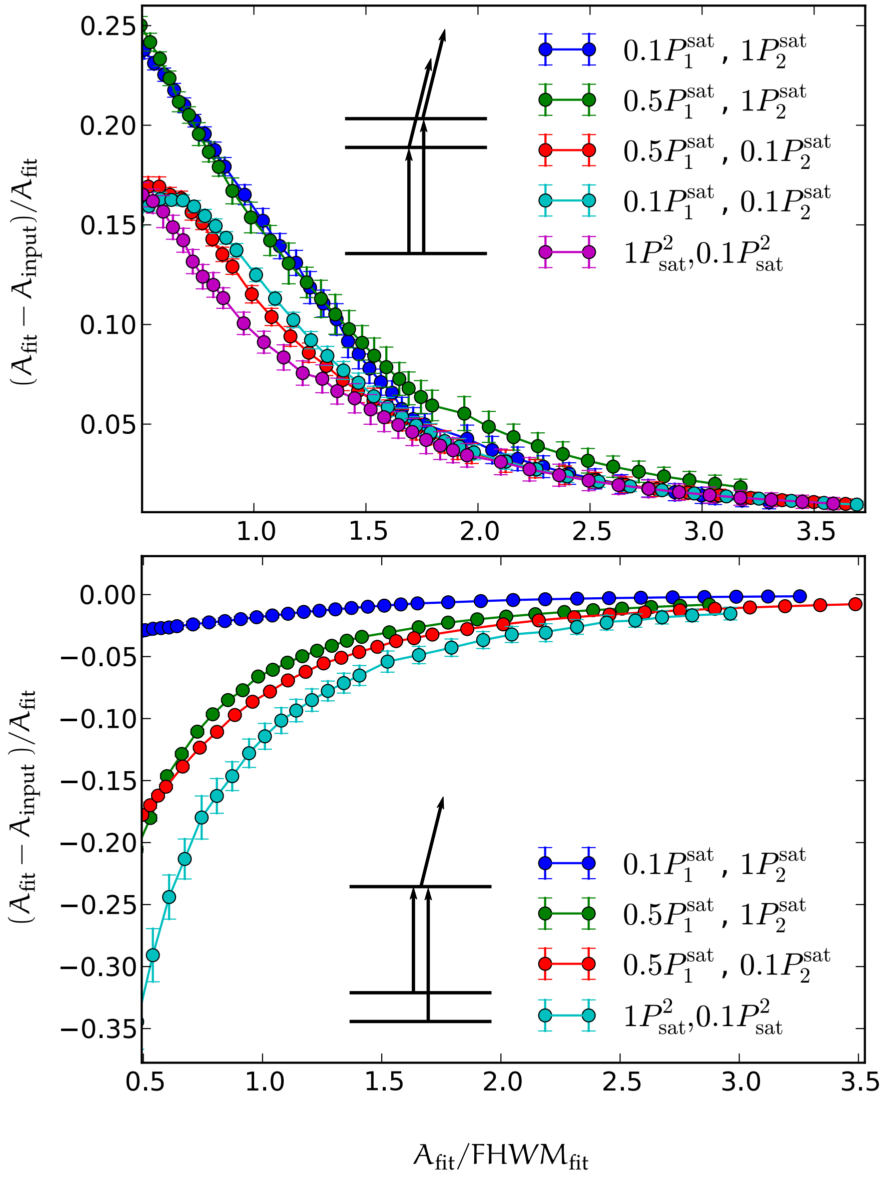

Figure 18: Relative deviation on extracted hyperfine parameters for several different laser power combinations and input A parameters. The scale on the x axis is the fitted hyperfine splitting divided by the fitted FWHM, which is a measure for the resolution of the experiment. Note how the fit overestimates the upper splitting but underestimates the lower splittings. Note also the scale on the y axis; deviations of several tenths of percent are possible for very poorly resolved structures.

state splitting then have to compete with each other, making the accuracy of the final fitted values uncertain. To illustrate this point, an example with experimental data will be discussed in section 5.2.

5.1.1 *Part III: Influence of the Fano q Parameter*

The effect of the Fano q parameter introduced by equation (72) on the lineshapes is illustrated by figures 19. This figure shows examples of spectra at different values q. These figures were made at a quite high ionizing laser power of 25 mJ. The dashed lines on the left plot of figure 19 indicate the center of gravity of the two resonances. As the Fano parameter increases, this center shifts to lower wavelengths. This figure also shows that the peak-to-peak distance increases significantly. The right plot of figure 19 illustrates what happens for very large Fano factors: the two peaks become asymmetrically broadened and the center of gravity shifts quite dramatically. This asymmetrical power broadening is a result of the interferences between the different ionization channels to the dressed states that are embedded into the continuum by the the ionizing laser. To our knowledge, such asymmetric lineshapes have not been detected in resonance ionization laser spectroscopy experiments. For lower Fano factors, the main effect is the shifting of the center of gravity and the peak-to-peak distances. Recall also that typical values of q are less then 10.

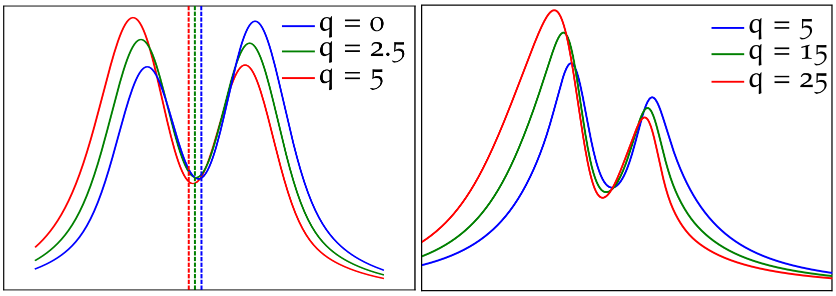

Figure 19: Five ionization curves, with Fano factors of respectively 0,2.5,5,15 and 25. For the three spectra shown on the left, the dashed lines indicate the center of gravity of the two resonances.

5.2 APPLICATION: IN-GAS-CELL LASER SPECTROSCOPY OF THE NEUTRON-DEFICIENT CU ISOTOPES

In two recent papers Cocolios et al. presented in-gas-cell laser spectroscopy measurements of neutron deficient Cu isotopes [42, 43]. This data was gathered using a two-step laser ionization scheme, but in different conditions than CRIS. Due to the production methods of the radioactive isotopes, the atoms have a large velocity spread and pass through a region of very high pressure. The high pressure results in a reduction of the lifetime of the excited states due to collisional de-excitations. The velocity spread and the collisions result in Doppler broadening and pressure broadening respectively. While Doppler broadening can be taken into account by simply convoluting the simulated lineshapes with Gaussian profiles of the appropriate width, pressure broadening is not trivially implemented within the context of the model.

For some isotopes the A parameters extracted in [42] and [43] deviate from the values obtained using high-resolution fluorescence laser spectroscopy [44]. The fitting approach of the in-gas cell experiments was to fix the ratio of A_{up} and A_{low} and to fit the ionization spectra with a set of Voigt profiles. This subsection investigates whether or not the discrepancy between the high-resolution fluorescence data and the in gas-cell data is due to the fact that this fitting model does not take into account the effects that were discussed earlier in this chapter.

In ^{59}Cu the fitted A parameters are about 1 percent larger than in [44]. For ^{58}Cu, the extracted A parameters are 16 percent smaller than in[44]. Figures 20 and 21 show the experimental spectra taken from [42] and [43]. Table 1 summarizes the essential values.

	Gas cell	Collinear	
Isotope	A_{up}[42]	A_{up}[44]	A_{up}[42]/A_{up}[44]
58	1891(52)	2257(9)	0.84(2)
59	5033(10)	4989.6(24)	1.009(2)

Table 1: Summary of literature values of the hyperfine A parameter.

The influence of the laser-related homogeneous broadening on the extracted A parameters can be investigated by performing simulations at the laser powers and laser specifications used by Cocolios et al (explained in detail in [45]). Since pressure broadening is not included in the model the resulting lines will be much narrower than the experimental data. Note that the laser linewidth is 1.6 GHz, while the natural linewdith of the resonances is 1 MHz [46]. Therefore, neglecting pressure broadening, only a fraction (6.25×10^{-4}) of the total laser power can actually be used for the excitations. Simulations should be convoluted with a 1.6 GHz FWHM Gaussian to take the Doppler broadening into account. Making the simulations with the actual splitting of the hyperfine levels and the experimental laser powers will result in resonances with an energy separation many times their width. As figure 18 suggested, no shifts in the peak-to-peak positions will therefore be observed. Some information can nevertheless be obtained from the simulations by downscaling the A parameter so that the simulations match the experimental spectra. This reflects the idea that it is the energy difference relative to the resonance width that is the important variable: a system with resonances that are a few GHz wide and have an splitting parameter of several GHz due to pressure broadening could be considered approximately equivalent to a system with resonances that are a few MHz wide with a splitting that is reduced accordingly.

File B.3 shows the simulation settings. The simulations are convoluted with a 1.6GHz FWHM Gaussian to take the Doppler broadening into account. The fitting approach is as follows: a Voigt profile is used for each component of the hyperfine spectrum. The upper hyperfine A parameter is constrained as follows (based on measurements in an atomic beam unit):

$$A_{\text{upper}} = 0.414 \times A_{\text{lower}}. \tag{94}$$

This is also the approach taken by Cocolios et al. This fitting routine does not take into account the laser-related couplings that have been discussed earlier in this section into account. This could lead to an incorrect extraction of the hyperfine parameters. Figures 20 and 21 show the results of the simulations and the corresponding fits. Note the close agreement of the relative peak intensities. A summary of the results is shown in table 2.

Isotope	A_{up}[42]/A_{up}[44]	A_{up}/A_{input}
58	0.84(2)	1.04(1)
59	1.009(2)	1.008(3)

Table 2: Summary of literature and simulated ratios of the hyperfine A parameter. The experimental data is divided by the result obtained with the collinear laser spectroscopy measurement by Vingerhoets et al [44] while the simulated values are normalized to the input A parameter.

The table illustrates how for ^{59}Cu, the couplings induced by the ionizing laser result in an increase in the fitted A-parameter, which could explain the discrepancy between the gas cell data and the collinear data. The order-of-magnitude of the effect is reproduced by the simulations. The reduced A-parameter obtained in [42] for ^{58}Cu is not reproduced in the simulations. However, fitting four hyperfine peaks underneath such an unresolved structure is nontrivial; the positions and width of the peaks are very strongly correlated, which could have been undervalued by previous analysis. For example, a reduction of the intensity of the rightmost peak is easily compensated for by moving the third peak further to the right.

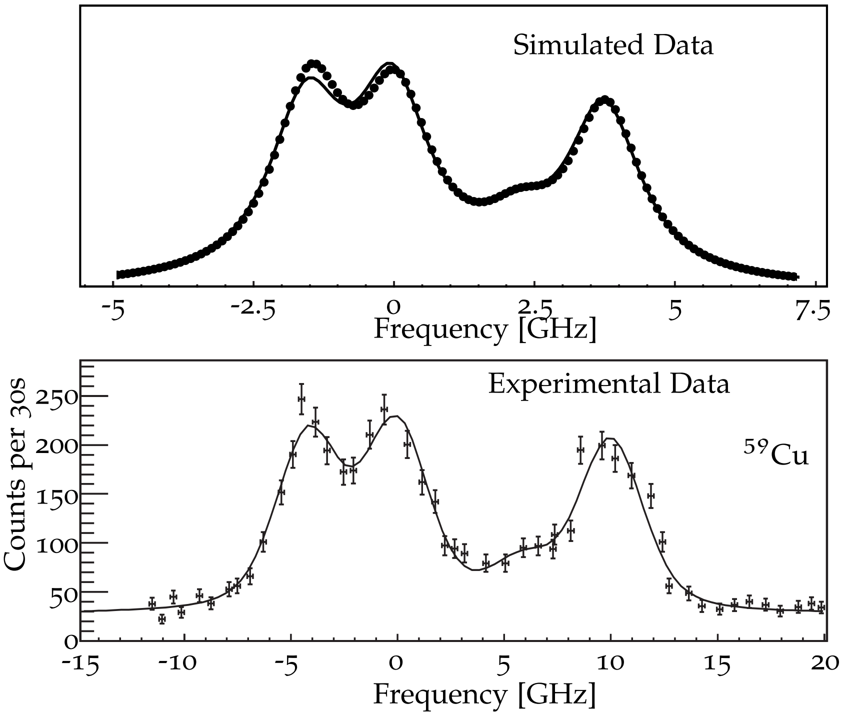

Figure 20: Simulations and experimental data for ^{59}Cu. Top: Simulation (dots) and the fit (line). Bottom: Experimental data from [42].

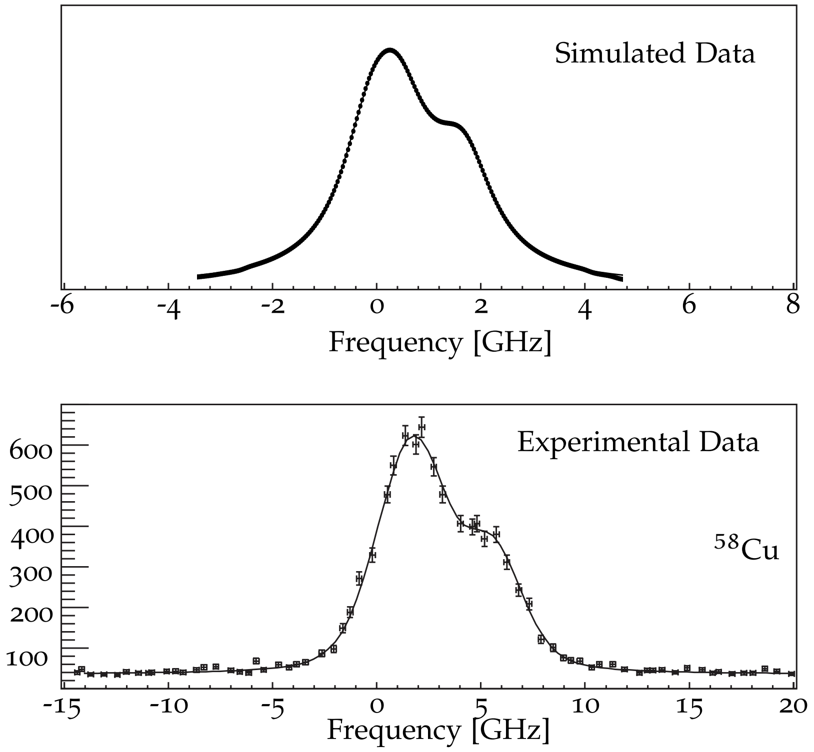

Figure 21: Simulations and experimental data for ^{58}Cu. Top: Simulation (dots) and fit (line). Bottom: Experimental data from [42].

6

SYSTEMATIC EFFECTS ON LINESHAPES FOR TIME-SEPARATED LASER PULSES

The combination of the inherent timing structure of a pulsed laser with laser ionization and subsequent ion detection provides the experimentalist with an interesting freedom: the possibility to choose when to probe the population of the excited state. The exploration of this additional degree of freedom and the implications it has for spectroscopy have only recently been investigated theoretically and experimentally (see e.g. [17, 47, 48]).

The previous chapters have always dealt with the case of simultaneous excitations and ionizations. The ionizing laser perturbs the energy levels and since the excitations take place while these perturbations are present, they can be seen in the ionization spectra. If on the other hand the second laser is only firing after the first laser has stopped, the energy levels will only be perturbed after the excitations have probed them. This means that the ionization spectra will not show any of the ionization-related lineshape distortions. This will be investigated in section 6.1.3.

Another issue that could be addressed by exploiting the timing properties of the two laser fields is the issue of power broadening (explained in section 2.4 earlier in this document) . Power broadening due to the second laser is avoided completely if the second laser pulse arrives after the excitation laser pulse, for the same reasons explained in the previous paragraph. The states do get broadened by the second laser, but they only broaden after they have been probed; the broadening will therefore not be recorded. But there is more; power broadening due to the first laser can also be reduced significantly (and in some cases avoided entirely).

6.1 SEPARATED LASER PULSES AND PRECISION

Applying pulsed laser excitations to an atomic system adds an explicit time dependence to the Hamiltonian. The effect this has on the evolution of the population of this system is the subject of the next section. After the influence of pulsed lasers is understood, an ionization pulse will be added to the description. Sections 6.1.2 and 6.1.3 will then discuss how the relative timing of the excitation and ionization pulse can be used to improve respectively the precision and accuracy of RIS.

6.1.1 *Pulsed Laser Excitation*

Consider a simple two-level system subjected to only a pulsed resonant excitation laser. The evolution of such a system is described by the following Hamiltonian (in the adiabatic basis):

$$i\dot{A}(t) = \begin{pmatrix} \lambda_- & -i\dot{\theta} \\ i\dot{\theta} & \lambda_+ \end{pmatrix} A(t). \tag{32}$$

The name 'adiabatic states' can now be explained, using the adiabatic theorem (originally formulated by Born and Fock [49]) states (translated from German):

> "A physical system remains in its instantaneous eigenstate if a given perturbation is acting on it slowly enough compared to the gap between the eigenvalue and the rest of the Hamiltonian's spectrum".

The gap in the energy spectrum determines a unit of time by dividing the energy gap by $\hbar$, and therefore allows for a definition of what 'slow' actually means (although there is theoretical work devoted to defining an adiabatic theorem for systems without such a gap, allowing study of system with crossing levels rather than mixing levels [50]). For dynamics (32) the adiabatic theorem states that the excitation process is adiabatic if [17]:

$$\left|\dot{\theta}(t)\right| \ll \lambda_+ - \lambda_- \tag{95}$$

Because the perturbation slowly varies in time, the system has time to adapt its configuration. The state vector of the system can keep up with the vector $|-, n\rangle$ as it evolves through time (see figure 22 for a schematic idea of how the vector $|-, n\rangle$ evolves when subjected to a gaussian pulse). If this condition is not met, the process is diabatic and the state vector of the system will have trouble adjusting its configuration. The state vector will lag behind. This means that the population can stay in the adiabatic state throughout the excitation pulse. Note that at the beginning and the end of the excitation pulse $\theta = 0$; the adiabatic and bare states are uniquely identified with one another.

Suppose the population is initially in $|0, n\rangle = |-, n\rangle$. If the evolution of the system is adiabatic, it has time to adapt in such a way that the population stays in the adiabatic state $|-, n\rangle$. At the end of the excitation pulse, the population is still in $|-, n\rangle$. Since $|-, n\rangle$ is the same as $|0, n\rangle$, no net population remains in the excited state $|1, n-1\rangle$. Note that the electrons do make a brief excursion from the state $|0, n\rangle$ to $|1, n-1\rangle$, but they end up in $|0, n\rangle$ eventually. This process is referred to as adiabatic population return. On the other hand, if the evolution is non-adiabatic, population initially in $|0, n\rangle = |-, n\rangle$ will evolve into

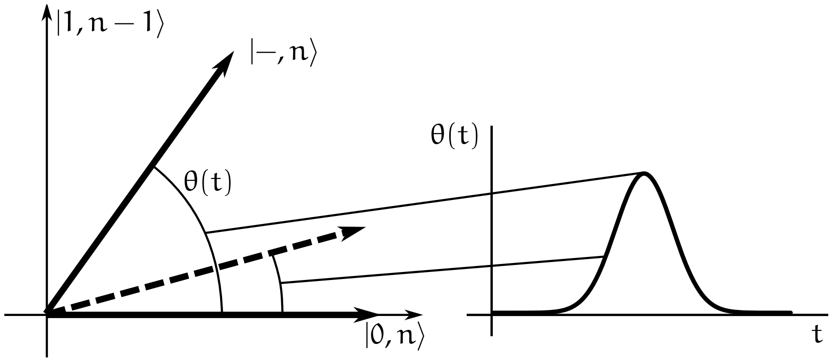

Figure 22: Left: Evolution of the state vector $|-, n\rangle$ when the system is subjected to a gaussian laser pulse. Right: the mixing angle $\theta(t)$. On resonance, the angle becomes $\frac{\pi}{2}$ when the power is maximal. If the evolution of the system is adiabatic, the state vector of the system follows that of the vector $|-, n\rangle$, and no net population remains in $|1, n-1\rangle$ after the pulse. If the evolution is non-adiabatic, the state vector of the system lags behind so that some population remains in $|1, n-1\rangle$.

a superposition of the two adiabatic states during the exciation pulse, which means that some of the population will have left the ground state $|0, n\rangle$ and will have transferred to $|1, n-1\rangle$ at the end of the evolution. The maximal transferred population is 50%.

Figure 23 A reveals both kinds of processes occur during coherent photon excitation. This figure shows the population of the excited state of a two-level system as a function of time and as a function of the detuning of the excitation laser. The laser pulse shape is Gaussian as a function of time and there is no ionization laser.

Note that there is a considerable adiabatic component to the excitations when the laser is tuned off-resonance: after an excursion to the state $|1, n\rangle$, there is adiabatic population return to $|0, n\rangle$. This is illustrated in figure 23 C for a detuning $\Delta_{01} = 0$. However, for sufficiently small detunings, the population density is irreversibly changed; the population remains in the excited state even after the excitation pulse. This is illustrated in figure 23 D for a detuning $\Delta_{01} = c$. Note also the Rabi Oscillations that are damped in time due to the coherence loss mechanisms outlined in chapter 4.

An ionization laser can probe this excited state population. The time at which this second laser is fired is crucially important for the experimental linewidth. If the second laser is fired simultaneously with the first laser, atoms will be ionized in essentially the entire detuning range shown in figure 23. This is further illustrated in plot B of this figure by showing the population as a function of the detuning at a time $t = a$. If on the other hand the second laser is fired after the excitation pulse has passed, there will only be ion production within a small detuning range, as can be seen on figure 23 B for $t = b$. The width of the resonances as measured by ion detection will therefore be severely reduced in the second case.

The next question deals with the observables that determine the width of the region in which the population evolves non-adiabatically, since this will determine the experimental linewidth. The adiabatic condition (95) can be used to estimate this non-adiabatic detuning range. It can in principle depend on the laser power and the pulse length T. Detailed analysis reveals that the pulse shape is another important factor in determining the dependence of the detuning range on the pulse length and the laser power. Three important bell-shaped examples will be discussed and expressions for the non-adiabatic detuning ranges will be provided (the calculations can be found in [47], a graphical illustration that supports these calculation is shown in appendix A). These analytical formulas can be determined by (often tedious) manipulations of the adiabatic condition (95).

1. **Gaussian pulse shape**
   A first class of pulse shapes is the Gaussian shape. For these pulses, the maximal non-diabatic detuning range is given by

   $$\Delta_{\max} \propto \frac{\sqrt{\log g/\Delta_{\max}}}{T}. \tag{96}$$

   In other words, population can only remain in the excited state after in the excitation within a frequency range that depends logarithmically on the laser power. Additionally, if the pulse time is longer, this range is reduced accordingly. Gaussian shapes are probably the more common shapes realized by most laser systems, so verification of the logarithmic power broadening dependence is also the most abundant [17, 48]. Figure 24 shows a parametric plot of this equation as well as a plot of $y = \log x$ for comparison.

2. **Sech^n pulse shape**
   The sech^n-like shapes are a family of pulses with a particularly easy analytical maximal non-adiabatic detuning range:

   $$\Delta_{\max} = \frac{n}{\sqrt{2}T} + \frac{2^{2/n}}{2^{3/2+1/n}} \frac{1-n}{g^{2/n}T^{2/n+1}} \tag{97}$$

   Interestingly, for $n = 1$, this reduces to

   $$\Delta_{\max} = \frac{n}{\sqrt{2}T}; \tag{98}$$

   the maximal non-diabatic detuning range is completely independent of power. This means that there is no power

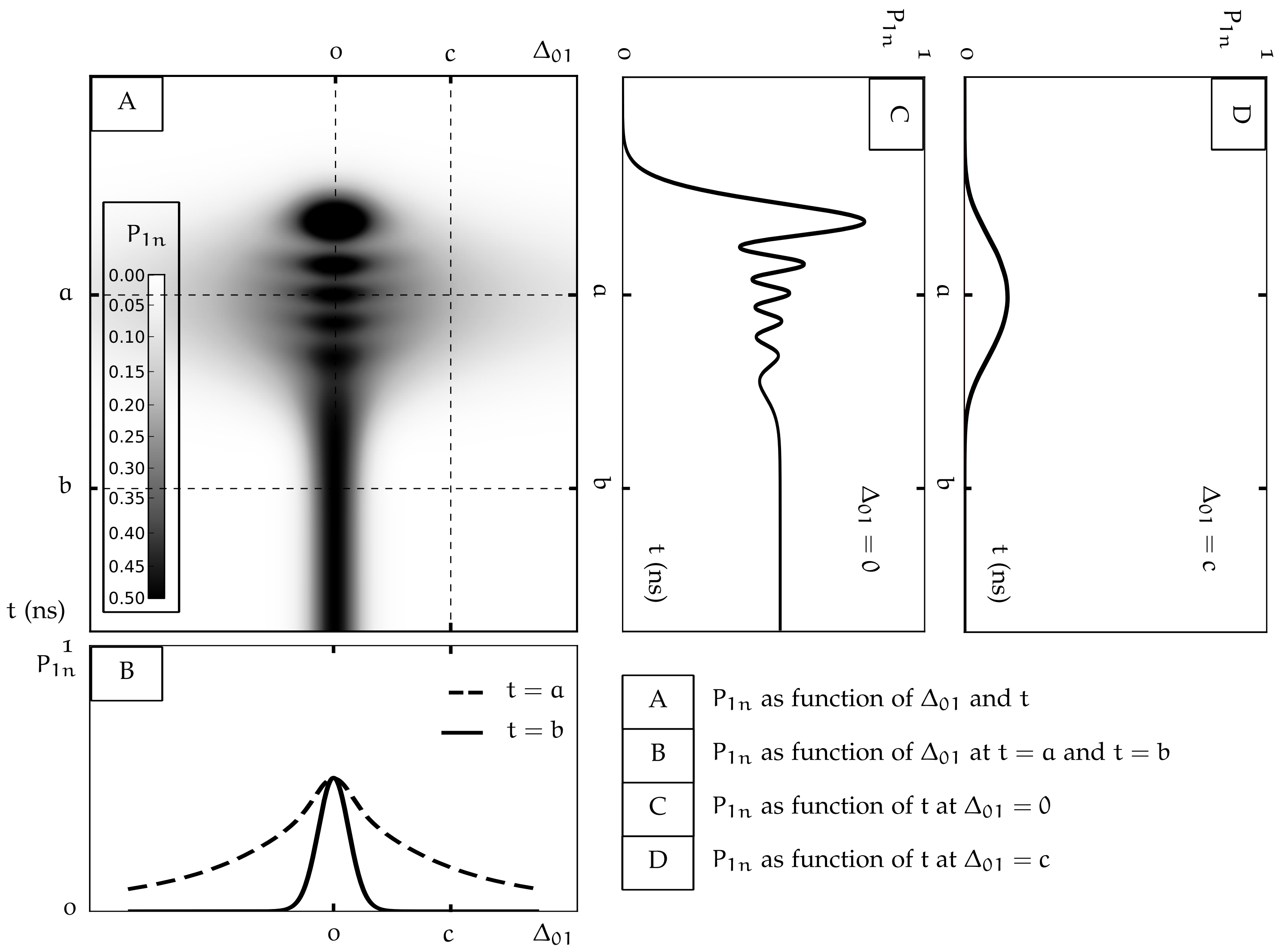

Figure 23: Population of the excited state illustrated as function of time and detuning, with several cuts along either the time or the detuning axis.

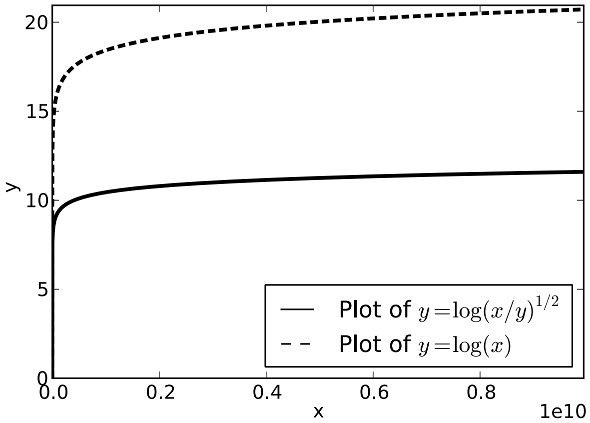

Figure 24: Illustration of the expression (96). For comparison, $y = \log x$ is also plotted.

broadening at all; the width of the excitation spectrum after the actual excitation step is completely independent of power. Note also how an increased pulse length facilitates satisfying the adiabatic condition.

3. **Lorentzian pulse shape**
For Lorentzian pulses, the maximal excitation linewidth is given by

$$\Delta_{\max} = \frac{3\sqrt{3}}{4gT^2}. \tag{99}$$

In other words, the maximal linewidth actually decreases with power. This is perhaps one of the most striking examples of how pulsed laser excitation differs from cw laser excitation.

If the pulses are not bell shaped, it is not the pulse length that determines the power dependence of the resonance widths, but rather the shape of the falling edge and its fall time. For example, if the pulse shape has a Gaussian falling edge with a fall time T, result (96) should be recovered.

Note that results (96,97) and (99) are obtained in absence of any spontaneous decay. The natural linewidth of the electronic states that is due to this spontaneous decay imposes a lower limit on the energy distribution of the electrons. So, for a two-step exciation-ionization scheme, increasing T will reduce $\Delta_{\max}$ up until the natural linewidth, but no further. Similarly, the power narrowing effects for Lorentzian shapes will only narrow the resonances up to the natural linewidth.

Note also that for simultaneous lasing using equation (52) instead of (32) reveals that the factors $i\Gamma$ lead to a breakdown of adiabaticity, which leads to a recovery of the normal power broadening phenomena discussed in section 2.4 [17].

In summary, the post-excitation population of the excited state shows much narrower resonances than the population during the excitation pulse. This is due to the adiabatic evolution of the system outside of a certain detuning window. This window is determined by the pulse length: increasing this pulse length makes the resonances narrower (until the natural width is obtained). Depending on the pulse shape, the energy distribution of the electrons can either experience power broadening, be independent of power or even undergo power narrowing.

6.1.2 *Time-Separated Laser Pulses and Precision*

If the second laser is not present during the excitation step, the ionization spectra will inherit the width of the excited state population. This linewidth is significantly less then what would be obtained for simultaneous laser pulses. This is also due to the fact that the power broadening due to the second laser is also removed completely, as was already mentioned in the beginning of this chapter.

These two aspects are illustrated in figures 25 and 26, which show the linewidth of resonances as function of the power density of respectively the first and second laser, with both lasers modeled as Gaussian pulses with a full width at half maximum of 20ns. The simulations could of course be repeated for arbitrary spatial profiles. Both graphs show this linewidth for simultaneous laser pulses and for separated pulses. The first figure (figure 26) shows how the standard power broadening effects as described in section 2.4 are reduced to a very weak logarithmic dependency on power as the two pulses are pulled further apart. In this plot, a rescaled laser power of 1 is already very deep in the saturation region, proving that the theoretical description holds up even for very high laser powers. There are still some oscillations on top of this logarithmic behavior due to the approximate nature of the numerical simulations.

Figure 26 shows very clearly that all power broadening due to the second laser is removed. Power broadening due to the first laser is also reduced significantly (as was shown on figure 25, which is why the width at very low powers drops from 200 MHz to 120 MHz.

By separating the laser pulses there will be a relaxation of some of the population in the excited state to the ground state. Depending on the choice of transition this relaxation can be reduced. There is also an upper limit to the total efficiency of the two-step ionization, since at most 50 percent of the population can be excited by the excitation pulse. In the case of simultaneous pulses, 100 percent efficiency could in principle be reached; the second laser constantly takes electrons to the continuum, and

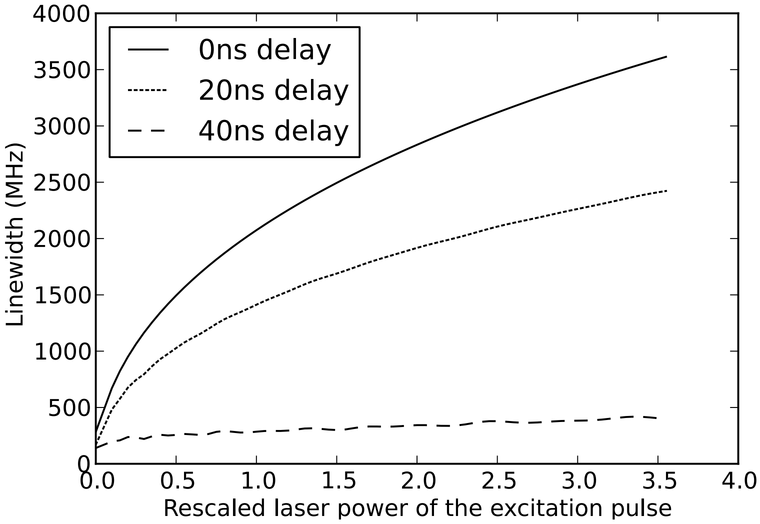

Figure 25: Linewidth as function of a rescaled power in the first step, shown for several delays between the first and the second laser. The pulses are 20ns long. A rescaled power density of 1 is already very deep in saturation. The power in the second step is constant for all points on this figure and is very deep in the saturation region.

an equilibrium distribution is only attained when both states are empty.

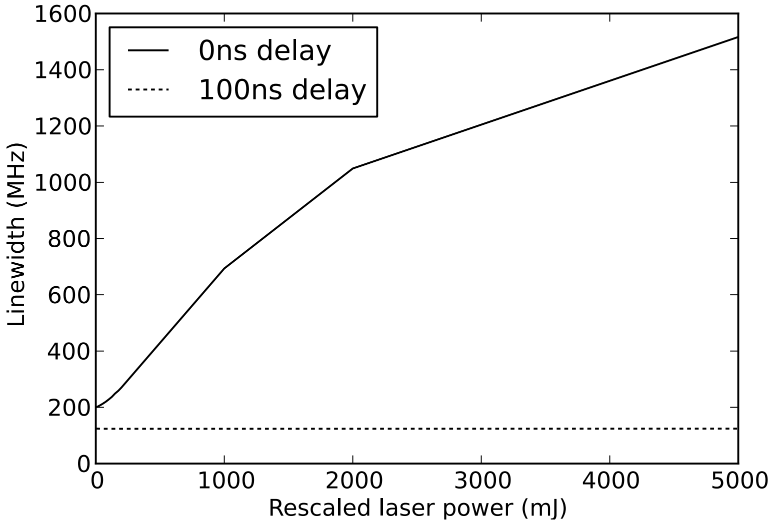

Figure 26: Linewidth as function of power in the second step (in mJ per pulse), shown simultaneous and delayed laser pulses. The pulses are 20ns long. The power in the first step is constant and near saturation for all points on this figure.

6.1.3 *Time-Separated Laser Pulses and Accuracy*

In chapter 5 it was demonstrated how the presence of an ionizing laser during the excitations can lead to modification of the ionization spectra which in turn results in incorrect extraction of the hyperfine splitting parameters. Figure 18 in particular demonstrated large power-dependent deviations. The previous section of this chapter argued that delaying the ionization until after the excitation step removes power broadening due to this ionization laser since the electronic states are only perturbed after their energetic structure is probed by the first laser. This argument explains equally well why all ionization-related deviations in fitted energy splitting should disappear if the ionization step is separated in time from the excitation step; the system is only perturbed after the energy levels are probed.

Figure 27 illustrates this statement. The data shown is simulated using the exact same simulations setting as 18, but with a delay of 75ns instead of 0 ns (the pulse length of both lasers is 25ns). Note how it is only the first laser power that determines the relative deviation between the fitted and real value. Note also how this deviation is significantly lower for the data obtained with the delay. This is further illustrated by figure 28. The relative deviations for the data simulated with simultaneous excitation and ionization is represented with squares. The data obtained with the exact same set of simulation parameters, but with separated laser pulses is shown with filled circles. As section 6.1.2 already discussed, the resolution obtained with delayed ionization is better, which is why the figure has two scales for the x-axis. The scale shown at the top of the figure shows the resolution obtained with simultaneous pulses, the scale on the bottom with separated pulses.

The similarities in the trends in the simulated data motivate a scaling of the relative deviations by a factor $\frac{P_1^{ref}}{P_1}$, where $P_1^{ref} = 0.1P_1^{sat}$. The rescaled data is shown in figure 29; the rescaling makes all the simulated data fall onto a same curve.

Two things should be noted regarding this rescaling:

- It is independent of the power of the ionizing laser, proving the claim that the influence of the second laser step is indeed completely absent from spectra obtained with delayed ionization
- It can be experimentally determined by making determining $A/FWHM$ by fitting the spectra, and the power by making a saturation curve measurement.

The combination of these two remarks allows for an accurate determination of both the size and sign of the deviation made by choosing the simple Voigt fitting model, using only quantities

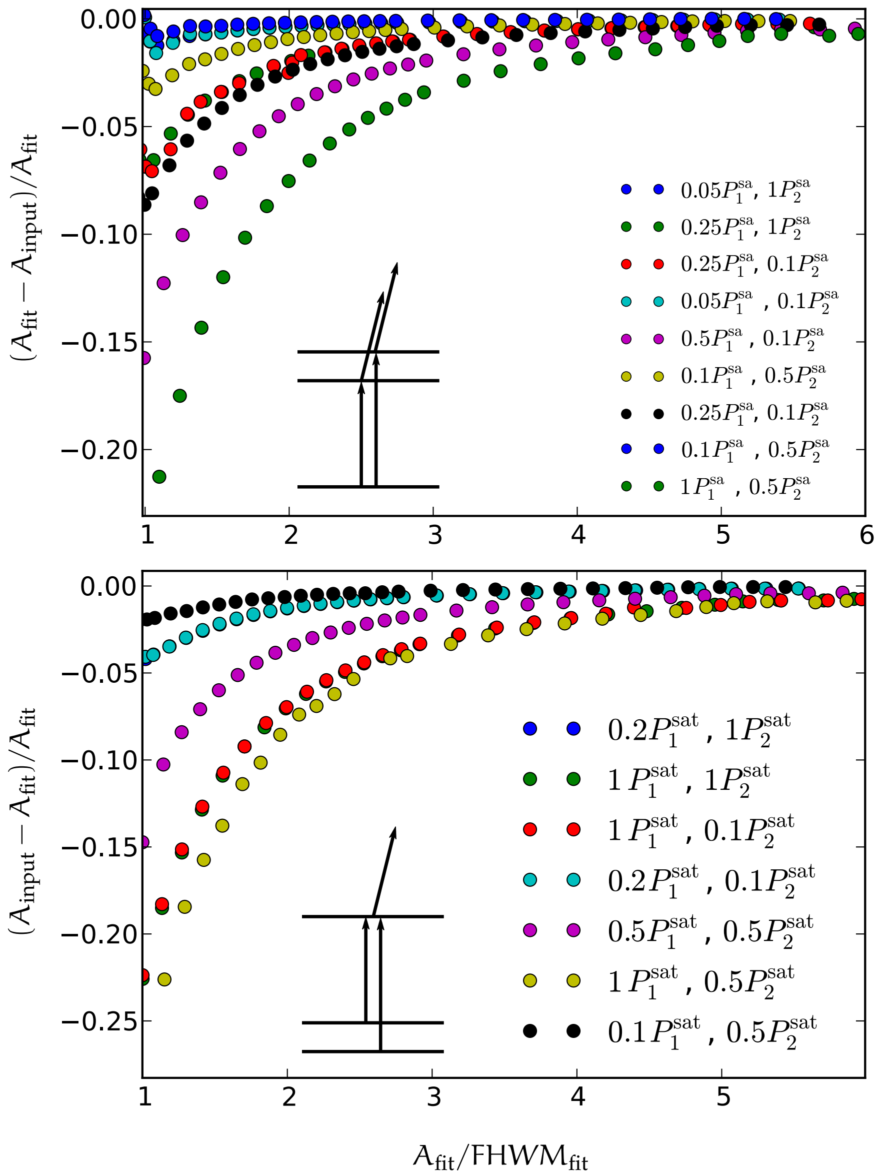

Figure 27: Relative deviation on extracted hyperfine parameters. The results for everal different laser power combinations and input A parameters are plotted, always with the second laser delayed by 75 ns with respect to the excitation laser. The scale on the x axis is the fitted hyperfine splitting divided by the fitted FWHM, a measure for the resolution of the experiment. Compare also to figure 18 which was obtained using the exact same simulations settings but without the delay.

that can be experimentally determined (e.g. the power of the first laser, the ratio $A_{\mathrm{fit}}/\mathrm{FWHM}_{\mathrm{fit}}$). Making the same (or any other obvious) rescaling case of simultaneous laser pulses is not as successful. A more complicated approach taking the laser power of both lasers into account would be needed.

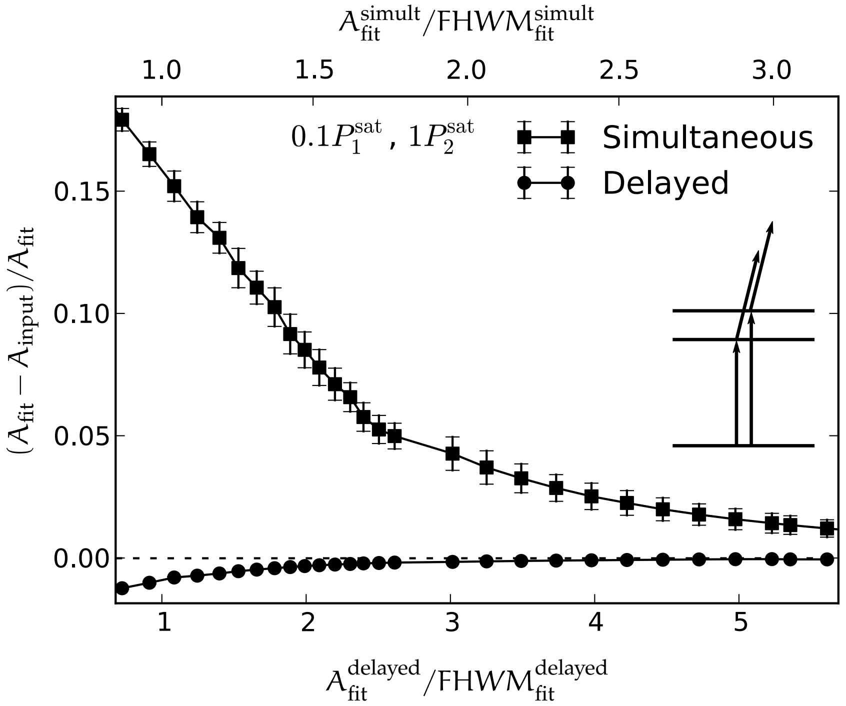

Figure 28: Comparison of simulated data with and without the delay. The scale on the x-axis is the resolution of the data without delay for easier comparison. The resolution for the data obtained with the delay is a factor of two better.

The fact that the relative deviation is not always identically zero reflects the idea that the post-excitation population has some memory of what happened during the excitation pulse. This is illustrated in figure 30; the shape of the population spectrum of each of the states in the excited doublet is not symmetric during the excitation. This is because during the excitation pulse these two states were mixed and therefore influenced one another. The consequences of this interaction (i.e. the asymmetry of the excitation spectra) are not completely removed as the pulse dies out, as can also be seen on figure 30.

6.2 CONCLUSIONS ON TIME-SEPARATED LASER PULSES

The observations in this chapter show that delaying the ionization pulse until after the excitation has finished removes all ionization-induced effects on the ionization spectra. Furthermore, the quantum mechanics of pulsed excitations allows for adiabatic population return of population. These two observations have lead to the following two results:

- The **resolution** (precision) of RIS can be improved considerably due to removal of power broadening resulting from both lasers. This reduction in power broadening is a par-

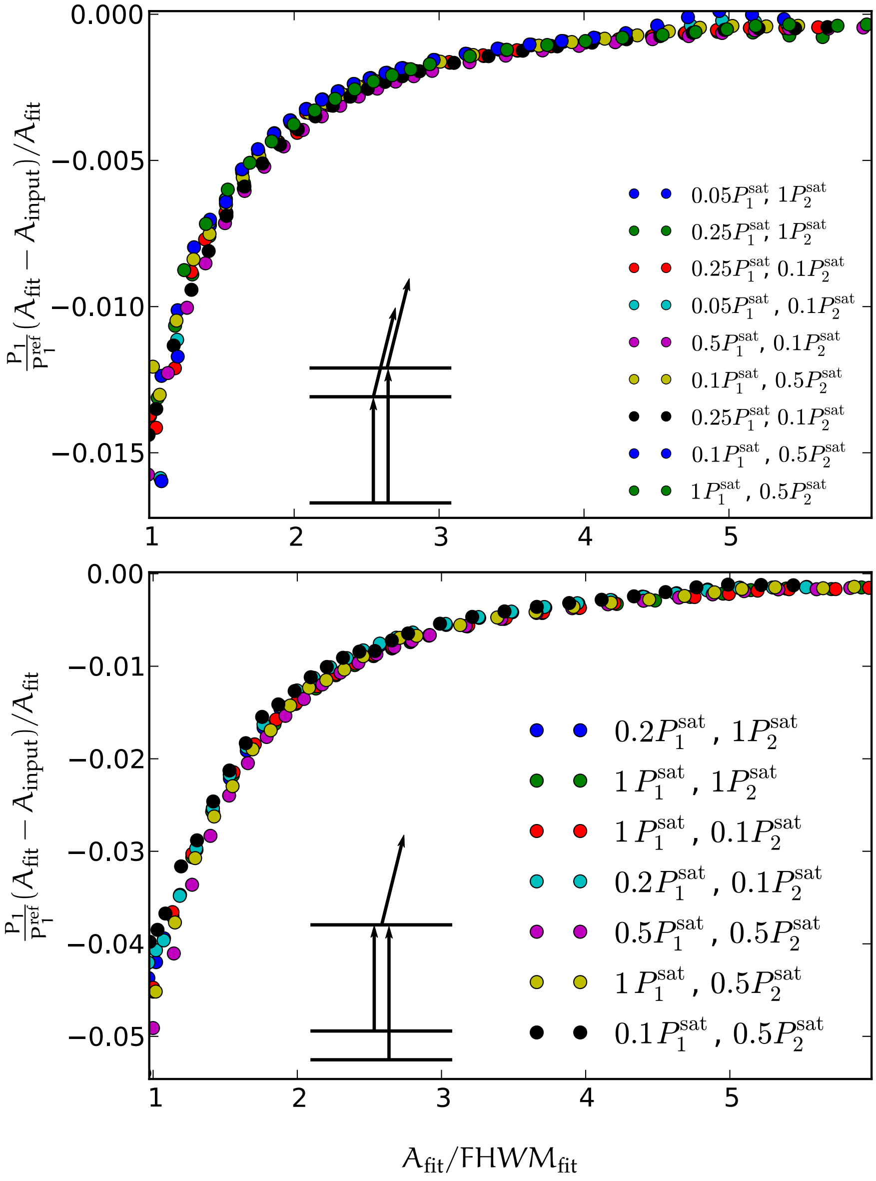

Figure 29: As figure 27, now rescaled by a factor $\frac{P_1^{\text{ref}}}{P_1}$, where $P_1^{\text{ref}} = 0.1P_1^{\text{sat}}$. Note how the curves fall on top of each other.

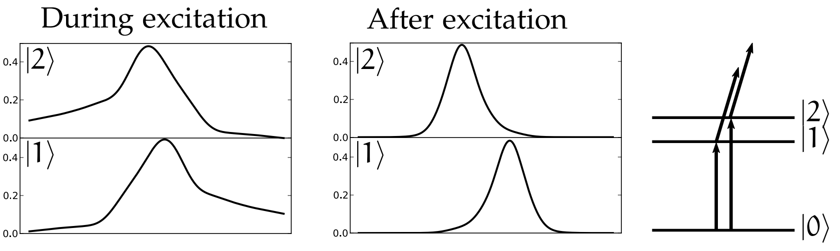

Figure 30: Population of the excited states during and after the excitation. On the right the levels and their labels are shown. Note the asymmetry during the excitation and how it remains after the excitation, though in considerably reduced.

tial reduction for the excitation step and a full reduction for the ionization step

- The **accuracy** of RIS can be improved significantly on two separate levels. Firstly, the deviations in the fitted hyperfine splitting are reduced considerably. Secondly, the deviations that are still present can be easily parametrized by determining the experimental resolution and the power relative to the saturation power. This parametrization has been verified up until saturation, which is the typical regime experiments would be performed in.

Part III

EXPERIMENTAL TESTS

7

EXPERIMENTAL TESTS

An experiment was proposed to test the theoretical predictions made in chapters 5 and 6 in late January, and subsequently realized in March. The goals of these tests were the following:

1. Determining saturation powers, resolution, efficiency for both cw and pulsed excitations for alkali atoms (in this case potassium),
2. Investigating power-related lineshape effects,
3. Testing of adiabatic population transfer mechanisms for pulsed excitations (efficiency and resonance linewidth)

All three goals are preferably realized in a Doppler-reduced or Doppler-free way, such that only the atom-laser interactions determine the line shapes and widths. Both photon and ion detection should be carried out since photon is technically easier to realize and because it allows determination of the Doppler broadening before attempting RIS.

This section describes the experimental setup that was constructed to reach these goals and discusses the results.

7.1 EXPERIMENTAL SETUP

The RIS tests were performed on atomic beams of K. These beams were produced from a potassium salt using a direct current-heated Tantalum oven. This oven was put in a vacuum chamber capable of reaching pressures of 9×10^{-7} mbar in absence of oven heating. The pressure equilibrates at 3.6×10^{-6} mbar with a heating DC of 10A. At these temperatures, a fraction of the K vapor is ionized through surface ionization. These ions are prevented from reaching the laser-atom interaction region by applying a positive bias to a grid placed just above the source. The neutral atoms are not affected by the potential grid and pass into the interaction region.

The laser-atom interactions take place in a cylindrical light collection region, schematically shown in figure 31. The geometry of the system is such that the lasers make a 90 degree angle with the atomic beam axis. This geometry differs from the CRIS geometry but does not change the laser-atom interactions. A pair of slits is used to reduce the velocity spread of the atoms along the laser propagation axis. The light collection region reduces the scattered light observed by the photo-multiplier tube mounted onto the vacuum chamber. Additionally, several baffles and collimators were installed along the path of the laser beam with the aim of reducing the amount of scattered light that reaches the PMT. The main sources of laser scattering are the two Quartz windows used to let the laser enter and exit the vacuum chamber. The entry window was set at the Brewster's angle to further reduce this scatter, and is mounted 0.5m away from the interaction point. The exit window is a flat window and a significant source of scattered laser photons. The distance from this flat window to the interaction point is 30cm.

Through the use of imaging lenses the solid angle of the PMT is increased to ??. In addition to the PMT, an Multi Channel Plate detector is also installed on the vacuum chamber. The distance from the interaction point to the MCP is 40cm, allowing for time-of-flight identification and separation of the ions. To help guide the ions across this distance, a second grid is mounted in between the interaction point and the MCP and kept at a negative voltage.

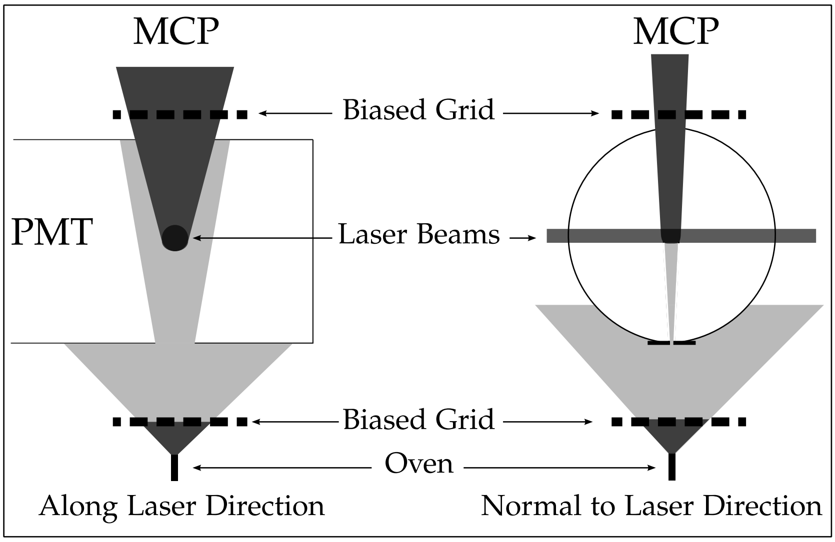

Figure 31: Schematic diagrams of the oven, interaction region and the light collection region that surrounds it. Also shown are the two grids and the Doppler-narrowing slits. The atom beams are shown in a lighter shade than the ions.

Ionization is achieved using a two-step ionization scheme. The first step relies on a cw Ti:Sa laser to provide 769nm light to perform resonant excitations of the electrons from the $4s_{1/2}$ ground state to $4p_{1/2}$. Both states are hyperfine split into a doublet which results in four transitions (labeled A,B,C and D on figure 32). The second step is a non-resonant ionization step which requires 355nm photons, obtained by frequency tripling 1064 light from a Nd:YAG laser. This laser arrangement can produce up to 300mW of 769nm light and 5mJ per pulse of 355nm. The reson-

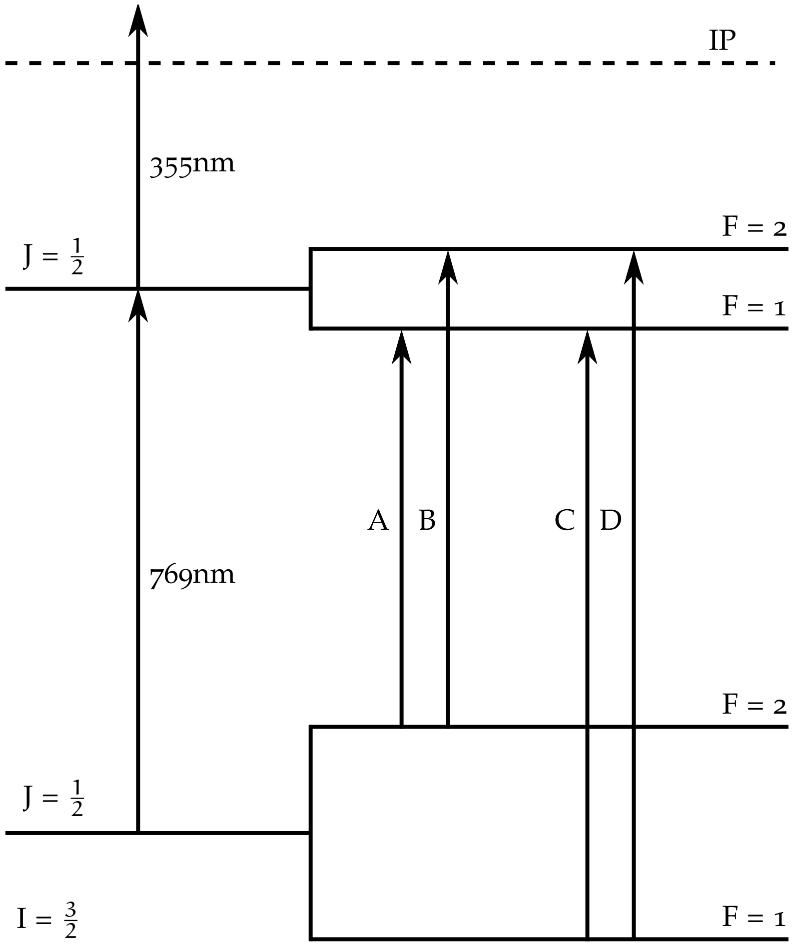

Figure 32: Electronic level scheme of ^{39}K for the transition used in this work.

ant step can be performed by continuous excitation or by chopping the cw light into pulses using a Pockels cell. This optical element uses a birefringent crystal. By applying a 3.6kV voltage the polarization of the crystal can be rotated 90 degrees. A fast high voltage switch therefore allows for extinction of the laser light by three orders of magnitude or full transmission depending on the relative polarization of the crystal and the laser light. By chopping the beam it is possible to begin testing the theoretical predictions of chapter 6 without using a really pulsed laser for step 1.

7.2 RESULTS

The discussion of the results is divided into two parts; one devoted to scans with a continuous excitation step, the other to scans with a pulsed excitation step. The first part of this section will mostly illustrate the presence of power-induced resonance position shifts, making it related to chapter 5 while the study with pulsed excitations should be read in the context of chapter 6.

7.2.1 *Continuous excitation*

Both fluorescence detection and RIS was performed on the K beams, allowing a side-by-side comparison. Figure 33 shows two scans, the left one using ion detection after RIS and the right one using photon fluorescence detection. In both cases the excitation is continuous. The ionization step was pulsed. The ion scan was recorded using 0.5mW of 769nm and 1.6mJ of 355nm, while the photon scan was taken using 1mW in the resonant step. These spectra clearly show the well-resolved hyperfine spectrum associated with the Doppler-collimated atomic beam that has passed through the slits. The four narrow peaks sit on top of a broad structure. This broad structure is due to a considerable residual vapor that fills the chamber and the interaction region. This rarified gas has a large velocity spread, leading to Doppler-broadened resonances in the hyperfine spectra. The photon spectra have an additional background since the PMT also detects scattered laser photons.

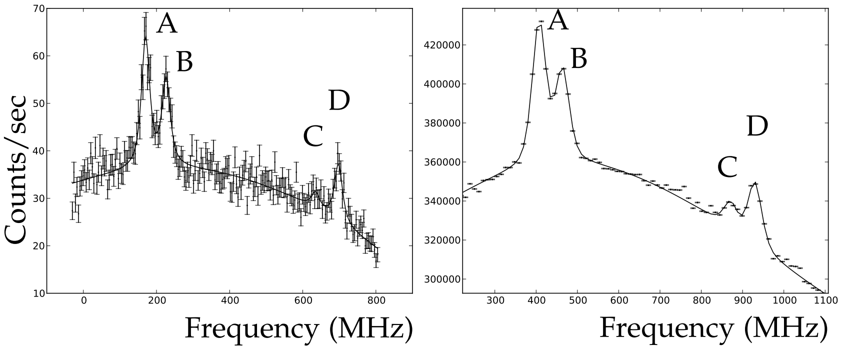

Figure 33: Ion (left) and phton (right) spectrum of ^{39}K taken in similar conditions. The solid line is the best fitting curve obtained by the procedure outlined in the main body of this text.

The solid line is the best fit obtained through a least-squares minimization. The fitting model is the sum of several components needed to take the observations of the previous paragraph into account. So, the fitting function contains four narrow Voigt profiles with the same width, but with free positions and intensities. Additionally, four wider Voigt profiles are added at the same positions as the narrow peaks, once again with free intensities but the same width. These are used to fit the large, broad distribution underneath the four narrow peaks.

A lot more statistics are collected per second for the photon signal. One reason for this is the suboptimal ion optics present in the ABU in its current form. The main reason however is that the excitation step happens continuously, while the ionization step happens via a 20Hz repetition rate pulse that is only a few nanoseconds long. This duty cycle loss results in lower statistics.

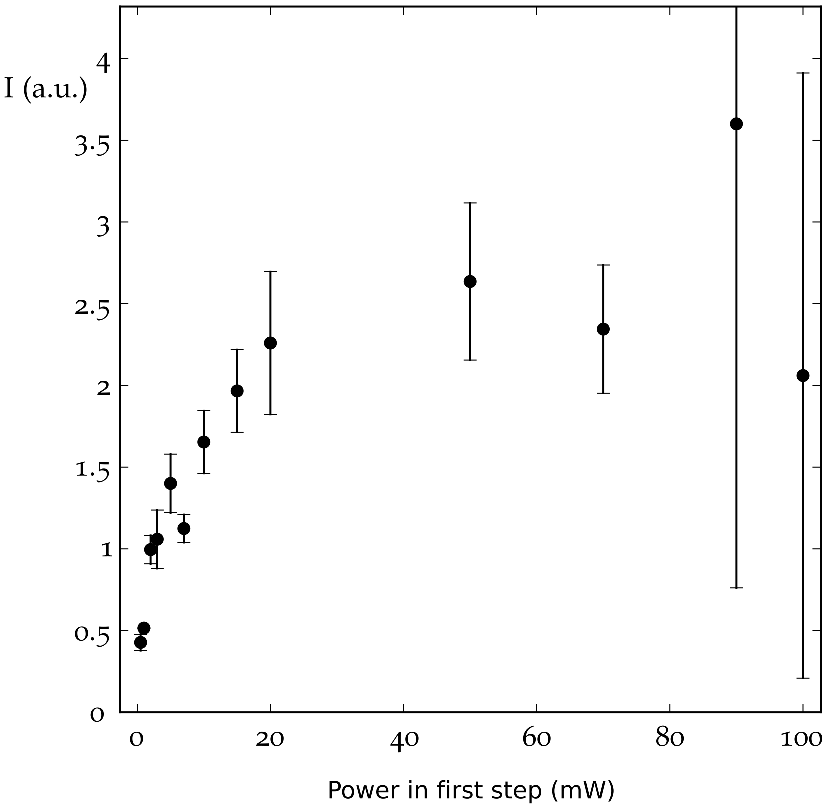

Figure 34: Saturation curve: Intensity (normalized to reference scans taken in between every measurement) of the leftmost peak of the hypefine spectrum of ^{39}K as function of power density used for the first step of the ionization process.

Figure 34 shows the saturation curve for the excitation step. This figure demonstrates that the transition reaches saturation at approximately 30-40mW for the narrow structures. Figure 35 shows the widths of the narrow peaks at the laser powers of figure 34. Figure 36 shows the difference in frequency of the two transitions from the $F = 1$ hyperfine ground states to the two excited states as function of the power in this excitation step. Figure 35 illustrates how the width of the resonances increases with the power density, as expected (compare for example to 25 at 0 ns delay). Figure 36 shows that an increase in power density results in a shift in the peak-to-peak distance of the resonances. Figure 37 shows a few examples of ion scans at several laser power densities, illustrating both the increasing widths and splittings. The splittings increase by a factor of three when going from a few mW to 100mW, an effect far larger than what the model developed in this thesis can account for. Further research is needed to understand this effect.

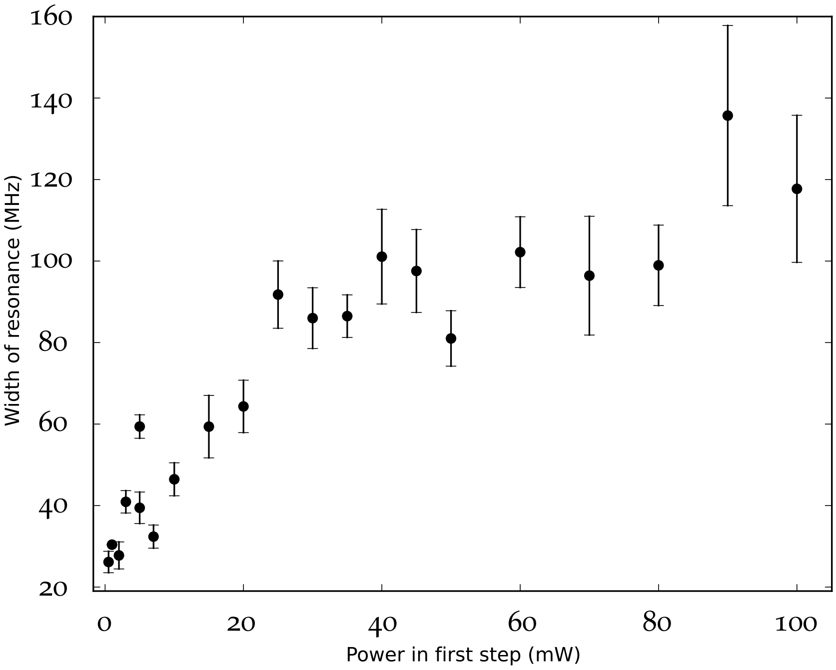

Figure 35: Full Width at Half Maximum of the narrow Doppler-narrowed peaks in the ion spectra as function of the power in the first step.

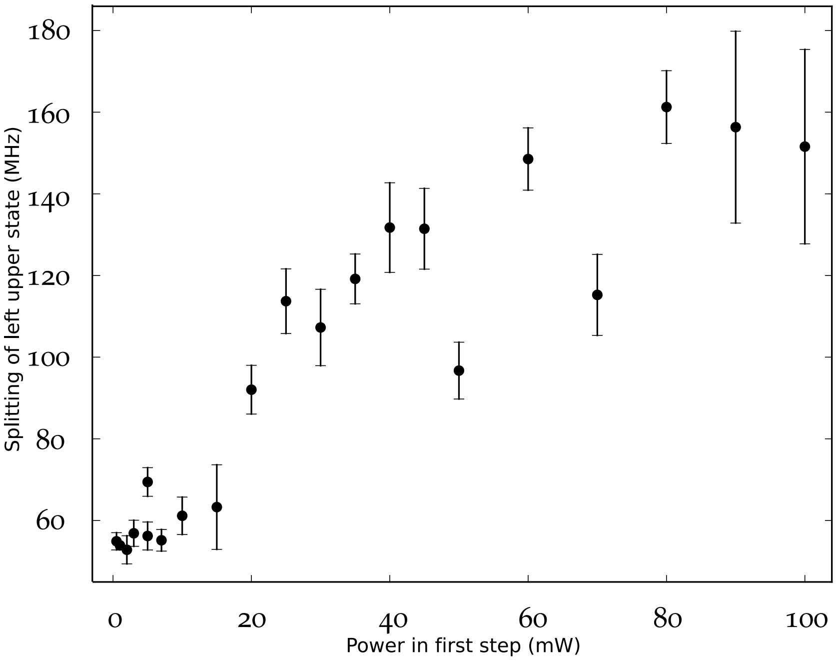

Figure 36: Splitting of the narrow Doppler-narrowed peaks in the left doublet of the ion spectra as function of the power in the first step.

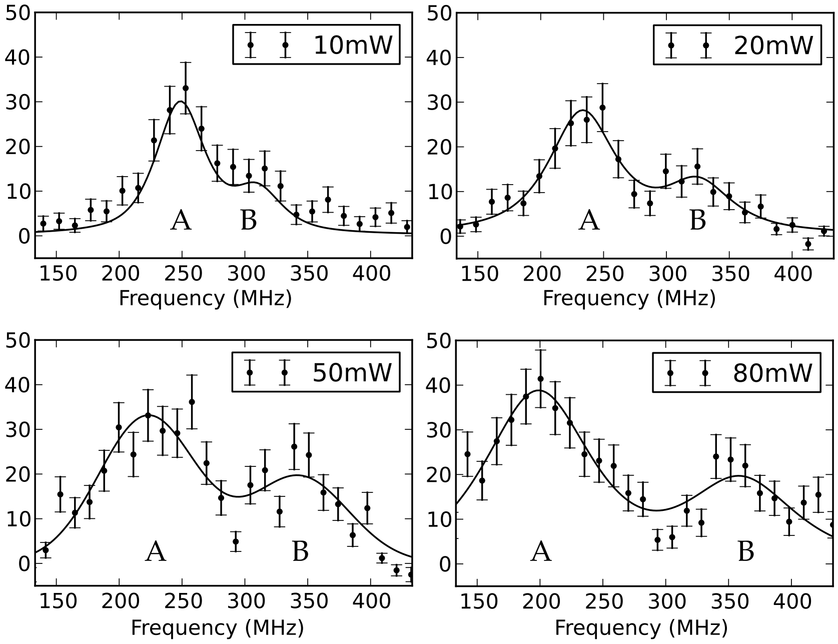

Figure 37: Ionization spectra after subtraction of the Doppler-broadened contribution of the rest gas for various Ti:SA laser power densities. Experimental data and the best fit for the transitions from F = 1 to the two excited states of ^{39}K is shown, as function of frequency. The Doppler-broadened component is subtracted from the total ion rate.

7.2.2 *Pulsed Excitation*

The second stage of the experiment consisted of using a Pockels cell placed in the optical beam path to chop the cw light, effectively making it into a pulsed laser. All measurements discussed in this chapter were obtained with an excitation pulse of 100 ns FWHM, as seen by a 1 GHz sample rate photo diode. The extinction rate of the Pockels cell is 1/500, which means that there is still some cw laser light present in the interaction region. To determine the influence of this remanent light, the ionization laser was timed to 200 µs before the excitation pulse. Figure 40 shows the resulting ionization spectrum, as well as a spectrum obtained by temporally overlapping the excitation and ionization pulse. The remanent light is still sufficiently intense to excite a small fraction of the population to the ground state, but the contribution of the pulsed excitation is dominant.

The passage through the Pockels cell and the analysing optics reduced the power of the laser pulse by a factor of 3. Figure 39 shows the saturation curve for the available power densities. The intensities have been normalized to reference measurements at a chopped 18 mW cw beam. For reference, a zoom-in of the saturation curve for a cw excitation step is also repeated from figure 34, still normalized to cw reference scans at 50 mW. The data re-

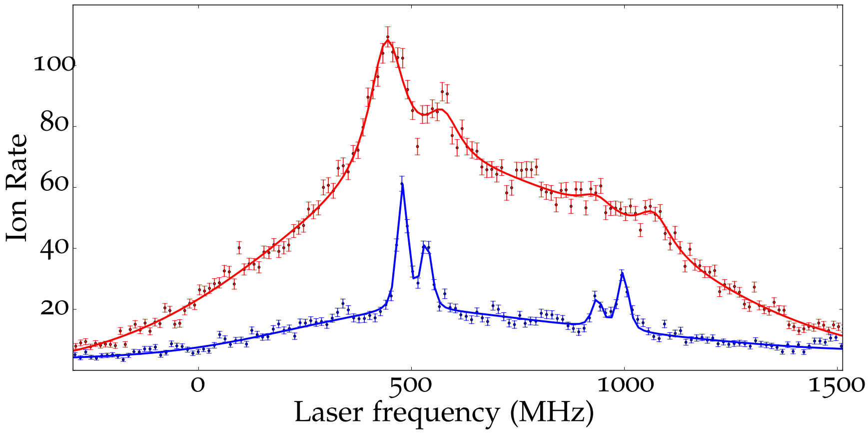

Figure 38: Comparison of a scan with a cw first step (red) and a scan with a pulsed excitation step (blue). The excitation power is 40mW, the ionization pulse has 1.6mJ per pulse. The two scans were taken at different moments in during the experimental run; the pressure was lower for the pulsed excitation measurements. This explains the reduction of the Doppler-broadened structure underneath the narrow peaks.

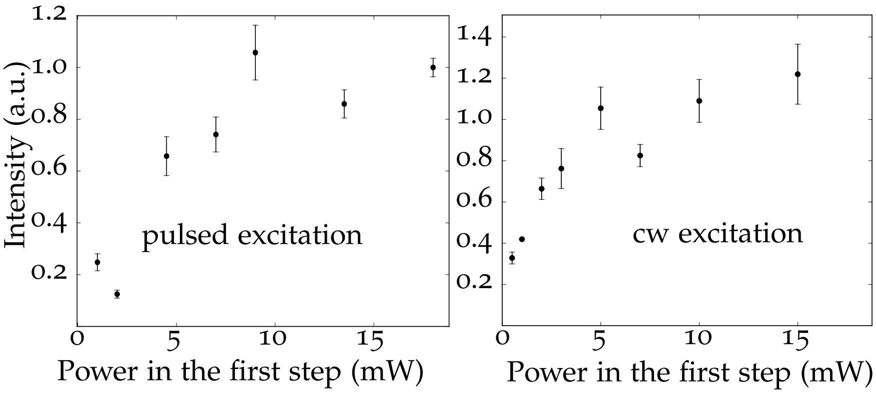

Figure 39: Left: Saturation curve for pulsed excitation and delayed ionization. The intensity in the two narrow peaks normalized to reference scans at 18 mW taken in between scans. Right: saturation curve for a cw excitation step, normalized to the saturation intensity.

quired for the chopped saturation curve was made by delaying the 1064 nm light to 100 ns after the end of the excitation pulse. The powers on the x-axis of this chopped saturation curve were measured by sending the laser beam through the pockels cell while it is not chopping (i.e. by constantly applying the maximal voltage).

Figure 38 compares two ionization spectra of the full hyperfine spectrum, one obtained with a cw first step, the other with the first step chopped and the second laser firing after the excitation pulse. The laser setup was the same for both scans, with 50 mW power in the excitation step. However, the cw scan was taken in a higher-pressure environment. This explains the reduc-

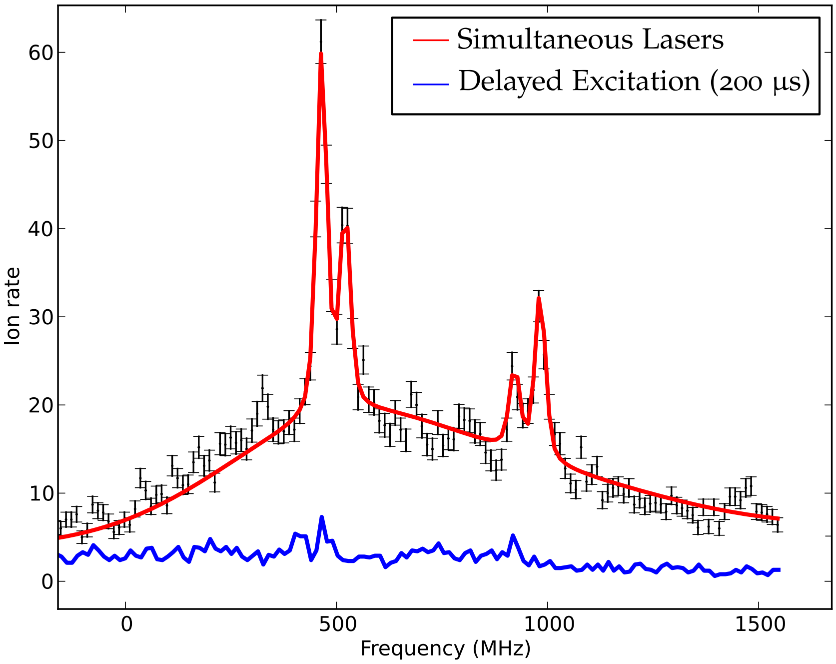

Figure 40: Left: Ionization spectra obtained by ionizing during the excitation (blue, labeled 'Simultaneous Lasers') and ionizing before the excitation (red, labeled 'Reverse Timing').

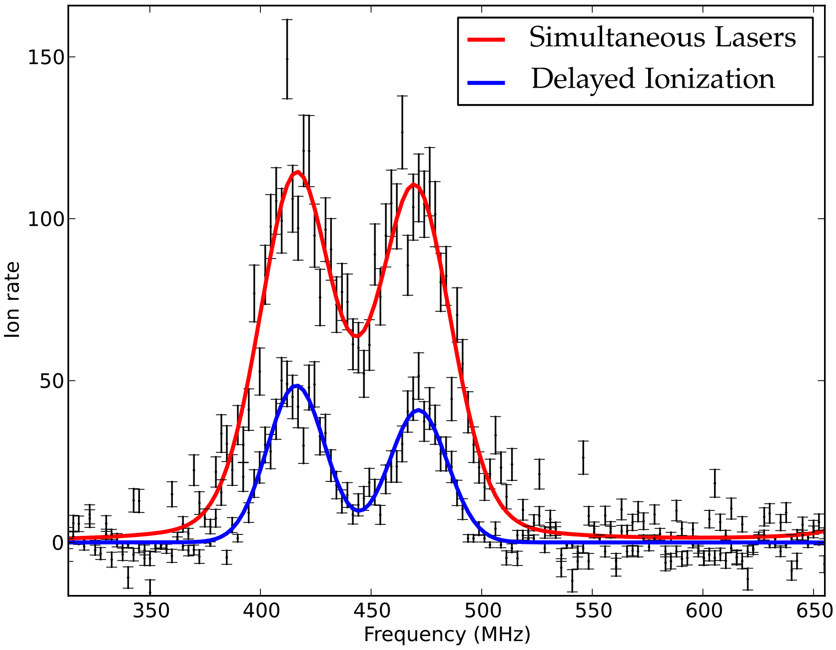

Figure 41: Ionization spectrum of just the A and B transitions, with simultaneous laser pulses (blue) and with the ionization pulse delayed until after the excitation pulse (red).

tion of the Doppler-broadened structure underneath the narrow peaks. Chopping the first step results in a reduction of the resonance width from 100 ± 11MHz 29 ± 3MHz. The position of the resonances are also no longer shifted, which results in a recovery the normal ^{39}K hyperfine splittings.

The delay between both laser pulses can easily be adjusted by changing the trigger to the Pockels cell. Figure 41 compares two ionization spectra, one obtained with simultaneous laser pulses (in red), the other one (in blue) with the ionization pulse delayed to 400ns after the chopping trigger (i.e. to just after the extinction of the excitation pulse which ends at 375 ns). Both spectra were obtained by chopping 18 mW of 769nm light into pulses. Only the A-B doublet is shown. Note how the intensity of the delayed spectrum is reduced due to spontaneous decay. This intensity loss could be mitigated by choosing a transition to an excited state with a longer liftetime (the lifetime of the excited $4p_{1/2}$-state is 26.3 ns [46]). The width of the resonances is also smaller for the delayed pulses; it drops from 39(3) MHz to 26(2) MHz. How both the intensity and the width of the resonances depend on power and on the delay between both pulses is investigated next.

By changing the timing of the trigger to the pockels cell, the arrival time of the ionization pulse pulses can be delayed relative to the excitation pulse. The top plot of figure 42 shows that the width of the ionization spectra is reduced if the ionization pulse is delayed after the excitation pulse, as was predicted in chapter 6. When the delay is larger than 375ns the width of the resonances drops down from a weighted average of 38 ± 1MHz to a weighted average of 25 ± 1MHz. This last value matches the best resolution obtained using this atomic beam unit.

The bottom plot of figure 42 shows the intensity of the resonances as function of the delay. Recall that the excitation pulse starts at 100ns and ends at 375ns. The right tail of the intensity curve shows how the population of the excited state through spontaneous decay, with a decay rate of 26.3 ns. Future work could investigate transitions with a longer spontaneous decay half-life. An important point of investigation is whether or not chopped cw lasers could supply the laser powers needed to saturate the excitation of such a weak transition. The experimental setup used for these tests can still be improved on this point; recovering the power losses at the entry of the Pockels cell could represent a first step towards the study of weaker transitions.

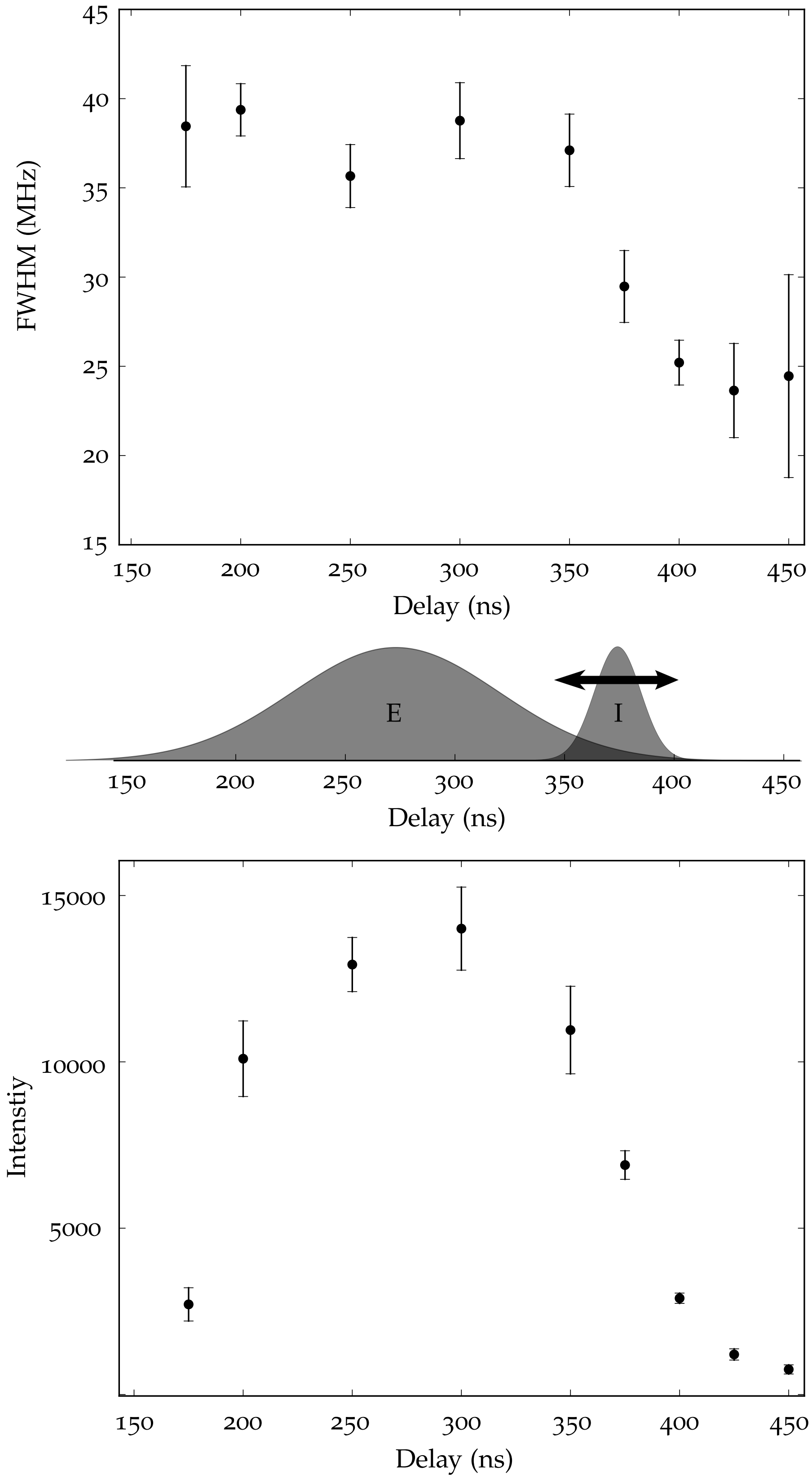

Figure 42: Top: Width of the resonances as function of the delay between the laser pulses. The power density is 18 mW in all cases. Middle: drawing of the laser pulses for a delay of 375ns. Bottom: Intensity as function of the delay between the two laser pulses. For both graphs the excitation laser power was 18 mW.

Part IV

CONCLUSION AND APPENDICES

8

CONCLUSION

This thesis aimed to develop a framework that could handle the coherent nature of the interaction of laser photons with atomic electrons for a two-step resonance ionization process. This framework was developed by deriving equations of motion of the coupled atom-photon system. The equations that emerged from these calculations served as a starting point for the study of two topics.

The first of these two topics can be classified under the umbrella of 'accuracy in resonant ionization spectroscopy'. The interactions of the electrons with the photon field of the excitation laser and the bound-bound couplings resulting from the ionization laser proved capable of influencing the hyperfine splitting that is extracted from poorly resolved ionization spectra by applying the standard fitting routines in laser spectroscopy. These systematic deviations can be up to several percents; the influence of the ionization-induced bound-bound interactions on the hyperfine splitting of the excited states in particular can deviate by several tens of percents. These theoretical findings were compared to published in gas-cell laser spectroscopic data on neutron deficient Cu isotopes. Simulations tailored specifically to this dataset proved capable of explaining the discrepancy between the hyperfine splittings extracted from the in-gas cell data and high-resolution fluorescence data.

The second topic dealt with the issue of 'precision in resonant ionization spectroscopy' and focused in particular on a theoretical study of power broadening due to pulsed laser excitations and ionizations. The key concept required to understand these differences proved to be the idea of adiabatic population transfer. Application of the adiabatic theorem yielded estimates for how the linewidth for post-excitation ionization spectra varies with the laser power, revealing that power broadening for pulsed lasers differs significantly from power broadening due to continuous wave lasers. In particular, for Gaussian pulse shapes, a logarithmic power dependence was established. This and other results provide compelling arguments to further study the role of the delay between the excitation and ionization laser; if the ionization laser is delayed until after the excitation laser pulse has passed, a substantial increase in resolution could be obtained. A first experimental step was already made in this regard, with results that were shown in this work. These results confirm the reduction of power broadening by delaying the ionization step.

These two topics are not independent of one another. This thesis not only suggests that the precision of RIS could be improved by ionizing only after the excitation step, the ionization-related changes in the fitted hyperfine splitting should also be removed completely by doing so. This and other predictions made in this thesis will be tested during the coming summer. This data will provide the ultimate test for the model as it is now. Regardless of the outcome of these tests, there is certainly one aspect lacking as of now: a good description of spontaneous decay. Spontaneous decay is not only required to explain optical pumping phenomena that determine relative peak intensities of hyperfine structure spectra but could also be at the root of the very large increase in splitting observed in figure 36.

A

ILLUSTRATION OF ANALYTICAL ESTIMATES OF THE ADIABATIC REGIME

Consider a a two-level system irradiated by a photon field of frequency ω_a in the adiabatic basis. Chapter 6 argued that application of the adiabatic theorem allows determination of the maximal amount of power broadening a resonance can have after the excitation pulse. Equations 96, 97 and 99 provide expressions for this maximal broadening in terms of the pulse fall time and the power density of the excitation laser. This appendix graphically illustrates the calculations in [47]. These derivations start from equation 32:

$$i\dot{A}(t) = \begin{pmatrix} \lambda_- & -i\dot{\theta} \\ i\dot{\theta} & \lambda_+ \end{pmatrix} A(t) \tag{32}$$

Recall the definition of $\lambda_\pm$ and θ:

$$\lambda_\pm = \frac{1}{2}\left(\Delta_{01} \pm \sqrt{4g(t)^2 + \Delta_{01}^2}\right), \tag{100}$$

$$\theta = \frac{1}{2}\arctan\frac{2g(t)}{\Delta_{01}}, \tag{101}$$

which means that

$$\dot{\theta} = \frac{\Delta_{01}\dot{g}(t)}{\Delta_{01}^2 + 4g(t)^2}. \tag{102}$$

Of particular interest are functions $g(t)$ that are smooth bell-shaped functions of time.

If the coupling of the adiabatic states is very weak the population will stay in its initial adiabatic state throughout the excitation pulse. Note that this does not mean the system stays in either of the bare states; it rather makes an excursion to the other bare state, only to return to the initial state asymptotically (since them the bare states coincide with the adiabatic states).

If on the other hand the adiabatic coupling is strong, the population will not stay in its initial adiabatic state. The final state of the system will therefore always have a component along the excited state vector. This means that population will be transferred to the excited state $|1\rangle$. The maximal width Δ_{max} of the post-excitation excited state population is determined by the diabatic region and is therefore constrained by the adiabatic condition

$$\lambda_+ - \lambda_- \gg \left|\dot{\theta}\right|, \tag{95}$$

which implies

$$\sqrt{\Delta_{01}^2 + 4g(t)} \gg \left| \frac{\Delta_{01}\dot{g}(t)}{\Delta_{01}^2 + 4g(t)^2} \right| \tag{103}$$

Bringing all the terms on one side of inequality 103 reveals a numerically testable criterium for nonadiabatic evolution:

$$\frac{\left(\Delta_{01}^2 + 4g(t)^2\right)^{3/2}}{\Delta_{01}\dot{g}(t)} \gg 1. \tag{104}$$

Figure 43 illustrates expression 104 as a function of the detuning and time for a Gaussian pulse. The laser fires at $t = 0$ and has a FWHM of T. Black areas are areas in which condition 104 is violated and the evolution of the system is diabatic; white areas are areas of adiabatic evolution. Note that there are always two diabatic regions. This is due to $\dot{\theta}$ having two maxima in time at times $\pm t_0$; around these times, condition 95 is hardest to satisfy. An estimate for the maximal non-adiabatic detuning region can be obtained by finding where the black areas of figure 43 are the widest along the detuning axis. Note also how the diabatic region extends much further along the time-axis for the Lorentzian pulse shape. This is due to the much slower power drop in the tails of a Lorentzian pulse.

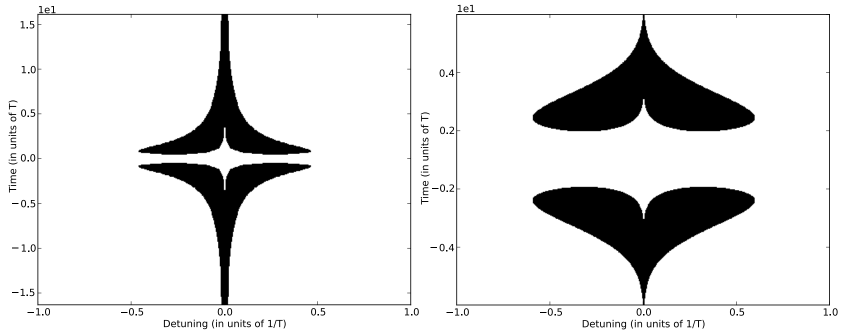

Figure 43: Example of the region in the detuning-time plane where adiabticity is violated (black) for a Lorentzian (left) and Gaussian (right) pulse. The range of detunings for which the evolution is non-adiabatic determines the maximal linewidth of the excited state population.

Figure 44 shows the diabatic regions in the detuning-time plane for several, linearly increasing powers and a Lorentzian pulse shape. The detuning axis is scales inversely with the laser power; the time axis scales linearly with power. This scaling was done with the calculations of [47] in mind; if they are correct, all the diabatic regions should look the same since $t_0 \sim g_0$ and $\Delta_{\text{max}} \sim 1/g_0$. This is indeed what figure 44 shows. Figure 45 presents a different view on the same plots by showing the contour plots of the diabatic regions in the detuning-time plane all on one plot, clearly illustrating that $t_0 \sim g_0$ and $\Delta_{\text{max}} \sim 1/g_0$.

The implications are twofold; the post-excitation ionization linewidth scales inversely with the laserpower and the times at which the evolution is diabatic is linearly dependent on the power. This second point confirms the intuitive arguments for power narrowing presented in [47].

Figure 47 repeats the calculations that led to figure 44, but this time with a Gaussian pulse shape and exponentially increasing powers ($g_i = e^i g_{\text{ref}}$). The theory in [47] predicts the linewidth has a logarithmic power dependence, so the detuning axis is scaled linearly with i. The similarity in maximal widths of the adiabatic regions shown in 47 therefore confirms the logarithmic power broadening. Figure 46 shows the contour lines of the diabatic regions in the detuning-time plane all plotted on one figure. The widths of the diabatic regions increase linearly with the exponent i, once again confirming the logarithmic power broadening.

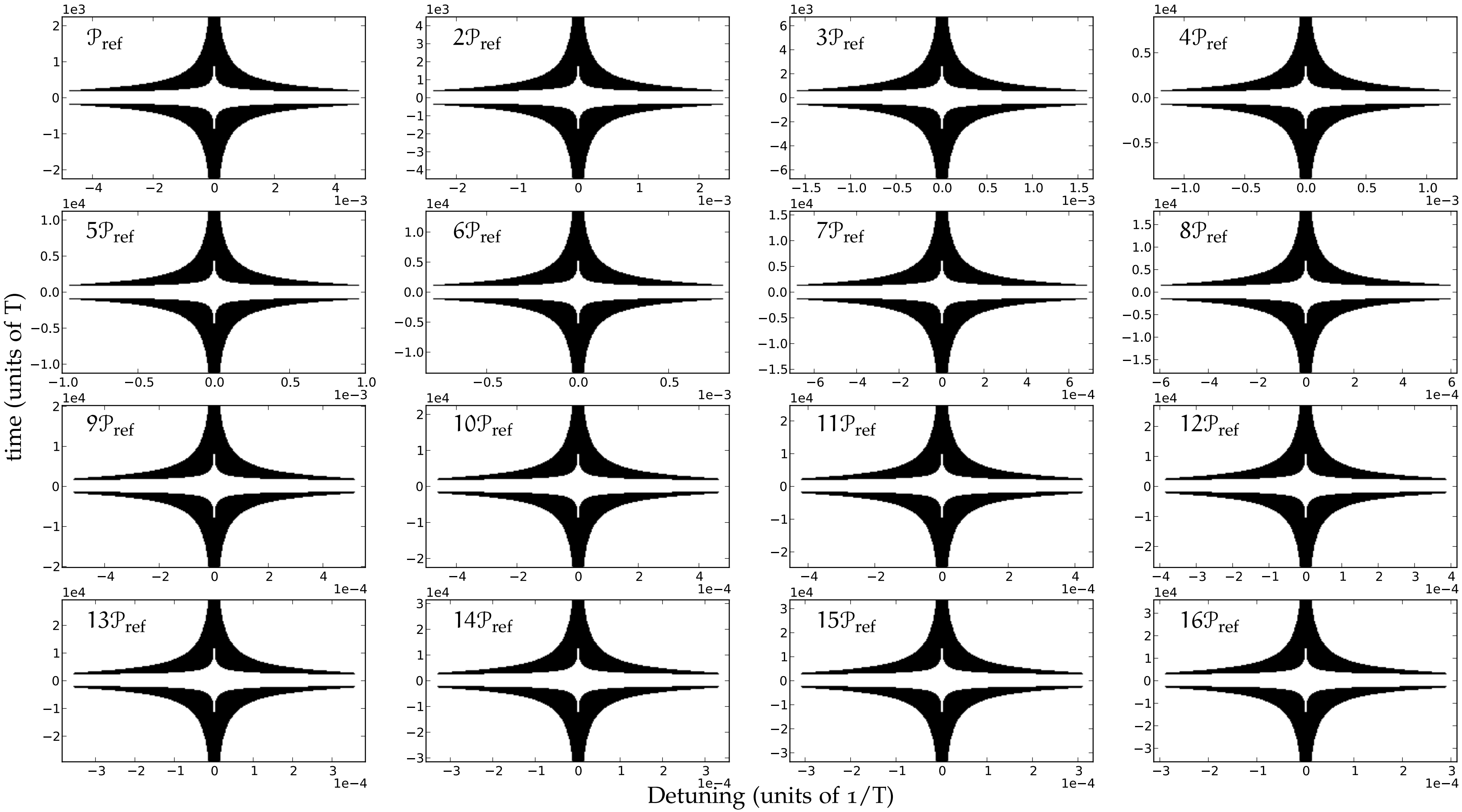

Figure 44: Diabatic region for several laser powers. The detuning axis is scales inversely with the laser power; the time axis scales linearly with power. The excellent scaling of the diabatic regions implies that the linewidth of the post-excitation indeed scales inversely with power.

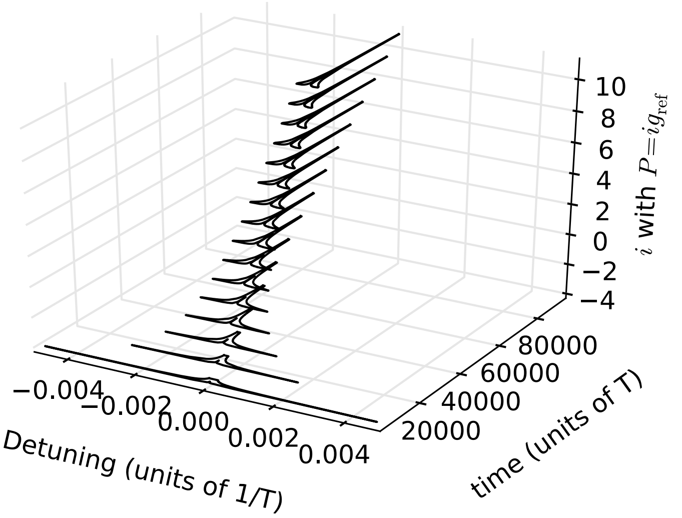

Figure 45: Contour lines of the diabatic regions in the detuning-time plane as function of linearly increasing power for a Lorentzian excitation pulse.

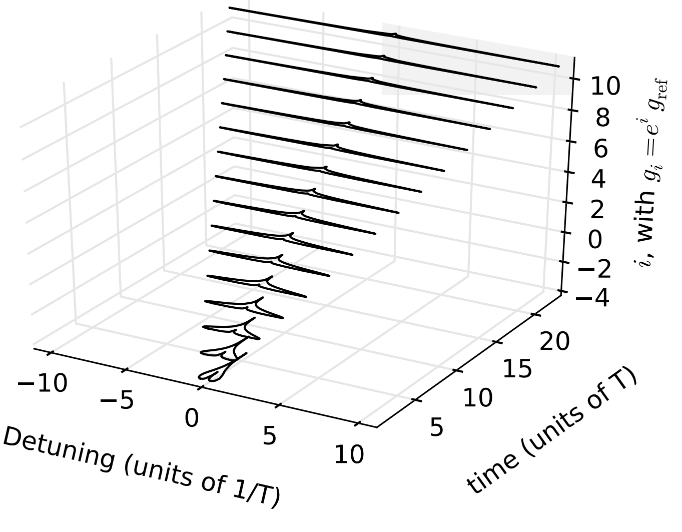

Figure 46: Contour lines of the diabatic regions in the detuning-time plane as function of exponentially increasing power for a Lorentzian excitation pulse.

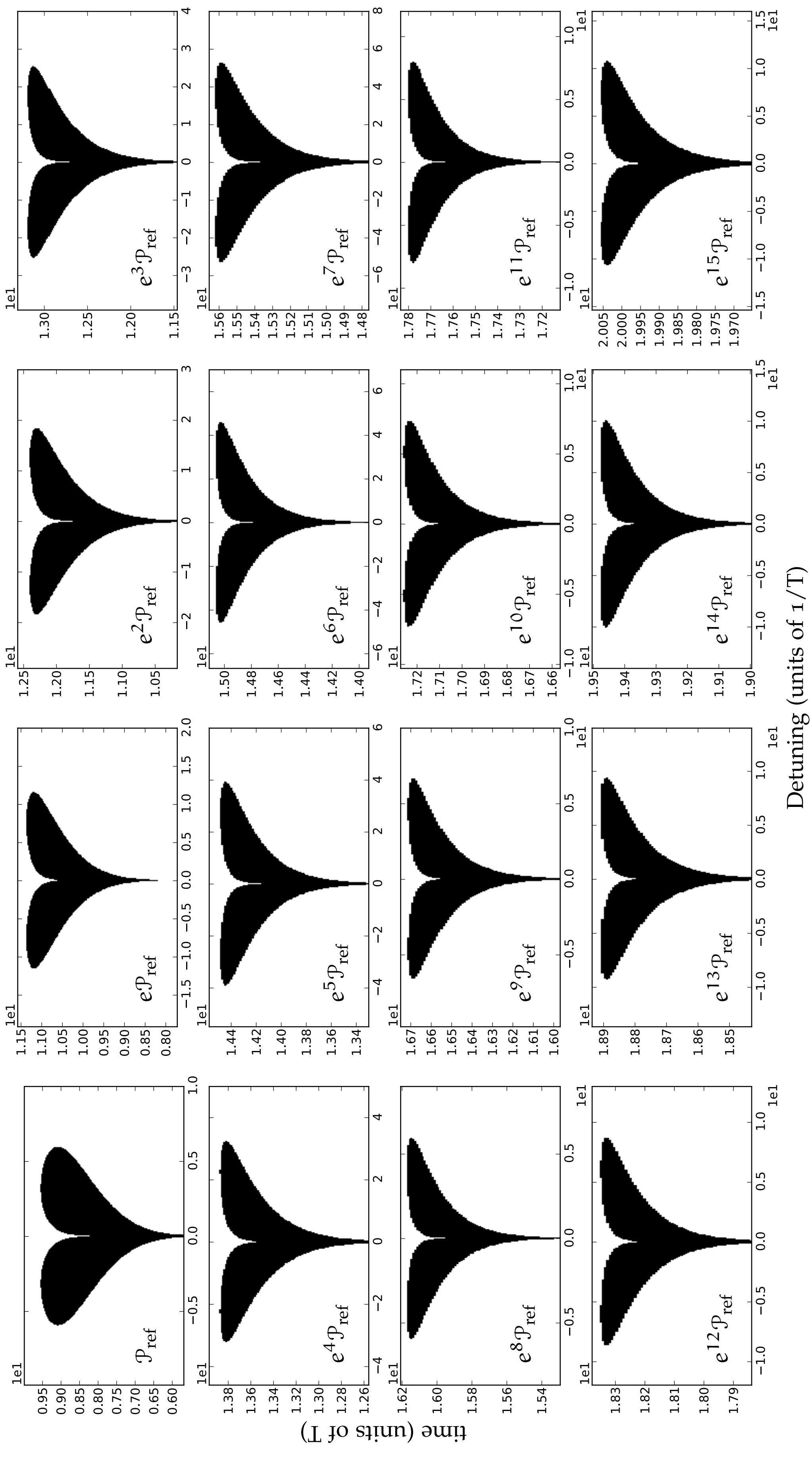

Figure 47: Diabatic region for several laser powers.

B

SIMULATION INPUT FILES

Listing 2: Simulation input file used for the tests in chapter 5

```
Nuclear Spin
0.5

Electronic Spin
0
1

Magnetic Dipole Constants in Mhz
0
150

Electric Quadrupole Constant
0
0

Wavelength of the transitions in nm
422
1064.0

Photo-inisation cross section in 10^-18 cm^2
3

Fano Factor
0

Interaction area in cm^2 (=pi * beam radius^2)
0.3

Oscillator strength
0.286

Duration of the laser pulse in nanosec
25
25

Separation of the laser pulse in nanosec
0

Intensity of the lasers in mJ per pulse
4e-4
0.5

Scanning range of the laser frequency in Ghz
1.4
```

Listing 3: Simulation input file used for simulating the ^{59}Cu data with option 1

```
Nuclear Spin
1.5

Electronic Spin
0.5
0.5

Magnetic Dipole Constants in Mhz
5033
2064

Electric Quadrupole Constant
0
0

Wavelength of the transitions in nm
244
411

Photo-ionisation cross section in 10^-18 cm^2
3

Fano Factor
0

Interaction area in cm^2 (=pi * beam radius^2)
0.3

Oscillator strength
0.0018

Duration of the laser pulse in nanosec
15
15

Separation of the laser pulse in nanosec
0

Intensity of the lasers in mJ per pulse
0.001
1.5

Scanning range of the laser frequency in Ghz
50
```

Listing 4: Simulation input file used for simulating the ^{59}Cu data with option 2

```
Nuclear Spin
1.5

Electronic Spin
0.5
0.5

Magnetic Dipole Constants in Mhz
2000
820

Electric Quadrupole Constant
0
0

Wavelength of the transitions in nm
244
411

Photo-ionisation cross section in 10^-18 cm^2
3

Fano Factor
0

Interaction area in cm^2 (=pi * beam radius^2)
0.3

Oscillator strength
0.0018

Duration of the laser pulse in nanosec
15
15

Separation of the laser pulse in nanosec
0

Intensity of the lasers in mJ per pulse
0.00009
1

Scanning range of the laser frequency in Ghz
25
```

Part V

BIBLIOGRAPHY

BIBLIOGRAPHY

[1] V. N. Fedosseev, Y. Kudryavtsev, and V. I. Mishin, "Resonance laser ionization of atoms for nuclear physics," *Physica Scripta*, vol. 85, no. 5, p. 058104, May 2012. [Online]. Available: http://stacks.iop.org/1402-4896/85/i=5/a=058104?key=crossref.c4b819f0a5bcf527b8fa8270eb7e4ee1

[2] S. Gheysen, G. Neyens, and J. Odeurs, "Calculated hyperfine spectra for in-source laser spectroscopy and deduced magnetic moments and isomer shifts of Cu68 and Cu70 isomeric states," *Physical Review C*, vol. 69, no. 6, p. 064310, Jun. 2004. [Online]. Available: http://link.aps.org/doi/10.1103/PhysRevC.69.064310

[3] G. Neyens, "Nuclear magnetic and quadrupole moments for nuclear structure research on exotic nuclei," *Reports on Progress in Physics*, vol. 66, no. 4, pp. 633–689, Apr. 2003. [Online]. Available: http://stacks.iop.org/0034-4885/66/i=4/a=205?key=crossref.a8f63ecd4735d553dad9fc7c51e39bae

[4] T. J. Procter, H. Aghaei-Khozani, J. Billowes, M. L. Bissell, F. L. Blanc, B. Cheal, T. E. Cocolios, K. T. Flanagan, H. Hori, T. Kobayashi, D. Lunney, K. M. Lynch, B. a. Marsh, G. Neyens, J. Papuga, M. M. Rajabali, S. Rothe, G. Simpson, a. J. Smith, H. H. Stroke, W. Vanderheijden, and K. Wendt, "Development of the CRIS (Collinear Resonant Ionisation Spectroscopy) beam line," in *Journal of Physics: Conference Series*, vol. 381, Sep. 2012, p. 012070. [Online]. Available: http://stacks.iop.org/1742-6596/381/i=1/a=012070?key=crossref.114dfa01f32016dbee8c2da068fd4c8d

[5] T. J. Procter and K. T. Flanagan, "First on-line results from the CRIS (Collinear Resonant Ionisation Spectroscopy) beam line at ISOLDE," *Hyperfine Interactions*, vol. 216, no. 1-3, pp. 89–93, Feb. 2013. [Online]. Available: http://link.springer.com/10.1007/s10751-013-0833-6

[6] R. Neugart and G. Neyens, "Nuclear Moments, Lecture Notes on Physics," *Lecture Notes on Physics*, no. 700, pp. 135–189, 2006.

[7] B. Cheal and K. T. Flanagan, "Progress in laser spectroscopy at radioactive ion beam facilities," *Journal of Physics G: Nuclear and Particle Physics*, vol. 37, no. 11, p. 113101, Nov. 2010. [Online]. Available-

able: http://stacks.iop.org/0954-3899/37/i=11/a=113101?key=crossref.d0f0f994156e795b20c5d5ec720e9530

[8] J. H. Shirley, "Solution of the Schrodinger Equation with a Hamiltonian Periodic in Time," *Physical Review*, vol. 138, no. 4B, pp. 979–987, 1965.

[9] M. Horbatsch and E. a. Hessels, "Shifts from a distant neighboring resonance," *Physical Review A*, vol. 82, no. 5, p. 052519, Nov. 2010. [Online]. Available: http://link.aps.org/doi/10.1103/PhysRevA.82.052519

[10] ——, "Shifts from a distant neighboring resonance for a four-level atom," *Physical Review A*, vol. 84, no. 3, p. 032508, Sep. 2011. [Online]. Available: http://link.aps.org/doi/10.1103/PhysRevA.84.032508

[11] P. L. Knight and M. A. Lauder, "Laser Induced Continuum Structure," *Physics Reports*, vol. 190, no. 1, pp. 1–61, 1990.

[12] E. T. Jaynes and F. W. Cummings, "Comparison of quantum and semiclassical radiation theories with application to the beam maser," pp. 89–109, 1963. [Online]. Available: http://ieeexplore.ieee.org/xpls/abs_all.jsp?arnumber=1443594

[13] B. W. Shore and P. L. Knight, "The Jaynes-Cummings Model," *Journal of Modern Optics*, vol. 40, no. 7, pp. 1195–1238, 1993.

[14] D. M. Brink and G. R. Satchler, *Angular Momentum*, 3rd ed. New York: Oxford Science Publications, 1993.

[15] R. C. Hilborn, "Einstein coefficients, cross sections, f values, dipole moments and all that," *American Journal of Physics*, vol. 50, pp. 982–986, 1982.

[16] L. Anders and N. S. Erik, "TRANSITION PROBABILITIES FOR THE ALKALI ISOELECTRONIC SEQUENCES LI I , NA I , K I , RB I , Cs I , FR I," *Atomic Data and Nuclear Data Tables*, vol. 19, no. 6, pp. 533–633, 1977.

[17] N. Vitanov, "Power broadening revisited: theory and experiment," *Optics Communications*, vol. 199, no. 1-4, pp. 117–126, 2001. [Online]. Available: http://linkinghub.elsevier.com/retrieve/pii/S003040180101495X

[18] B. W. Shore, *The Theory of Coherent Atomic Excitation*. New York: John Wiley and Sons, 1990.

[19] I. I. Rabi, "Space Quantization in a Gyrating Magnetic Field," *Physical Review*, vol. 51, no. 1931, pp. 652–654, 1937.

[20] C. F. D. M. Faria and a. Fring, "Time evolution of non-Hermitian Hamiltonian systems," *Journal of Physics A: Mathematical and General*, vol. 39, no. 29, pp. 9269–9289, Jul. 2006. [Online]. Available: http://stacks.iop.org/0305-4470/39/i=29/a=018?key=crossref.7bd91c2a3154f68a82d664a33fc79556

[21] A. Imamoglu, "Interference of Radiatively Broadenend Resonances," *Physical Review A*, vol. 40, no. 5, pp. 2835–2838, 1989.

[22] S. E. Harris, "Lasers without Inversion: Interference of Lifetime-Broadened Resonances," *Physical Review Letters*, vol. 62, no. 9, pp. 1033–1036, 1990.

[23] C. Cohen-Tannoudji, *Atoms in electromagnetic fields*. World Scientific Publishing Company Incorporated, 1994.

[24] P. L. Knight, "AC Stark splitting of bound-continuum decays," *Journal of Physics B: Atomic, Molecular and Optical Physics*, vol. 12, no. 20, pp. 3297–3308, 1979.

[25] P. Alsing, D.-S. Gua, and H. J. Carmichael, "Dynamic Stark effect for the Jaynes-Cummings System," *Physical Review A*, vol. 45, no. 7, pp. 5135–5143, 1992.

[26] G. Belin, L. Holmgren, and S. Svanberg, "Hyperfine Interaction, Zeeman and Stark Effects for Excited States in Cesium," *Physica Scripta*, vol. 14, no. 1-2, pp. 39–47, Jul. 1976. [Online]. Available: http://stacks.iop.org/1402-4896/14/i=1-2/a=008?key=crossref.cc35ace47f14e31f83240cea5796df11

[27] J. P. Young, G. S. Hurst, M. G. Payne, and S. D. Kramer, "Resonance spectroscopy detection*," *Reviews of Modern Physics*, vol. 51, no. 4, pp. 767–819, 1979.

[28] M. L. Citron, H. R. Gray, C. W. Gabel, and C. R. J. Stroud, "Experimental Study of Power Broadening in a Two-Level Atom," *Physical Review A*, vol. 16, no. 4, pp. 1507–1512, 1977.

[29] U. Fano, "Effects of Configuration Interaction on Intensities and Phase Shifts," *Physical Review*, vol. 124, no. 6, pp. 1866–1878, 1961.

[30] P. E. Coleman and P. L. Knight, "Laser Induced Continuum Structure in Multiphoton Ionisation," *Optics Communications*, vol. 42, no. 3, pp. 171–178, 1982.

[31] L. P. Yatsenko, R. G. Unanyan, K. Bergmann, T. Halfmann, and B. W. Shore, "Population Transfer through the Continuum using Laser-Controlled Stark Shifts," *Optics Communications*, vol. 135, pp. 406–412, 1997.

[32] L. Yatsenko, T. Halfmann, B. Shore, and K. Bergmann, “Photoionization suppression by continuum coherence: Experiment and theory,” *Physical Review A*, vol. 59, no. 4, pp. 2926–2947, Apr. 1999. [Online]. Available: http://link.aps.org/doi/10.1103/PhysRevA.59.2926

[33] R. Eramo, S. Cavalieri, L. Fini, and M. Matera, “Observation of a laser-induced structure in the ionization continuum of sodium atoms using photoelectron energy spectroscopy Observation of a laser-induced structure in the ionization continuum of sodium atoms using photoelectron energy spectroscopy,” *Journal of Physics B: Atomic, Molecular and Optical Physics*, vol. 30, p. 3789, 1997.

[34] M. Koide, F. Koike, R. Wehlitz, M.-T. Huang, T. Nagata, J. C. Levin, S. Fritzsche, B. D. DePaola, S. Ohtani, and Y. Azuma, “New Window Resonances in the Potassium 3s Photoabsorption Spectrum,” *Journal of the Physics Society Japan*, vol. 71, no. 7, pp. 1676–1679, Jul. 2002. [Online]. Available: http://jpsj.ipap.jp/link?JPSJ/71/1676/

[35] M. Koide, F. Koike, T. Nagata, J. C. Levin, S. Fritzsche, R. Wehlitz, M.-T. Huang, B. D. DePaola, S. Ohtani, and Y. Azuma, “Common Window Resonance Features in K and Heavier Alkaline Atoms Rb and Cs,” *Journal of the Physics Society Japan*, vol. 71, no. 11, pp. 2681–2686, Nov. 2002. [Online]. Available: http://jpsj.ipap.jp/link?JPSJ/71/2681/

[36] S. Feneuille, S. Liberman, J. Pinard, and A. Taleb, “Observation of Fano Profiles in Photionization of Rubidium in the Presence of a dc Field,” *Physical Review Letters*, vol. 42, no. 21, pp. 1404–1406, 1979.

[37] T. Peters and T. Halfmann, “Stimulated Raman adiabatic passage via the ionization continuum in helium: Experiment and theory,” *Optics Communications*, vol. 271, no. 2, pp. 475–486, Mar. 2007. [Online]. Available: http://linkinghub.elsevier.com/retrieve/pii/S003040180601162X

[38] a. Rangelov, N. Vitanov, and E. Arimondo, “Stimulated Raman adiabatic passage into continuum,” *Physical Review A*, vol. 76, no. 4, p. 043414, Oct. 2007. [Online]. Available: http://link.aps.org/doi/10.1103/PhysRevA.76.043414

[39] E. Jones, T. Oliphant, and P. Peterson, “Title: SciPy: Open Source Scientific Tools for Python.” [Online]. Available: http://www.scipy.org/

[40] C. Moler and C. Van Loan, “Nineteen Dubious Ways to Compute the Exponential of a Matrix,” *Society for Industrial and Applied Mathematics*, vol. 20, no. 4, pp. 801–836, 1978.

[41] T. Ida, M. Ando, and H. Toraya, "Extended pseudo-Voigt function for approximating the Voigt profile research papers Extended pseudo-Voigt function for approximating the Voigt profile," *Journal of Applied Crystallography*, vol. 33, pp. 1311–1316, 2000.

[42] T. Cocolios, a. Andreyev, B. Bastin, N. Bree, J. Büscher, J. Elseviers, J. Gentens, M. Huyse, Y. Kudryavtsev, D. Pauwels, T. Sonoda, P. Van den Bergh, and P. Van Duppen, "Magnetic Dipole Moment of Cu57,59 Measured by In-Gas-Cell Laser Spectroscopy," *Physical Review Letters*, vol. 103, no. 10, p. 102501, Aug. 2009. [Online]. Available: http://link.aps.org/doi/10.1103/PhysRevLett.103.102501

[43] T. E. Cocolios, a. N. Andreyev, B. Bastin, N. Bree, J. Büscher, J. Elseviers, J. Gentens, M. Huyse, Y. Kudryavtsev, D. Pauwels, T. Sonoda, P. V. D. Bergh, and P. Van Duppen, "Magnetic dipole moments of ^{57,58,59}Cu," *Physical Review C*, vol. 81, no. 1, p. 014314, Jan. 2010. [Online]. Available: http://link.aps.org/doi/10.1103/PhysRevC.81.014314

[44] P. Vingerhoets, K. Flanagan, J. Billowes, M. Bissell, K. Blaum, B. Cheal, M. De Rydt, D. Forest, C. Geppert, M. Honma, M. Kowalska, J. Krämer, K. Kreim, A. Krieger, R. Neugart, G. Neyens, W. Nörtershäuser, J. Papuga, T. Procter, M. Rajabali, R. Sánchez, H. Stroke, and D. Yordanov, "Magnetic and quadrupole moments of neutron deficient 58-62Cu isotopes," *Physics Letters B*, vol. 703, no. 1, pp. 34–39, Sep. 2011. [Online]. Available: http://linkinghub.elsevier.com/retrieve/pii/S0370269311008549

[45] Y. Kudryavtsev, J. Andrzejewski, N. Bijnens, S. Franchoo, J. Gentens, M. Huyse, A. Piechaczek, J. Szerypo, P. V. Duppen, P. V. D. Bergh, L. Vermeeren, J. Wauters, and A. Wiihr, "Beams of short lived nuclei produced by selective laser ionization in a," *Nuclear Instruments and Methods in Physics Research B*, vol. 114, pp. 350–365, 1996.

[46] Kurucz R.L. and B. Bell, "Atomic Line Data, Kurucz CD-ROM No. 23." Cambridge, 1995.

[47] I. I. Boradjiev and N. V. Vitanov, "Power narrowing in coherent atomic excitation by smoothly shaped pulsed fields," *Optics Communications*, vol. 288, pp. 91–96, Feb. 2013. [Online]. Available: http://linkinghub.elsevier.com/retrieve/pii/S0030401812010486

[48] T. Halfmann, T. Rickes, N. V. Vitanov, and K. Bergmann, "Lineshapes in coherent two-photon excitation," *Optics*

Communications, vol. 220, no. 4-6, pp. 353–359, May 2003. [Online]. Available: http://linkinghub.elsevier.com/retrieve/pii/S0030401803013683

[49] B. M and F. V, "Beweis des Adiabatensatzes," *Zeitschrift für Physik*, vol. 51, no. 3-4, pp. 165–180, 1928.

[50] J. E. Avron and A. Elgart, "Adiabatic Theorem without a Gap Condition," 1998.

COLOPHON

This document was typeset using the typographical look-and-feel `classicthesis` developed by André Miede. The style was inspired by Robert Bringhurst's seminal book on typography "*The Elements of Typographic Style*". `classicthesis` is available for both LaTeX and LyX:

`http://code.google.com/p/classicthesis/`

Instituut voor Kern-en Stralingsfysica
Celestijnenlaan 200D bus 2418
3001 HEVERLEE, BELGIË
tel. + 32 16 32 72 63
fax + 32 16 32 79 85
www.kuleuven.be